MICHIGAN STATE UNIVERSITY

CYCLOTRON LABORATORY

LIGHT PARTICLE EMISSION IN ^{16}O-INDUCED REACTIONS AT 140, 215, AND 310 MeV

Phys Rev C 25 (1982) 2361

T. C. AWES, S. SAINI, G. POGGI, C. K. GELBKE

D. CHA, R. LEGRAIN, and G. D. WESTFALL

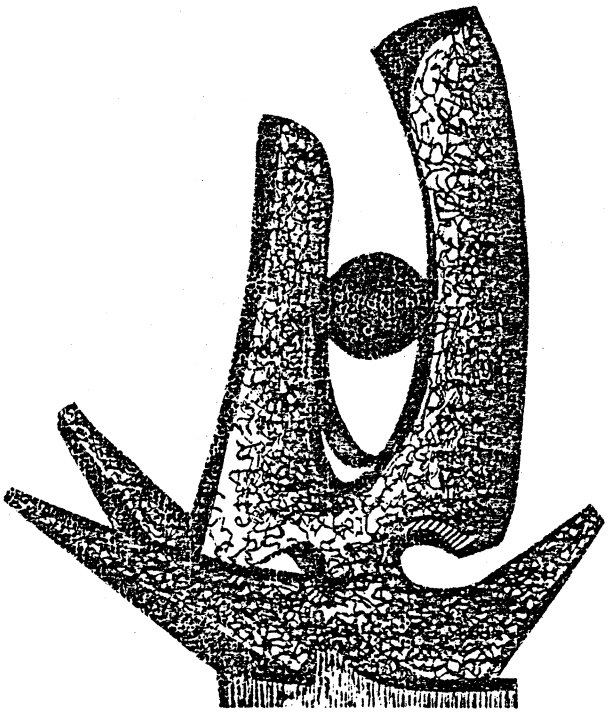

DECEMBER 1981

MSUCL-362

MSUCL-362
December 1981

Light Particle Emission in ^{16}O-induced Reactions at 140, 215, and 310 MeV

T.C. Awes,[+] S. Saini,[++] G. Poggi,[+++] C.K. Gelbke and D. Cha

Cyclotron Laboratory, Michigan State University
East Lansing, Michigan 48824 USA

and

R. Legrain[*] and G.D. Westfall[**]

Lawrence Berkeley Laboratory
Berkeley, California 94720 USA

+ Present address: Oak Ridge National Laboratory
Oak Ridge, Tennessee 37830

++ On Leave from Bhabha Atomic Research Center, India
Present address: Argonne National Laboratory
Argonne, Illinois 60439

+++ On Leave from University of Florence, Florence, Italy

* On Leave from C.E.N. Saclay, France

** Present address: Michigan State University
East Lansing, MI 48824

PACS Numbers: 25.70 Bc

ABSTRACT

Double differential cross sections have been measured for energetic p,d,t, and α-particles emitted in ^{16}O-induced reactions on targets of Al, Zr, and Au at incident energies of 140, 215, and 310 MeV. The energy and angular distributions are well described by isotropic emission from a moving thermal source. The extracted temperature and velocity parameters are found to vary systematically with the incident energy per nucleon above the Coulomb barrier. The observed trends cannot be explained by compound nucleus emission but instead suggest emission from a source which consists of comparable contributions from target and projectile. Alternatively, the proton energy spectra are compared with a precompound model and with a simple knock-out model. The d,t and α-particle cross sections are also described in terms of a generalized coalescence relation which takes into account Coulomb repulsion from the target nucleus.

NUCLEAR REACTIONS: ^{27}Al(^{16}O,x), E = 140, 215, and 310 MeV; ^{90}Zr(^{16}O,x), E = 215 and 310 MeV; ^{197}Au(^{16}O,x), E = 140, 215, and 310 MeV; x = p,d,t, and α. Measured $\sigma(E_x,\theta_x)$. Analysis in terms of moving source, precompound, knock-out, and coalescence models.

I. INTRODUCTION

The emission of energetic light particles in heavy-ion reactions provides a useful means of studying the development of the reaction mechanism from energies just above the Coulomb barrier up to relativistic energies. At low energies (E/A $\lesssim$ 5 MeV above the Coulomb barrier) detailed studies[1-4] of neutron emission in heavy systems have shown that the neutrons are evaporated statistically from the compound nucleus or from fully accelerated fragments. At somewhat higher energies there exists evidence for nonequilibrium neutron emission[5-12] as well as nonequilibrium charged particle emission.[6,13-31] Many of these studies have involved coincidence measurements between the light particles and projectile-like fragments.[16-21] The interpretation of these experiments is dependent upon assumptions of whether the light particles result from sequential decay and, if so, upon assumptions about the primary distribution of the projectile fragments.[32] As a result, systems similar to those which were associated with nonequilibrium effects, have also been shown to be consistent with equilibrium emission from excited projectile residues.[32-34] By identifying coincident fusion products with γ-ray techniques[25-28] or by measuring the momentum transfer to the target residue,[29-31] however, it has been possible to establish the emission of energetic light particles in processes that cannot be associated with compound nucleus emission or sequential decay of fully accelerated and equilibrated heavy reaction products. Reactions

in which a major portion of the projectile mass is transferred to the target make an important contribution to the light particle emission.

Until the present, few single particle inclusive measurements have been published[13-15] in the energy range E/A $\lesssim$ 20 MeV. It is only recently that studies of the projectile, target, and beam energy dependence of the non-equilibrium light particle emission have been reported.[35-37] This is in contrast to the situation at relativistic energies where several systematic inclusive light particle emission studies have been made.[38-40] These experiments have caused a great deal of theoretical interest. The models which have been proposed range from thermal emission by the participant matter as in the fireball[41] or firestreak[42] models to the single scattering knock-out model.[43,44] The inclusive data have been found to carry sufficient information to rule out either single scattering or thermal emission as the sole source of light particles.[40] Instead, the data suggest a model in which both direct and thermal components are considered either explicitly[45] or by including contributions from single and multiple collisions as in linear cascade models[46-48] or fully three dimensional cascade models.[49,50]

At low energies there exist analogs to the high energy models such as the "hot spot"[17,22,23,51-56] thermal models, the prompt emission[57,58] (PEPs) single scattering model, and the cascade[59] and precompound[60-62] models which consider the time development of the approach to equilibrium. Un-

fortunately, quantitative comparisons with the data have been made for only a few inclusive measurements[14,15] and these isolated cases have not been sufficient to decide between the various models.

In this paper we present a systematic study of the emission of energetic light particles (p,d,t,α) in ^{16}O-induced reactions on targets of Al, Zr and Au at incident energies of 140, 215 and 310 MeV. In the next section of this paper we describe the experimental details. The experimental energy and angular distributions and the total light particle cross sections are presented in Sec. III. In Sec. IV, the light particle spectra are discussed in terms of various models. This section includes a comparison with the moving thermal source model[15] and a discussion of the dependence of the moving source parameters on beam energy and target. We then compare the proton cross sections with a simple knock-out calculation and a precompound[61] calculation. And finally, we discuss the connection between the composite particle production and the proton cross sections in terms of a generalized coalescence relation.[31,63] A summary of our results and conclusions will be given in Sec. V. Details of the knock-out calculation are presented in the Appendix. Some of the present results have been published previously.[35]

II. EXPERIMENT

The experiment was performed at the 88-inch cyclotron of the Lawrence Berkeley Laboratory using ^{16}O beams of 140, 215, and 310 MeV incident energies with typical intensities of 20, 1, and 0.5 nA, respectively. Measurements were made using three different targets spanning a large mass range. An ^{27}Al target of 1.6 mg/cm^2 thickness was used at all three bombarding energies. A ^{90}Zr foil of 20.9 mg/cm^2 thickness and a 10.6 mg/cm^2 thick ^{197}Au foil were each irradiated at 215 and 310 MeV incident energies. In addition, a thin ^{197}Au target of 1.2 mg/cm^2 thickness was bombarded at 140 MeV incident energy. This target was found to have a hydrogen contaminant which gave rise to a distinct peak in the forward angle proton spectra. This contribution has been removed in the analysis.

Light particles (p,d,t, and α) were detected with two ΔE-E telescopes mounted on a movable table inside the scattering chamber. Each telescope subtended a solid angle of 22 msr and consisted of a 400 μm thick surface barrier detector and a 7.6 cm thick NaI(Tl) detector the entrance window of which consisted of a Havar foil of about 75 μm thickness. For hydrogen isotopes the energy calibration of the NaI detectors was established by measuring the elastic scattering of protons on a ^{197}Au target at the incident energies of 10, 20 and 45 MeV. The resulting energy calibration was found to be linear over this energy range and was extra-

polated toward high energies. An independent energy calibration was established for alpha particles by measuring the elastic scattering of alpha particles on ^{197}Au at 40, 80 and 120 MeV. The resulting energy calibration was found to be slightly non-linear with a decreasing response toward higher energies. The gain stability of the NaI(Tl) detectors was monitored by recording the γ-ray spectra of ^{60}Co during ion source changes. The energy calibration of the ΔE silicon detectors was obtained by injecting a known amount of charge into the input stage of the preamplifiers. This energy calibration was verified by calculating the energy loss corresponding to the measured ΔE signal of the elastically scattered proton and alpha beams. The overall accuracy of the energy calibration is estimated to be about 3%.

The ΔE and E energy signals of the two telescopes were recorded event by event on magnetic tape for off-line analysis. Mass and charge identification of the light particles was obtained from the measured energy losses in the ΔE and E detectors by using a standard particle identification (PI) function of the form[64]

$$PI \propto (E + \Delta E)^{\gamma} - E^{\gamma} \qquad (1)$$

where γ is a parameter which was taken to be 1.71 with the energy calibration of the hydrogen isotopes. This allowed a clean separation of the hydrogen isotopes and an identification of helium. If a particle was identified as helium, the α-particle energy calibration was applied and a new PI function was calculated which allowed the resolution of the individual

helium isotopes. However, due to the much greater abundance of alpha-particles, the spectra of ^{3}He were not analyzed due to non-negligible alpha-particle contributions.

Differential cross sections were determined using the measured target thickness and integrated beam current. The dead time of the system was monitored by injecting a pulse into the detector preamplifiers at a rate which was proportional to the beam current. The resulting dead time corrections were usually less than 4%. The absolute magnitude of the cross sections is estimated to be accurate to within 35%.

III. EXPERIMENTAL RESULTS

A. Spectral Shapes

Some of the general features of the light particle spectra observed in the present experiment may be seen in Figs. 1-3. In Fig. 1, the light particle spectra for reactions of 140 MeV ^{16}O on ^{197}Au are shown by solid points at three selected angles which span the full angular range of the present study. Also shown are the corresponding energy spectra for reactions on ^{27}Al. In order to facilitate a comparison of the spectral shapes, the ^{27}Al cross sections have been renormalized at 20 MeV for the isotopes of hydrogen and at 40 MeV for alpha particles. In Figs. 2 and 3 similar comparisons are made for the incident energies of 215 and 310 MeV, respectively. It is observed that these different

target nuclei give rise to light particle spectra with very similar characteristics. Reactions on both ^{27}Al and ^{197}Au targets show smooth structureless energy spectra which extend well beyond the incident energy per nucleon of the beam and show a distinct shouldering at the most forward angles. Both targets also display nearly exponential tails which are very similar at each angle for all light particle species and which become progressively steeper toward backward angles. The only persistent difference between the light particle energy spectra resulting from reactions on the two targets is that in the case of ^{27}Al the energy spectra have slightly flatter slopes. This observation may be explained by the fact that the relative velocity of target and projectile at the point of contact is slightly higher for reactions on Al than on Au due to the lower Coulomb barrier for the Al target. These observations indicate that the light particle spectra depend mainly on the available energy per nucleon above the Coulomb barrier and to a much lesser extent on the characteristics of the target.

B. Angular Distributions

The light particle angular distributions from the present study are shown in Figs. 4-6 for reactions of ^{16}O on ^{197}Au, ^{90}Zr, and ^{27}Al at the three incident energies. The distributions were obtained by summing over all energies with the lower threshold set at 12 MeV for the hydrogen isotopes and at

30 MeV for alpha particles. The cross sections increase with increasing incident energy. The angular distributions are forward peaked at all energies and for all light particles. The slope of the angular distributions increases monotonically with the mass of the outgoing light particle. The shape of the angular distributions appears to be nearly independent of the incident energy, but becomes progressively more isotropic with increasing mass of the target nucleus. An interpretation of some of these features as well as a description of the dashed curves in Figs. 4-6 will be given in Sec. IV.A.

C. Light Particle Cross Sections

Total inclusive cross sections integrated over energy and angle are listed in Table I. The integration over energy has been made with a 12 MeV threshold for hydrogen isotopes and a 30 MeV threshold for alpha-particles and thereby emphasizes the nonequilibrium contributions to the cross sections. Also shown in Table I are the total reaction cross sections as calculated using the heavy-ion optical model code HOP II[65] with the optical potentials[66-68] listed in Table II. The calculated reaction cross sections were found to be rather independent of the details of the optical potential parameters. For example, interchanging potentials between the targets resulted in only 10% changes in the calculated total reaction cross sections. From Table I it is seen that the cross sections for producing protons and alpha particles are comparable

for each target and incident energy. On the other hand, the cross section for the production of deuterons is typically inhibited over proton emission by a factor of 3 to 4 with triton emission inhibited by another factor of about 2. The cross sections for light particle emission are observed to constitute a significant fraction of the total reaction cross section and even exceed it at the highest energies indicating mean multiplicities comparable to one.

The dependence of the average proton multiplicity, σ_p/σ_R, on target mass and incident energy per nucleon above the barrier is shown in Fig. 7. Also included in the figure is the multiplicity of the summed hydrogen isotopes. The Coulomb barrier in the laboratory was calculated according to

$$V_c = \frac{(A_p+A_t)}{A_t} \frac{Z_p Z_t e^2}{r_o(A_p^{1/3}+A_t^{1/3})} \qquad (2)$$

where A_p, A_t and Z_p,Z_t are the mass and atomic numbers of the projectile and target and r_o = 1.44 fm. The proton multiplicity is observed to be essentially independent of target and to increase smoothly with increasing available energy per nucleon. Therefore, we may conclude that the light particle multiplicities, excluding low energy contributions, depend only slightly on the details of the target nucleus but mainly on the incident energy per nucleon above the Coulomb barrier.

IV. INTERPRETATION OF LIGHT PARTICLE EMISSION

A. Moving Source Model

1. Energy Spectra

Energy spectra for the $^{197}Au(^{16}O,p)$ reaction at three incident energies are shown in Fig. 8. Although the features of these spectra are qualitatively similar to those reported in ref. 15 for the same system at 310 MeV, our data differ in slope. The reason for this difference is not understood; however we were able to reproduce our results at 310 MeV in two independently calibrated experiments.

We have chosen to parameterize the light particle spectra in terms of emission from a Maxwellian source which is at rest in a frame that moves with a velocity intermediate between target and projectile.[15,31,63] Correcting for the Coulomb repulsion of the light particle from the target residue one obtains non-relativistically[31,63]

$$\frac{d^2\sigma}{dEd\Omega} = N_o (E-ZE_c)^{\frac{1}{2}} \exp\{-(E-ZE_c+E_1-2E_1^{\frac{1}{2}}(E-ZE_c)^{\frac{1}{2}}\cos\theta)/T\} . \qquad (3)$$

Here E_c is the kinetic energy gained by the light particle of charge Z due to the Coulomb repulsion from the target, $E_1=\frac{1}{2} mv^2$ is the kinetic energy of a particle at rest in the moving frame, T is the source temperature, θ is the detection angle and N_o is an overall normalization constant.

As seen by the solid curves of Figs. 8-10, the moving source parameterization provides a good description of the proton spectra for all targets and incident energies with temperatures which are typically greater than those of the compound nucleus and velocities intermediate between the projectile and compound nucleus velocity. It has been shown[25-31] that reactions in which nearly the entire projectile is absorbed by the target nucleus contribute significantly to the emission of energetic light particles. This would preclude the existence of an independent thermal source. The successful application of this parameterization should not, therefore, be taken as evidence for a hot gas of nucleons separated from the target nucleus. Instead, it simply indicates that the light particle velocities are randomized in a rest frame different from the compound nucleus rest frame.

In the present analysis, the temperature and velocity parameters have been determined by a least-squares minimization while the Coulomb threshold parameters E_c have been chosen at values of E_c = 0, 5, and 10 MeV for the Al, Zr, and Au targets, respectively. In the fitting procedure each data point was given an additional 10% error to reduce the statistical weight of the low energy regions of the spectra. The major effect of the E_c parameter is to modify the low-energy region of the fit.[31,63] An example of the shape of the χ^2-minima is shown in Fig. 11 for the $^{197}Au(^{16}O,p)$ reaction at 310 MeV. Here the reduced χ^2-values are shown for variations in the temperature, velocity, and Coulomb parameters. In

general, changes of about 5% in the temperature or about 10% in the velocity parameter increase the reduced χ^2-values by about 20%. In addition, the velocity parameter is found to be quite sensitive to the angular range over which the data are fit. For example, by considering only the region from 20^o - 80^o for the $^{27}Al(^{16}O,p)$ reaction at 140 MeV, values of v = 0.071c and T = 3.84 MeV were obtained as compared to the values of v = 0.049c and T = 3.96 MeV obtained by considering the full angular range. This observation explains the comparatively large source velocity extracted for reactions on the ^{197}Au target at 140 MeV where only a restricted angular range of data was measured.

Energy spectra and moving source calculations for deuteron, triton, and alpha-particle emission are presented in Figs. 12-14, Figs. 15-17, and Figs. 18-20, respectively. The moving source parameterization gives quite a reasonable description of the composite particle energy spectra although the reproduction of the angular dependence becomes somewhat worse with increasing mass of the outgoing composite particle. The most persistent discrepancy between the moving source model and experiment occurs at forward angles for the higher incident energies. Here the increasing contributions from direct processes such as projectile breakup are likely to become significant.[40,69]

Integrating Eq. (3) over energy with a low-energy threshold, E_T, the following expression for the moving source angular distribution is obtained

$$\frac{d\sigma}{d\Omega} = \frac{N_o}{2\pi} (\pi T)^{3/2} e^{-E_1 \sin^2\theta/T} \{(1+2x^2)+((1+2x^2)\mathrm{erf}(x-y)+\frac{2}{\pi^{1/2}}(x+y)e^{-(x-y)^2})\} \quad (4)$$

where $x = (E_1/T)^{1/2}\cos\theta$ and $y = ((E_T-E_c)/T)^{1/2}$. For $E_T = E_c$ we have $y = 0$ and observe that the first term in Eq. (4) is symmetric in x about 90^o while the second term is antisymmetric and accounts for the observed forward peaking of the angular distributions. The calculated moving source angular distributions are shown by the dashed curves in Figs. 4-6. These curves have been calculated at 310 MeV incident energy for all light particles with the indicated low-energy thresholds and using the proton velocity and temperature parameters (see Table III). The differences in the angular distibutions of the various light particles are essentially accounted for by the kinematic effect of the differing masses. This is reflected in the dependence of Eq. (4) on the ratio $E_1/T = \frac{1}{2}mv^2/T$ which reduces to a pure mass dependence due to the similarity of the velocity and temperature parameters for all particle types in a particular reaction (see Table III). Within this model, one expects the source velocity to be the same for all light particles while the thermal velocity should decrease for increasing particle mass. As a consequence, the angular distributions exhibit steeper slopes with increasing mass of the emitted particles.

A summary of the extracted moving source parameters is given in Table III. Also included are the light particle cross sections calculated according to

$$\sigma = 2 N_o (\pi T)^{3/2} \quad (5)$$

which is obtained by integrating Eq. (3) over energy from $E = E_c$ and over angles. These cross sections should be compared with those listed in Table I as an indication of the amount of cross section falling below the low-energy cut-offs introduced in Table I. From Table III it is observed that, for each reaction, the extracted velocity parameters are very similar for all light particle species whereas the temperature parameters are slightly lower for protons than for the composite particles. These features, as well as the dependence of the parameters on target and incident energy, will be discussed in detail in the following section.

2. Systematics of Moving Source Parameters

The dependence of the moving source parameters on target and incident energy is shown in Fig. 21. The temperature and velocity parameters exhibit an approximately linear dependence on $((E-V_c)/A)^{1/2}$, or equivalently, on the relative velocity of target and projectile at the point of contact. Here, V_c is the recoil-corrected Coulomb barrier calculated according to Eq. (2) and A is the mass number of the projectile. As indicated by the dashed curves of Fig. 21, such a dependence cannot be explained by compound nucleus emission. Instead it suggests more rapid processes such as knock-out or the formation of a hot subsystem of nucleons. In fact, the

observed linear dependence on the relative velocity can be understood if one assumes the formation of a hot Fermi gas consisting of equal nucleon contributions from target and projectile. In this case the temperature will be given by[31,63]

$$T_{nn} = \left(\frac{m_o \epsilon_F}{2}\right)^{\frac{1}{2}} v_{rel} \qquad (6)$$

where $v_{rel}=(2(E-V_c)/(m_o A))^{\frac{1}{2}}$ is the relative velocity at the point of contact, m_o is the nucleon mass and ϵ_F = 38 MeV is the Fermi energy corresponding to normal nuclear matter. Furthermore, due to equal target and projectile contributions, nucleon emission should be isotropic in the nucleon-nucleon rest frame. The velocity of this frame, after accounting for target recoil, is given by

$$v_{nn} = \frac{v_{rel}}{2} + \frac{A_p}{(A_t+A_p)}(v_B - v_{rel}) \approx \frac{v_{rel}}{2} \qquad (7)$$

where v_B is the beam velocity and A_p and A_t are the mass numbers of projectile and target. According to the solid curves of Fig. 21 the temperature and velocity parameters are 25% lower than the equal contributions limit given by Eqs. (6) and (7).

It is interesting to investigate whether the observed trends can be extrapolated toward relativistic energies where similar thermal models[38,41,42] have been used to describe the light particle spectra. With this in mind we have determined temperature and velocity parameters for the reaction

^{20}Ne + NaF → p at incident energies of E/A = 400 and 800 MeV.[40] This has been done in a manner consistent with our low energy treatment by using the relativistic generalization of Eq. (3) for the Lorentz-invariant cross section[35]

$$\frac{E}{p^2}\frac{d^2\sigma}{dpd\Omega} = N_o\gamma(E-\beta p\cos\theta)\exp(-\gamma(E-\beta p\cos\theta)/T) \qquad (8)$$

where β is the velocity of the source (c=1), $\gamma=(1-\beta^2)^{-\frac{1}{2}}$, and $E=(p^2+m_o^2)^{\frac{1}{2}}$. In order to minimize the contribution from fragmentation and knock-out[40] we have restricted our consideration to the data at large transverse momenta ($\theta \geq 45^o$). Despite the simplicity of the present parameterization, it provides an acceptable description of the experimental data, see Fig. 22.

The trend of the temperature parameter observed at low energies may be connected smoothly to the temperatures obtained for the Ne + NaF reaction at relativistic energies.[35] This is shown in Fig. 23 where, for orientation, the solid and dashed curves have been calculated for relativistic Fermi and Boltzmann gases consisting of equal nucleon contributions from target and projectile. In this case, the excitation energy per nucleon, ϵ^*, is related to the incident kinetic energy per nucleon above the Coulomb barrier, $(E-V_c)/A$, according to

$$\epsilon^* = \left(m_o^2 + \tfrac{1}{2}m_o(E-V_c)/A\right)^{\frac{1}{2}} - m_o \ , \qquad (9)$$

where m_o is the nucleon rest mass. Alternatively, the excitation energy per nucleon of the gas may be written as

$$\varepsilon^* = \langle\varepsilon(T)\rangle - \langle\varepsilon(T=0)\rangle \quad , \tag{10}$$

where $\langle\varepsilon(T)\rangle$ is the average kinetic energy per nucleon at temperature T with $\langle\varepsilon(T=0)\rangle=0$ for a Boltzmann gas and $\langle\varepsilon(T=0)\rangle=3/5\varepsilon_F$ for a Fermi gas. Combining Eqs. (9) and (10) one obtains the desired relation between temperature and incident kinetic energy.

The average kinetic energy is calculated using

$$\langle\varepsilon(T)\rangle = \frac{V}{N}\frac{g}{2\pi^2\hbar^3}\int_0^\infty E(p)f(p,T)p^2dp \quad . \tag{11}$$

Here g is the spin-isospin degeneracy factor, $E(p) = (p^2+m_o^2)^{\frac{1}{2}}-m_o$ is the kinetic energy of the nucleon and f(p,T) is the distribution function given by

$$f(p,T) = \frac{1}{\alpha+\exp\{(E(p) - \mu(T))/T\}} \quad , \tag{12}$$

with $\alpha=0$ for Boltzmann statistics and $\alpha=1$ for Fermi statistics. The chemical potential $\mu(T)$ is determined from

$$\frac{N}{V} = \frac{g}{2\pi^2\hbar^3}\int_0^\infty f(p,T)p^2dp \quad , \tag{13}$$

by assuming normal nuclear density, $N/V = 0.17\ fm^{-3}$. We note that, at low energies, the temperature will be given

by Eq. (6) for a Fermi gas and by $T = 2\varepsilon^*/3$ for a Boltzmann gas.

The general trend of the experimental temperature parameters is seen to follow approximately that depicted by the Fermi gas calculation. Recent inclusive measurements for ^{12}C on ^{60}Ni at several energies confirm our low-energy temperature dependence[37]. Other recent measurements follow the trend of the Fermi gas curve in the intermediate energy region with reactions of ^{20}Ne + Ni, Ag, and Ta at E/A = 43 MeV,[69] ^{12}C + C, Al, Cu, Ag, and Au at E/A = 58 and 86 MeV,[70] and ^4He + Al and Ta at E/A = 180 MeV.[71] Taken literally, the observed trend suggests the thermalization of a subset of nucleons. However, because features of inclusive measurements may be reproduced by models having rather different assumptions[15,39,40] it should be investigated whether the observed trend can be reproduced by alternative approaches such as single scattering or precompound models. We will consider this question in the following two sections.

As a final comment, we draw attention to the insert of Fig. 23 which demonstrates that the temperatures extracted for deuterons and tritons are systematically larger than those for protons. This may be because the proton spectra contain larger contributions from more equilibrated processes such as compound nucleus evaporation. Further investigations with different target projectile combinations and at higher energies are necessary to elucidate the origin of this systematic temperature difference.

B. Knock-out model

The results of the previous section suggest that many of the features of the light particle spectra may be interpreted as evidence for thermal emission from a hot subsystem of nucleons consisting of equal contributions from target and projectile. However, before adopting such an interpretation we must investigate whether the observed characteristics can be explained by alternative methods. Our motivation derives from observations at relativistic energies where features of the proton spectra can be explained by fully thermal models[41,42] at one extreme, or alternatively, by single nucleon-nucleon scattering[43,44] at the other extreme. In this section a schematic single scattering knock-out model is considered to determine whether the observed proton energy and angular distributions might result from such a process.

At the incident energies of the present study, we envision a peripheral reaction in which a single nucleon of the projectile scatters in a quasi-free manner with a nucleon in the surface of the target. Following this interaction, one of the nucleons escapes and, as suggested by the rather low nucleon multiplicies observed (see Table I), the other nucleon is absorbed by the target or projectile. Describing the incoming and outgoing particles by plane waves, and using a zero-range nucleon-nucleon interaction, the differential cross section for observing the emitted nucleon with energy E is (see Appendix)

$$\frac{d^2\sigma}{dE d\Omega} \simeq \frac{k}{K_o}\int d^3K \left(\frac{1}{A}\left|F_A(\tilde{A}(\vec{K}_o+\vec{K}+\vec{k}))\right|^2 P_B(-\tilde{B}\vec{K}_o-\vec{K})\right.$$
$$\left. + \frac{1}{B}\left|F_B(\tilde{B}(-\vec{K}_o+\vec{K}+\vec{k}))\right|^2 P_A(\tilde{A}\vec{K}_o-\vec{K})\right)\delta(E_f-E_i) \qquad (14)$$

In this expression $\vec{K}_o$ is the incoming momentum of the projectile in the center of mass and $\vec{k}$ is the momentum of the knocked out nucleon. The quantities $\tilde{A}$ and $\tilde{B}$ are given by $\tilde{A} = (A-1)/A$ and $\tilde{B} = (B-1)/B$ where A and B are the mass numbers of the projectile and target, respectively. The first term in Eq. (14) represents knock-out from the target (see Fig. 35) with $P_B(\vec{q})$ being the momentum distribution of a nucleon in the target

$$P_B(\vec{q}) = \sum_\beta |\phi_\beta(\vec{q})|^2 \qquad (15)$$

and $F_A(\vec{q})$ is the form factor of the density distribution, $\rho_A(\vec{r})$, of the projectile

$$F_A(\vec{q}) = \int d^3r\, e^{-i(\vec{q}\cdot\vec{r})}\rho_A(\vec{r}) \; . \qquad (16)$$

Similarly, the second term of Eq. (14) represents knock-out from the projectile.

To evaluate $P(\vec{q})$ and $F(\vec{q})$ we use the harmonic oscillator s- and p-shell wavefunctions for ^{16}O to obtain

$$P_{16}(\vec{q}) = 4\left(\frac{6}{\pi}\right)^3(1+2b^2q^2)e^{-b^2q^2} \qquad (17)$$

and

$$F_{16}(\vec{q})=4(4-\tfrac{1}{2}b^2q^2)e^{-b^2q^2/4} \qquad (18)$$

with size parameter b=1.84 fm. Because the interactions are assumed to occur in the nuclear surface, the functions $P(\vec{q})$ and $F(\vec{q})$ for the target nuclei should be similar to those for ^{16}O. Therefore we have used the above functions for the target nuclei as well as for the ^{16}O projectile.

The knock-out calculation for the $^{197}Au(^{16}O,p)$ reaction (solid curves in Fig. 24) is found to reproduce the observed angular distribution in the low-energy region but falls off slightly faster than experiment in the high-energy region. The curves have been calculated using Eq. (A23) of the Appendix with P(q) and F(q) as described above. In addition, the calculated curves have been shifted by 8 MeV to approximate the Coulomb repulsion of the emitted proton from the target residue.

Although the similarity between knock-out calculation and experiment for the ^{197}Au target is encouraging, the knock-out model gives much steeper energy spectra than found experimentally for the $^{27}Al(^{16}O,p)$ reactions, see Fig. 25. Furthermore, when seemingly more realistic calculations were made by including all of the filled harmonic oscillator orbitals in $P(\vec{q})$ and $F(\vec{q})$ for the target nuclei, the calculated energy spectra were observed to fall-off much faster than experiment and showed an enhanced oscillatory structure (due primarily to $F(\vec{q})$) which is not observed in the experimental

data. Qualitatively similar results were obtained by using Woods-Saxon wavefunctions instead of the harmonic oscillator wavefunctions described above. Much steeper energy spectra were also obtained when both nucleons were assumed to escape. We conclude that the above schematic knock-out model cannot rule out that the single-scattering contribution to the proton spectra may be significant; however, it will be necessary to perform a more detailed analysis including distorted waves in the final state to determine the overall magnitude and details of the knock-out process.

C. Precompound Calculation

In the previous two sections we have considered two extreme explanations for the light particle emission. At one extreme a completely thermal model was applied and at the other a single-scattering model. In this section we consider a compromise viewpoint and allow both direct and thermal contributions. At relativistic energies models which include both contributions either explicitly[45] or by following the development of the collision process, as in cascade calculations[46-50], have been the most successful in reproducing the experimental light particle spectra.[40] At low energies, the preequilibrium[60] and cascade[59] calculations which follow the time development of the system toward equilibrum have been quite successful in reproducing the light particle spectra resulting from light-ion induced

reactions. Until now, however, there have not been sufficient inclusive light particle measurements to adequately test the recent generalization[61] of the preequilibrium model to heavy-ion induced reactions.

In the generalization of the precompound model to heavy-ion collisions[61] the modified master equation approach is applied with an additional term included to represent the time dependent addition of projectile nucleons to the equilibrating system as the fusion process develops. The number of projectile nucleons which enter the reaction region at each time interval is calculated from the geometrical volume of the projectile which passes through the tangential plane between target and projectile at the initial point of contact. Only S-wave collisions are considered, and the fusion rate is determined by the relative velocity at the point of contact. This model does not calculate angular distributions nor composite particle emission although it might be generalized to do so with further assumptions.[15,61,72]

The angle-integrated energy distributions as observed in the center-of-mass system for the $^{197}Au(^{16}O,p)$ reaction at 140, 215 and 310 MeV incident energies are compared in Fig. 26 with results of the heavy-ion precompound model. The precompound calculations have been normalized using the total reaction cross sections of Table I instead of the fusion cross sections and therefore are an overestimate of the expected proton cross sections. The calculations were performed using 60 steps over a relaxation interval

of 1.3×10^{-21} sec (as in ref. 61) and assuming available excitation energies of E*=97, 162 and 254 MeV at the three incident energies, respectively. In one case, the parameter n_o, which determines the distribution function has been arbitrarily chosen at n_c=20 and was assumed to be independent of energy. (We will call n_c the exciton number although it may also include collective degrees of freedom.) This calculation (see solid curves of Fig. 26 labeled n_o = 20) is seen to yield energy slopes which are too steep at 140 MeV and too flat at 215 and 310 MeV. In order to reproduce the observed spectral shapes, exciton number of about n_o=18, 25 and 30 must be assumed[73,74] at the energies of 140, 215 and 310 MeV (solid curves Fig. 26 labeled n_o = 18, 25, 30). Under the present assumptions of the model it is not possible to describe the proton spectra with an exciton number parameter which is independent of the incident energy.

In order to investigate those assumptions of the model which might be improved we have made two additional calculations which illustrate the effects governing the fusion process. Because evidence from deeply inelastic scattering suggests that the intermediate complex may be rather long-lived we have performed a calculation in which the fusion process is assumed to occur at one fifth of the rate expected from the relative velocities. This calculation yielded results which were virtually identical to the above results implying that the model is rather insensitive to the time scale of the fusion process. This suggests that the interactions

of an excited nucleon with cold nucleons are much more important than the interactions with other excited nucleons. The assumption of only S-wave collisions has been investigated by decreasing the available excitation energy by the rotational energy for fusion occurring at the angular momentum limit. Following the classical model of Bass[75] we have used rotational energies of E_{rot}=17, 34, and 34 MeV at the energies of 140, 215, and 310 MeV, respectively. These calculations, using an initial exciton number of n_o=16, are shown by the dotted curves in Fig. 26. Removing the rotational energy from the available excitation energy has the same effect as sharing the excitation energy among more excitons. However, it is still necessary to vary the number of excitons with incident energy in order to fit the data. Further work will be necessary in order to understand the energy dependence of n_o.

Also shown by the dashed curves in Fig. 26 are the energy distributions expected from the moving source model. These distributions were calculated according to

$$\frac{d\sigma}{dE} = \frac{2\pi N_o T}{\sqrt{E_1}} \exp(-(E-E_c+E_1)/T)\sinh(2(E_1)^{\frac{1}{2}}(E-E_c)^{\frac{1}{2}}/T) \qquad (19)$$

which is obtained by integrating Eq. (3) over solid angle. The calculations were performed using the parameters listed in Table III which fit the double differential cross sections (Fig. 8). With the exception of the 310 MeV data the agreement

with experiment is excellent. Here an additional component is observed in the experimental spectra at proton energies of about 50 MeV. This is the same component which was observed at forward angles in the double differential cross sections (Fig. 8) and is most likely due to a direct contribution.

D. Composite Particle Production

1. Proton to Deuteron Ratios

It has been suggested that the proton to deuteron ratio might offer a means of determining the amount of entropy produced in the region of overlap in heavy-ion reactions.[76] An excess production of entropy over that expected might provide an indication for an abnormal process such as a pion condensate or a phase transition to quark matter.[76,77] With increasing incident energy one expects the system to access more degrees of freedom and hence produce more entropy. Therefore, since composite particles have fewer degrees of freedom than the sum of their constituent nucleons, one would expect an increase in the ratio of nucleon emission to composite particle production as the bombarding energy is increased. Experimentally however, the proton to deuteron ratio has been found to vary little from relativistic energies[40] down to 20 MeV/nucleon.[31]

The proton to deuteron ratios of the present study are shown by the solid points in Fig. 27 as a function of

the incident energy per nucleon above the Coulomb barrier. The ratios were calculated using the cross sections of Table I with a low-energy cut-off of 12 MeV. With this rather high cut-off the p to d ratio is found, with the exception of ^{90}Zr, to be rather independent of the target. As the solid curve indicates, the ratio decreases smoothly from a value of 5 at the lowest energies to about 2.5 at the highest energies. This value is very similar to the values obtained at 400 MeV/nucleon incident energies which vary between 2 and 3 depending on the target-projectile system.[40] If the proton to deuteron ratio is in fact a measure of the entropy produced in the reaction then these ratios are much larger than expected, and the observed increase toward lower energies is contrary to expectations.[76,77] It has been suggested[78] that the proton to deuteron ratio may be limited to a value of about 3 at low energies due to the Pauli exclusion principle. An alternative explanation for the large proton to deuteron ratios is obtained in a hydrodynamic calculation[79] which includes the decay from excited states of composite particles. These decays effectively increase the proton to deuteron ratio to give good agreement with the experimentally observed ratios over the full range of incident energies. It is very likely that final state interactions may have a large effect on the observed ratios. In fact, it has been proposed that the deuterons result from pickup in the nuclear surface[80] and, therefore, have little relation to the concepts of chemical equilibrium or entropy production.

The open circles in Fig. 27 show the proton to deuteron ratios with the low-energy cut-offs lowered to near the detector thresholds at 8 and 10 MeV for protons and deuterons, respectively. The corresponding p/d-ratios, therefore, include larger contributions from possible compound nucleus evaporation. Including these contributions removes the degeneracy between the various targets. The reactions on the ^{90}Zr target contain the largest low-energy proton component, and the ^{197}Au target gives the smallest low-energy contribution due to its large Coulomb barrier. The proton to deuteron ratios are observed to increase toward lower incident energies which we may interpret as due to the increasing importance of compound nucleus reactions for which proton evaporation will be favored over deuteron emission.[81]

2. Coalescence Model

For heavy-ion collisions at relativistic energies it has been shown[38,40,82] that the energy spectra of composite light particles are related to the energy spectra of protons via a power law. In the coalescence model this power law is explained by the assumption that complex particles are formed by the coalescence of free nucleons which happen to occupy the same region of momentum space.[83] The model is a pure phase space approach and makes no assumption about the dynamics of the reaction. It involves a single free parameter, the coalescence radius, P_o, which is the radius

of the sphere in momentum space within which the coalescence occurs. There have been several attempts[84-86] to arrive at a dynamical understanding of the coalescence relation but at present the question of its dynamical basis must be considered open. Recently, the validity of the coalescence relation has been demonstrated at incident beam energies as low as 20 MeV/ nucleon.[31,63,87] It is interesting to further investigate the validity of the model at even lower energies and for various target-projectile combinations. At low energies it was demonstrated that the Coulomb field of the target residue should not be neglected.[31,63] The coalescence relation can be generalized to account for the Coulomb repulsion of the charged particles from the target residue to obtain[31]

$$\frac{d^2N(Z,N,E_A)}{dE_A d\Omega} = \left(\frac{N_t+N_p}{Z_t+Z_p}\right)^N \frac{A^{-1}}{N!Z!} \left\{\frac{4\pi P_o^3/3}{(2m_o^3(E-E_c))^{\frac{1}{2}}}\right\}^{A-1} \left(\frac{d^2N(1,0,E)}{dEd\Omega}\right)^A . \quad (20)$$

Here N_t,N_p and Z_t,Z_p are the neutron and proton numbers of target and projectile respectively, m_o is the nucleon rest mass, $d^2N(Z,N,E_A)/dE_A d\Omega$ is the differential multiplicity of nuclei composed of Z protons and N=A-Z neutrons, and E_A=AE-NE$_c$ where E_c is the Coulomb repulsion per unit charge. The differential multiplicity for a given event is not a measured quantity. In practice, it is approximated by the average differential multiplicity[31]

$$\frac{d^2N(Z,N)}{dE_A d\Omega} = \frac{1}{\sigma_R} \frac{d^2\sigma(Z,N)}{dE_A d\Omega} \quad (21)$$

where σ_R is the total reaction cross section. In the present analysis we use Eq. (21) with the total reaction cross sections listed in Table I.

The physical picture underlying Eq. (20) is that the coalescing neutrons and protons are emitted with the same energy distributions in the vicinity of the target residue. The light particles of charge Z then receive a Coulomb boost of energy ZE_c as they leave the Coulomb field of the target residue. More explicitly, it is assumed that the energy distributions of the coalescing protons and neutrons are related as

$$\frac{d^2N(0,1,E)}{dEd\Omega} = \frac{N_t+N_p}{Z_t+Z_p} \cdot \frac{d^2N(1,0,E+E_c)}{dEd\Omega} . \quad (22)$$

Although Eq. (20) has been quite successful in reproducing the composite particle spectra[31,63] it has recently been shown from a direct comparison of proton and neutron spectra[12] that the assumption of Eq. (22) is not completely valid. In order to resolve this apparent contradiction it is important to obtain light particle spectra, including neutron spectra, for a variety of systems and incident energies. In this section we demonstrate that Eq. (20) provides an adequate description of the composite particle spectra for reactions on the ^{197}Au and ^{27}Al targets at all three incident energies of the present study.

In Fig. 28 the energy spectra of light particles (solid points) are shown for reactions on ^{197}Au at 140 MeV. The spectra of the composite particles are compared with the predictions of the coalescence model (open squares) obtained from the experimental proton spectra shown in the upper left quadrant of the figure. The coalescence relation can reproduce the high energy tails of the composite particle spectra very well but becomes somewhat worse in the low energy region, especially for tritons. At incident energies of 215 and 310 MeV (see Figs. 29 and 30, respectively) the coalescence relation describes the composite particle spectra from reactions on ^{197}Au quite well, although the general agreement becomes slightly worse with increasing incident energy.

The composite particle spectra are compared to the coalescence relation for reactions on ^{27}Al at 140, 215 and 310 MeV in Figs. 31-33, respectively. The agreement between experiment and calculation is qualitatively similar to that observed for reactions on ^{197}Au. Allowing for the 10% uncertainty in the coalescence radii due to the 35% uncertainty in the absolute cross sections (see Eq. (20)) we cannot present conclusive evidence for an incident energy dependence of the coalescence parameter in the present study. The order of magnitude of the coalescence radii and the quality of the fits are similar to those obtained at relativistic energies.[82] However, in contrast to the general trends observed at relativistic energies[40,82] we extract smaller

coalescence radii P_o for reactions on the Al target than for the Au target. Within the thermodynamic interpretation[84] and density matrix formulation[86] of the coalescence model, the coalescence radius P_o is expected to be inversely proportional to the spatial radius of the interaction region. As a consequence, the interaction radius should increase, i.e. P_o should decrease, with increasing target mass. This target dependence is observed at high energies. The smaller values of P_o observed for the lighter target in the present experiment might indicate a change in the mechanism of light particle production at low energies. In fact, it has been suggested[80] that the composite particles are produced by the pickup of nucleons from the nuclear surface. Further experimental and theoretical studies of the energy, projectile and target dependence of composite light particle emission will be necessary to clarify the underlying reaction mechanism.

In performing the coalescence calculations a Coulomb parameter of E_c=7 MeV was found to give the best agreement with experiment for reactions on ^{197}Au. This value is significantly smaller than expected for emission of the charged particle from the surface of the composite nucleus. The low value of E_c may be due to deformations of the target residue or emission from the surface of the ^{16}O. However, the Coulomb parameter might not strictly reflect the difference in the proton and neutron distributions, as we noted above. Instead it might simply be a parameter which is useful in relating the proton spectra to the deuteron spectra. It

is reassuring though, that good agreement with the ^{27}Al data is obtained with a Coulomb parameter of E_c=0 MeV. It should be remarked that the larger coalescence radii for reactions on ^{197}Au might be a result of the different Coulomb parameters required for reactions on ^{197}Au and ^{27}Al.

The energy spectra of deuterons and tritons for reactions of ^{16}O on ^{90}Zr at 215 and 310 MeV incident energies are shown in Fig. 34. The coalescence results with E_c=0 MeV are shown by the solid curves. The coalescence model is seen to give a poor reproduction of the experimental spectra, especially at low energies where the calculated spectra appear to have the wrong slope. This discrepancy at low energies is due to the relatively large low-energy component in the proton spectra which has no counterpart in the composite particle spectra, (see also the discussion of Fig. 27). In fact, if we ignore the low-energy region of the proton spectra below 20 MeV then we should compare coalescence calculation and experiment in the region above 40 MeV for deuterons and above 60 MeV for tritons. The agreement between coalescence calculation and experiment is much better in this region.

V. SUMMARY AND CONCLUSION

We have studied inclusive light particle emission in ^{16}O-induced reactions on targets of ^{197}Au, ^{90}Zr, and ^{27}Al at incident energies of 140, 215, and 310 MeV. The light particle spectra can be parameterized in terms of a single thermal source which moves with slightly less than half

of the beam velocity. The extracted velocity and temperature parameters exhibit a systematic variation with the incident energy per nucleon above the Coulomb barrier. The trend of the temperature parameter can be extrapolated to temperatures observed in relativistic heavy-ion collisions. This systematic behavior follows the trends expected for the formation of a Fermi gas consisting of about equal contributions of nucleons from target and projectile. At present it is not clear why deuterons and tritons exhibit larger temperature parameters than protons.

Since the temperature and velocity parameters of the moving source model suggested an interpretation in which each interacting nucleon of the projectile was paired with a nucleon of the target we have investigated a single-scattering knock-out model. These calculations, which involved a plane wave approximation, demonstrate that a direct mechanism might be able to explain some features of the energy distributions, especially at forward angles. It will be necessary to perform more detailed calculations with distorted waves in order to determine the magnitude and details of the knock-out contribution.

The proton energy spectra for reactions on ^{197}Au have also been compared with the results of precompound calculations. It was shown that the spectra could not be described with a single energy-independent exciton number. Although the energy dependence of the exciton number was not due to assumptions on the rate of the fusion process, it might be explained by accounting for the local velocity and excitation of the system as the fusion progresses.

The light particle multiplicities were observed to increase smoothly with incident energy approaching unity at the highest energies. On the other hand, the proton to deuteron ratio was observed to decrease with energy to a value very similar to that observed at relativistic energies. This observation might indicate that the proton to deuteron ratio is largely determined by final state effects rather than by chemical equilibrium. Future theoretical and experimental investigations will be necessary to clarify whether this ratio can be used to extract information about the entropy produced in heavy-ion collisions.

We have shown that the coalescence model may be extended to energies of less than 10 MeV/nucleon with little change in the coalescence parameter. However, a large low-energy contribution in the proton spectra prohibited a satisfactory application of the coalescence relation to the composite particle spectra for reactions on the ^{90}Zr target. It was found that the ^{197}Au target resulted in the largest coalescence radii. This is in contrast to the situation at relativistic energies where the coalescence radii generally decrease with increasing target mass. At present, the details of the production of composite light particles are not fully understood. The variation of the coalescence radius with energy and projectile target combination is an interesting topic for future investigations. Of equal importance is an investigation of the apparent disagreement of the neutron spectra with the assumption underlying the present form of the coalescence relation.

ACKNOWLEDGEMENTS

We would like to thank Dr. G.F. Bertsch for his continuing interest and for assistance with the knock-out calculations. We wish to extend our appreciation to Dr. M. Blann for making his precompound code available to us and for many helpful suggestions concerning the precompound calculations. We would also like to express our gratitude to Dr. S. Nagamiya and coworkers for providing us with their experimental data prior to publication and to Professor D.K. Scott for many discussions. One of us (C.K.G.) acknowledges an Alfred P. Sloan fellowship. This material is based upon work supported by the National Science Foundation under Grant No. PHY 80-17605 and in part by the Office of Basic Energy Sciences, Division of Nuclear Sciences, U.S. Department of Energy.

APPENDIX: Knock-out Mechanism in Low-Energy Heavy-ion Collisions

We wish to investigate the role of a knock-out mechanism in heavy-ion reactions at incident energies of about 20 MeV/nucleon. At these energies we envision a peripheral process in which a single nucleon from the projectile scatters in a quasi-free manner with a nucleon of the target. This is followed by the escape of one nucleon and the subsequent absorption of the other nucleon by either the target (Fig. 35a) or the projectile (Fig. 35b). A simple plane wave approximation is applied in order to determine whether such a single-scattering process can account for the observed shapes of the energy and angular distributions.

We consider first the process of nucleon knock-out from the target (Fig. 35b). The incoming projectile of mass number A and target of mass number B are described by plane waves of momenta $\vec{K}_o$ and $-\vec{K}_o$, respectively. The final state is similarly approximated by plane waves with wave vectors $\vec{k}$, $\vec{K}_A$, and $\vec{K}_B$ for the emitted nucleon, the outgoing projectile, and the target residue of mass number B-1, respectively. The initial and final wavefunctions $|i\rangle$ and $|f\rangle$ are written as

$$|i\rangle = \frac{1}{V} e^{i\vec{K}_o\cdot(\vec{R}_A - \vec{R}_B)} \phi_\alpha(\vec{r}_a - \vec{R}_a)\, \phi_\beta(\vec{r}_b - \vec{R}_b) \quad (A1)$$

and

$$|f\rangle = \frac{1}{V^{3/2}} e^{i\vec{K}_A\cdot\vec{R}_A} e^{i\vec{K}_B\cdot\vec{R}_b} e^{i\vec{k}\cdot\vec{r}_b} \phi_{\alpha'}(\vec{r}_a - \vec{R}_a) \quad (A2)$$

where V is the normalization volume of the plane waves and ϕ_α and ϕ_β are the wavefunctions for the relative motion of the interacting nucleon within the projectile and target nucleus, respectively. Here $\vec{R}_A$ and $\vec{R}_B$ are the coordinates of projectile and target, $\vec{r}_a$ and $\vec{r}_b$ are the coordinates of the interacting projectile and target nucleons, and $\vec{R}_a$ and $\vec{R}_b$ are the coordinates of the projectile and target residues consisting of A-1 and B-1 nucleons, respectively. These coordinates are related by

$$A\vec{R}_A = (A-1)\vec{R}_a + \vec{r}_a \quad (A3a)$$

$$B\vec{R}_B = (B-1)\vec{R}_b + \vec{r}_b \quad (A3b)$$

Using $\vec{R}_a$, $\vec{R}_b$, $\vec{r}_a$, and $\vec{r}_b$ as independent variables and expressing the bound state wavefunctions in terms of their Fourier components the initial and final state wavefunctions become

$$|i\rangle = \frac{1}{(2\pi)^3 V} e^{i\vec{K}_o\cdot\left[\frac{(A-1)}{A}\vec{R}_a + \frac{\vec{r}_a}{A}\right]} e^{-\vec{K}_o\cdot\left[\frac{(B-1)}{B}\vec{R}_b + \frac{\vec{r}_b}{B}\right]}$$

$$\times \int d^3k_a d^3k_b \phi_\alpha(\vec{k}_a)\phi_\beta(\vec{k}_b)\, e^{i\vec{k}_a\cdot(\vec{r}_a - \vec{R}_a)}\, e^{i\vec{k}_b\cdot(\vec{r}_b - \vec{R}_b)} \quad (A4)$$

and

$$|f\rangle = \frac{1}{(2\pi)^{3/2}V^{3/2}}\, e^{i\vec{K}_A\cdot\left[\frac{(A-1)}{A}\vec{R}_a + \frac{\vec{r}_a}{A}\right]} e^{i\vec{K}_B\cdot\vec{R}_b}\, e^{i\vec{k}\cdot\vec{r}_b}$$

$$\times \int d^3q\; e^{i\vec{q}\cdot(\vec{r}_a - \vec{R}_a)}\phi_{\alpha'}(\vec{q}) \quad . \qquad (A\,5)$$

The interaction matrix element $\langle f|v|i\rangle$ is evaluated by assuming a zero range interaction, $v(\vec{r}_a,\vec{r}_b) = v_o\delta(\vec{r}_a - \vec{r}_b)$, between the interacting nucleons. Using Eqs. (A4) and (A5) one obtains

$$\langle f|v|i\rangle = \frac{1}{(2\pi)^{9/2}}\frac{v_o}{V^{5/2}}\int d^3q\, d^3k_a\, d^3k_b\, \phi^*_{\alpha'}(\vec{q})\,\phi_\alpha(\vec{k}_a)\,\phi_\beta(\vec{k}_b)$$

$$\times \int d^3R_a\; e^{i\left[\vec{K}_o\frac{(A-1)}{A} - \vec{k}_a - \vec{K}_A\frac{(A-1)}{A} + \vec{q}\right]\cdot\vec{R}_a}$$

$$\times \int d^3R_b\; e^{i\left[-\vec{K}_o\frac{(B-1)}{B} - \vec{k}_b - \vec{K}_B\right]\cdot\vec{R}_b}$$

$$\times \int d^3r_a\; e^{i\left[\vec{k}_a + \vec{k}_b + \frac{\vec{K}_o}{A} - \frac{\vec{K}_o}{B} - \frac{\vec{K}_A}{A} - \vec{k} - \vec{q}\right]\cdot\vec{r}_a} \quad . \qquad (A6)$$

By rewriting the spatial integrals in terms of δ-functions and integrating over d^3k_a and d^3k_b the following expression is obtained

$$\langle f|v|i\rangle = \frac{(2\pi)^{9/2}v_o}{V^{5/2}}\int d^3q\,\phi^*_{\alpha'}(\vec{q})\,\phi_\alpha(\tilde{A}(\vec{K}_o - \vec{K}_A) + \vec{q})\,\phi_\beta(-\tilde{B}\vec{K}_o - \vec{K}_B)$$

$$\times\ \delta(\vec{K}_A + \vec{K}_B + \vec{k}) \quad . \qquad (A7)$$

Here we have introduced the quantities $\tilde{A} = (A-1)/A$ and $\tilde{B} = (B-1)/B$. The δ-function in Eq. (A7) insures momentum

conservation. We make the replacement

$$\int d^3q\,\phi^*_{\alpha'}(\vec{q})\,\phi_\alpha(\vec{q}+\vec{K}) = \int d^3r\, e^{-i\vec{K}\cdot\vec{r}}\phi^*_{\alpha'}(\vec{r})\,\phi_\alpha(\vec{r}) = \rho_{\alpha'\alpha}(\vec{K}). \qquad (A8)$$

With this substitution Eq. (A7) becomes

$$\langle f|v|i\rangle = \frac{(2\pi)^{9/2}v_o}{V^{5/2}}\,\rho_{\alpha'\alpha}(\tilde{A}(\vec{K}_o - \vec{K}_A))\,\phi_\beta(-\tilde{B}\vec{K}_o - \vec{K}_B)\,\delta(\vec{K}_A + \vec{K}_B + \vec{k}) \quad . \qquad (A9)$$

The transition rate is given according to Golden rule No. 2 by

$$d\Gamma = \frac{2\pi}{\hbar}\,|\langle f|v|i\rangle|^2\, dN\, \delta(E_f - E_i) \qquad (A10)$$

where dN is the density of final states. For three free particles in the final state

$$dN = \frac{V^3}{(2\pi)^9}\, d^3K_A d^3K_B d^3k \quad . \qquad (A11)$$

Therefore the transition rate for emitting a nucleon of momentum $\vec{k}$ within the momentum element d^3k is

$$\frac{d\Gamma}{d^3k} = \frac{2\pi}{\hbar}\,|\langle f|v|i\rangle|^2\,\frac{V^3}{(2\pi)^9}\, d^3K_A d^3K_B\, \delta(E_f - E_i) \quad . \qquad (A12)$$

Substituting Eq. (A9) into Eq. (A12) yields

$$\frac{d\Gamma}{d^3k} = \frac{2\pi}{\hbar}\,\frac{v_o^2}{V^2}\, d^3K_A d^3K_B\,|\rho_{\alpha'\alpha}(\tilde{A}(\vec{K}_o - \vec{K}_A))|^2\,|\phi_\beta(-\tilde{B}\vec{K}_o - \vec{K}_B)|^2$$

$$\times\,\delta(\vec{K}_A + \vec{K}_B + \vec{k})\,\delta(\vec{K}_A + \vec{K}_B + \vec{k})\,\delta(E_f - E_i) \quad . \qquad (A13)$$

We sum over final states $\int d^3K_A d^3K_B$ and assume that the absorbed nucleon is reabsorbed into the same state $\alpha'=\alpha$. Performing the integration over d^3K_A gives

$$\frac{d\Gamma}{d^3k} = \frac{2\pi}{\hbar}\frac{v_o^2}{V^2}\int d^3K_B |\rho_{\alpha\alpha}(\tilde{A}(\vec{K}_o+\vec{K}_B+\vec{k}))|^2 |\phi_\beta(-\tilde{B}\vec{K}_o-\vec{K}_B)|^2\delta(\vec{0}) \times \delta(E_f-E_i) \quad (A14)$$

But $\delta(\vec{0})$ is evaluated as

$$\delta(\vec{0}) = \frac{1}{(2\pi)^3}\int d^3r = \frac{V}{(2\pi)^3} \quad (A15)$$

The transition rate then becomes

$$\frac{d\Gamma}{d^3k} = \frac{v_o^2}{(2\pi)^2\hbar V}\int d^3K_B |\rho_{\alpha\alpha}(\tilde{A}(\vec{K}_o+\vec{K}_B+\vec{k}))|^2 \times |\phi_\beta(-\tilde{B}\vec{K}_o-\vec{K}_B)|^2\delta(E_f-E_i) \quad (A16)$$

We average over initial states α and β noting that since the target and projectile are initially in their ground states the scattering can occur from A possible orbits in the projectile and B possible orbits in the target. Furthermore, we make a coherent average over the initial projectile states α since these states cannot be observed due to the reabsorption. The transition rate is then

$$\frac{d\Gamma}{d^3k} = \frac{v_o^2}{(2\pi)^2\hbar V}\int d^3K_B \left|\frac{1}{A}\sum_\alpha \rho_{\alpha\alpha}(\tilde{A}(\vec{K}_o+\vec{K}_B+\vec{k}))\right|^2 \times \frac{1}{B}\sum_\beta |\phi_\beta(-\tilde{B}\vec{K}_o-\vec{K}_B)|^2\delta(E_f-E_i) \quad (A17)$$

We then introduce the momentum distribution $P_B(\vec{q})$ of the target nucleons

$$P_B(\vec{q}) = \sum_\beta |\phi_\beta(\vec{q})|^2 \quad (A18)$$

and the density form factor $F_A(\vec{q})$ of the projectile nucleus

$$F_A(\vec{q}) = \sum_\alpha \rho_{\alpha\alpha}(\vec{q}) = \int d^3r\, e^{-i\vec{q}\cdot\vec{r}}\sum_\alpha |\phi_\alpha(\vec{r})|^2 . \quad (A19)$$

Dividing the transition rate by the incident flux density

$$|\vec{j}_{inc}| = \frac{(A+B)}{AB}\frac{\hbar K_o}{mV} \quad (A20)$$

yields the differential cross section for the knock-out of a nucleon from the target nucleus

$$\frac{d^2\sigma}{dEd\Omega} = \frac{m^2}{\hbar^4}\frac{k}{K_o}\frac{v_o^2}{(2\pi)^2}\frac{(A+B)^{-1}}{A}\int d^3K_B |F_A(\tilde{A}(\vec{K}_o+\vec{K}_B+\vec{k}))|^2 \times P_B(-\tilde{B}\vec{K}_o-\vec{K}_B)\delta(E_f-E_i) . \quad (A21)$$

The contribution of knock-out from the projectile (Fig. 35a) is similarly found to be

$$\frac{d^2\sigma}{dEd\Omega} = \frac{m^2}{\hbar^4}\frac{k}{K_o}\frac{v_o^2}{(2\pi)^2}\frac{(A+B)^{-1}}{B}\int d^3K_A |F_B(\tilde{B}(-\vec{K}_o+\vec{K}_A+\vec{k}))|^2 \times P_A(\tilde{A}\vec{K}_o-\vec{K}_A)\delta(E_f-E_i) . \quad (A22)$$

Combining Eqs. (A21) and (A22) the total differential cross section for single nucleon knock-out is given by

$$\frac{d^2\sigma}{dE d\Omega} = \frac{m^2}{\hbar^4}\frac{k}{K_o}\frac{v_o^2}{(2\pi)^2}(A+B)^{-1}\int d^3K\left[\frac{1}{A}|F_A(\tilde{A}(\vec{K}_o+\vec{K}+\vec{k}))|^2\right.$$
$$\times P_B(-\tilde{B}\vec{K}_o-\vec{K})\delta(E_f^B-E_i)+\frac{1}{B}|F_B(\tilde{B}(-\vec{K}_o+\vec{K}+\vec{k}))|^2$$
$$\left.\times P_A(\tilde{A}\vec{K}_o-\vec{K})\delta(E_f^A-E_i)\right] \qquad (A\ 23)$$

where the initial energy E_i is given by

$$E_i = \frac{(A+B)}{AB}\frac{\hbar^2K_o^2}{2m} \qquad (A\ 24)$$

and the final energies E_f^A and E_f^B are given as

$$E_f^A = \frac{\hbar^2}{2m}\left[\frac{K^2}{(A-1)}+\frac{(\vec{K}+\vec{k})^2}{B}+k^2\right]+E_o^A \qquad (A\ 25a)$$

and

$$E_f^B = \frac{\hbar^2}{2m}\left[\frac{(\vec{K}+\vec{k})^2}{A}+\frac{K^2}{(B-1)}+k^2\right]+E_o^B \qquad (A\ 25b)$$

where E_o^A and E_o^B are the binding energies of the nucleon removed from the projectile and target, respectively.

Equation (A23) can be evaluated after the momentum distribution $P(\vec{k})$ and the density form factor $F(\vec{q})$ are obtained within the framework of a suitable model of nuclear structure. It should be clear that $P(\vec{k})$ enters at the vertex of Fig. 35 where the nucleon is removed from the nucleus while $|F(\vec{q})|^2$ enters at the vertex where the other nucleon is removed but absorbed again.

Figure Captions

FIG. 1. Comparison of light particle energy spectra for reactions on ^{197}Au and ^{27}Al targets at 140 MeV incident energy. At each angle, the ^{27}Al data have been normalized to the ^{197}Au data at 20 MeV for the hydrogen isotopes and at 40 MeV for alpha-particles.

FIG. 2. Comparison of light particle energy spectra for reactions on ^{197}Au and ^{27}Al targets at 215 MeV incident energy. At each angle, the ^{27}Al data have been normalized to the ^{197}Au data at 20 MeV for the hydrogen isotopes and at 40 MeV for alpha-particles.

FIG. 3. Comparison of light particle energy spectra for reactions on ^{197}Au and ^{27}Al targets at 310 MeV incident energy. At each angle, the ^{27}Al data have been normalized to the ^{197}Au data at 20 MeV for the hydrogen isotopes and at 40 MeV for alpha-particles.

FIG. 4. Light particle angular distributions for reactions on ^{197}Au at 140, 215, and 310 MeV incident energies. The low-energy cut-offs for the energy integration are indicated. The dashed curves correspond to emission from a moving source with v = 0.071c and T = 5.9 MeV.

FIG. 5. Light particle angular distributions for reactions on ^{90}Zr at 215 and 310 MeV incident energies. The low-energy cut-offs for the energy integration are indicated. The dashed curves correspond to emission from a moving source with v = 0.072c and T = 5.73 MeV.

FIG. 6. Light particle angular distributions for reactions on ^{27}Al at 140, 215, and 310 MeV incident energies. The low-energy cut-offs for the energy integrations are indicated. The dashed curves correspond to emission from a moving source with v = 0.085c and T = 6.25 MeV.

Fig. 7. Dependence of proton and hydrogen multiplicity on target and incident energy. Multiplicities are taken from Table I of text. Errors reflect the 35% uncertainty of the absolute cross sections. The Coulomb barrier V_c has been calculated using Eq. (2).

FIG. 8. Energy spectra of protons in the $^{197}Au(^{16}O,p)$ reaction. The data are fitted with the moving source model of Eq. (3). The laboratory angles and the moving source parameters are indicated.

FIG. 9. Energy spectra of protons in the $^{90}Zr(^{16}O,p)$ reaction. The data are fitted with the moving source model of Eq. (3). The laboratory angles and the moving source parameters are indicated.

FIG. 10. Energy spectra of protons in the $^{27}Al(^{16}O,p)$ reaction. The data are fitted with the moving source model of Eq. (3). The laboratory angles and the moving source parameters are indicated.

FIG. 11. Parameter dependence of the reduced χ^2-value for the moving source fit of the reaction $^{197}Au(^{16}O,p)$ at 310 MeV (see Fig. 8). The variations of the reduced χ^2-value for independent variations of the temperature, velocity, and Coulomb parameters of Eq. (3) are shown.

FIG. 12. Energy spectra of deuterons in the $^{197}Au(^{16}O,d)$ reaction. The data are fitted with the moving source model of Eq. (3). The laboratory angles and the moving source parameters are indicated.

FIG. 13. Energy spectra of deuterons in the $^{90}Zr(^{16}O,d)$ reaction. The data are fitted with the moving source model of Eq. (3). The laboratory angles and the moving source parameters are indicated.

FIG. 14. Energy spectra of deuterons in the $^{27}Al(^{16}O,d)$ reaction. The data are fitted with the moving source model of Eq. (3). The laboratory angles and the moving source parameters are indicated.

FIG. 15. Energy spectra of tritons in the $^{197}Au(^{16}O,t)$ reaction. The data are fitted with the moving source model of Eq. (3). The laboratory angles and the moving source parameters are indicated.

FIG. 16. Energy spectra of tritons in the $^{90}Zr(^{16}O,t)$ reaction. The data are fitted with the moving source model of Eq. (3). The laboratory angles and the moving source parameters are indicated.

FIG. 17. Energy spectra of tritons in the $^{27}Al(^{16}O,t)$ reaction. The data are fitted with the moving source model of Eq. (3). The laboratory angles and the moving source parameters are indicated.

FIG. 18. Energy spectra of α-particles in the $^{197}Au(^{16}O,\alpha)$ reaction. The data are fitted with the moving source model of Eq. (3). The laboratory angles and the moving source parameters are indicated.

FIG. 19. Energy spectra of α-particles in the $^{90}Zr(^{16}O,\alpha)$ reaction. The data are fitted with the moving source model of Eq. (3). The laboratory angles and the moving source parameters are indicated.

FIG. 20. Energy spectra of α-particles in the $^{27}Al(^{16}O,\alpha)$ reaction. The data are fitted with the moving source model of Eq. (3). The laboratory angles and the moving source parameters are indicated.

FIG. 21. Incident energy and target dependence of the moving source temperature and velocity parameters are shown in parts (a) and (b) respectively. The Coulomb barrier, V_c, has been calculated using Eq. (2). The dependence expected for compound nucleus emission is indicated by the dashed curves. The solid curve in part (a) denoted by $T = T_{nn}$ was calculated according to Eq. (6). The solid curve marked $v = v_{nn}$ in part (b) was calculated using Eq. (7).

FIG. 22. Energy spectra of protons in the Ne+NaF reaction at incident energies of E/A = 400 and 800 MeV. The data (from ref. 40) are fitted with the relativistic moving source model of Eq. (8). The laboratory angles and the moving source parameters are indicated.

FIG. 23. Moving source temperature parameters for the proton, deuteron, and triton spectra in ^{16}O-induced reactions of the present study and for the reaction Ne+NaF → p at E/A = 400 and 800 MeV. The solid and dashed curves are described in the text.

FIG. 24. Energy spectra of protons in the $^{197}Au(^{16}O,p)$ reaction at 140, 215, and 310 MeV incident energy. The curves are the result of knock-out calculations described in the text.

FIG. 25. Energy spectra of protons in the $^{27}Al(^{16}O,p)$ reaction at 140, 215, and 310 MeV incident energy. The curves are the result of knock-out calculations described in the text.

FIG. 26. Angle-integrated proton spectra in the compound nucleus rest frame for the $^{197}Au(^{16}O,p)$ reaction at 140, 215, and 310 MeV incident energies. The calculated curves are described in the text.

FIG. 27. Incident energy and target dependence of the proton to deuteron ratio. The solid points were calculated with a common low-energy cut-off of 12 MeV. The open points were calculated with low-energy cut-offs near the detector threshold. The solid and dashed curves have been drawn to guide the eye.

FIG. 28. Energy spectra of light particles in reactions of 140 MeV ^{16}O on ^{197}Au. The open squares are spectra predicted by the coalescence model of Eq. (20).

FIG. 29. Energy spectra of light particles in reactions of 215 MeV ^{16}O on ^{197}Au. The open squares are spectra predicted by the coalescence model of Eq. (20).

FIG. 30. Energy spectra of light particles in reactions of 310 MeV ^{16}O on ^{197}Au. The open squares are spectra predicted by the coalescence model of Eq. (20).

FIG. 31. Energy spectra of light particles in reactions of 140 MeV ^{16}O on ^{27}Al. The open squares are spectra predicted by the coalescence model of Eq. (20).

FIG. 32. Energy spectra of light particles in reactions of 215 MeV ^{16}O on ^{27}Al. The open squares are spectra predicted by the coalescence model of Eq. (20).

FIG. 33. Energy spectra of light particles in reactions of 310 MeV ^{16}O on ^{27}Al. The open squares are spectra predicted by the coalescence model of Eq. (20).

FIG. 34. Energy spectra of deuterons and tritons in reactions of ^{16}O on ^{90}Zr at 215 and 310 MeV incident energy. The solid curves are spectra predicted by the coalescence model of Eq. (20).

FIG. 35. Processes calculated in knock-out model. Part (a) represents knock-out from the projectile. Knock-out from the target is represented in part (b).

References

1. Y. Eyal, A. Gavron, I. Tserruya, Z. Fraenkel, Y. Eisen, S. Wald, R. Bass, G.R. Gould, G. Kreyling, R. Renfordt, K. Stelzer, R. Zitzmann, A. Gobbi, A. Lynen, H. Stelzer, I. Rode, and R. Bock, Phys. Rev. Lett. 41, 625 (1978).
2. D. Hilscher, J.R. Birkelund, A.D. Hoover, W.U. Schröder, W.W. Wilcke, J.R. Huizenga, A.C. Mignerey, K.L. Wolf, H.F. Breuer, and V.E. Viola, Jr., Phys. Rev. C20, 576 (1979).
3. B. Tamain, R. Chechik, H. Fuchs, F. Hanappe, M. Morjean, C. Ngô, J. Péter, M. Dakowski, B. Lucas, C. Mazur, M. Ribrag, and C. Signarbieux, Nucl. Phys. A330, 253 (1979).
4. C.R. Gould, R. Bass, J.v. Czarnecki, V. Hartmann, K. Stelzer, R. Zitzmann, and Y. Eyal, Z. Phys. A294, 323 (1980).
5. D.L. Hillis, O. Christensen, B. Fernandez, A.J. Ferguson, J.D. Garrett, G.B. Hagemann, B. Herskind, B.B. Back, and F. Folkmann, Phys. Lett. 78B, 405 (1978).
6. L. Westerberg, D.G. Sarantites, D.C. Hensley, R.A. Dayras, M.L. Halbert, and J.H. Barker, Phys. Rev. C18, 796 (1978).
7. H. Gemmeke, P. Netter, Ax. Richter, L. Lassen, S. Lewandowski, W. Lücking, and R. Schreck, Phys. Lett. 97B, 213 (1980).

8. A. Gavron, R.L. Ferguson, Felix E. Obenshain, F. Plasil, G.R. Young, G.A. Petitt, K. Geoffroy Young, D.G. Sarantites, and C.F. Maguire, Phys. Rev. Lett. 46, 8 (1981).
9. I. Tserruya, A. Breskin, R. Chechik, Z. Fraenkel, S. Wald, N. Zwang, R. Bock, M. Dakowski, A. Gobbi, H. Sann, R. Bass, G. Kreyling, R. Renfordt, K. Stelzer, and U. Arlt, Phys. Rev. Lett. 47, 16 (1981).
10. J.R. Beene, M.L. Halbert, D.C. Hensley, R.A. Dayras, K. Geoffroy Young, D.G. Sarantites, and J.H. Barker, Phys. Rev. C23, 2463 (1981).
11. K. Geoffroy Young, D.G. Sarantites, J.R. Beene, M.L. Halbert, D.C. Hensley, R.A. Dayras, and J.H. Barker, Phys. Rev. C23, 2479 (1981).
12. J. Kasagi, S. Saini, T.C. Awes, A. Galonsky, C.K. Gelbke, G. Poggi, D.K. Scott, K.L. Wolf, and R.L. Legrain, Phys. Lett. 104B, 434 (1981).
13. H.C. Britt and A.R. Quinton, Phys. Rev. 124, 877 (1961).
14. J.B. Ball, C.B. Fulmer, M.L. Mallory, and R.L. Robinson, Phys. Rev. Lett. 40, 1698 (1978).
15. T.J.M. Symons, P. Doll, M. Bini, D.L. Hendrie, J. Mahoney, G. Mantzouranis, D.K. Scott, K. Van Bibber, Y.P. Viyogi, H.H. Wieman, and C.K. Gelbke, Phys. Lett. 94B, 131 (1980).
16. J.W. Harris, T.M. Cormier, D.F. Gesaman, L.L. Lee, Jr., R.L. McGrath, and J.P. Wurm, Phys. Rev. Lett. 38, 1460 (1977).

17. H. Ho, R. Albrecht, W. Dünnweber, G. Graw, S.G. Steadman, J.P. Wurm, D. Disdier, V. Rauch, and F. Scheibling, Z. Phys. A283, 235 (1977).

18. C.K. Gelbke, M. Bini, C. Olmer, D.L. Hendrie, J.L. Laville, J. Mahoney, M.C. Mermaz, D.K. Scott, and H.H. Wieman, Phys. Lett. 71B, 83 (1977).

19. A. Gamp, J.C. Jacmart, N. Poffé, H. Doubre, J.C. Roynette, and J. Wilczyński, Phys. Lett. 74B, 215 (1978).

20. R.K. Bhowmik, E.C. Pollacco, N.E. Sanderson, J.B.A. England, G.C. Morrison, Phys. Rev. Lett. 43, 619 (1979).

21. H. Ho, P. Gonthier, M.N. Namboodiri, J.B. Natowitz, L. Adler, S. Simon, K. Hagel, R. Terry and A. Khodai, Phys. Lett. 96B, 51 (1980).

22. T. Nomura, H. Utsunomiya, T. Motobayashi, T. Inamura, and M. Yanokura, Phys. Rev. Lett. 40, 694 (1978).

23. H. Utsunomiya, T. Nomura, T. Inamura, T. Sugitate, and T. Motobayashi, Nucl. Phys. A334, 127 (1980).

24. J.H. Barker, J.R. Beene, M.L. Halbert, D.C. Hensley, M. Jääskeläinen, D.G. Sarantites, and R. Woodward, Phys. Rev. Lett. 45, 424 (1980).

25. T. Inamura, M. Ishihara, T. Fukuda, T. Shimoda, and H. Hiruta, Phys. Lett. 68B, 51 (1977).

26. D.R. Zolnowski, H. Yamada, S.E. Cala, A.C. Kahler, and T.T. Sugihara, Phys. Rev. Lett. 41, 92 (1978).

27. H. Yamada, D.R. Zolnowski, S.E. Cala, A.C. Kahler, J. Pierce, and T.T. Sugihara, Phys. Rev. Lett. 43, 605 (1979).

28. K. Siwek-Wilczyńska, E.H. du Marchie van Voorthuysen, J. van Popta, R.H. Siemssen, and J. Wilczyński, Phys. Rev. Lett. 42, 1599 (1979); Nucl. Phys. A330, 150 (1979).

29. T.C. Awes, C.K. Gelbke, B.B. Back, A.C. Mignerey, K.L. Wolf, P. Dyer, H. Breuer, and V.E. Viola, Jr., Phys. Lett. 87B, 43 (1979).

30. B.B. Back, K.L. Wolf, A.C. Mignerey, C.K. Gelbke, T.C. Awes, H. Breuer, V.E. Viola, Jr., and P. Dyer, Phys. Rev. C22, 1927 (1980).

31. T.C. Awes, G. Poggi, C.K. Gelbke, B.B. Back, B.G. Glagola, H. Breuer, and V.E. Viola, Jr., Phys. Rev. C24, 89 (1981).

32. M. Bini, C.K. Gelbke, D.K. Scott, T.J.M. Symons, P. Doll, D.L. Hendrie, J.L. Laville, J. Mahoney, M.C. Mermaz, C. Olmer, K. Van Bibber, and H.H. Wieman, Phys. Rev. C22, 1945 (1980).

33. G.R. Young, R.L. Ferguson, A. Gavron, D.C. Hensley, Felix E. Obenshain, F. Plasil, A.H. Snell, M.P. Webb, C.F. Maguire, and G.A. Petitt, Phys. Rev. Lett. 45, 1389 (1980).

34. R.P. Schmitt, G.J. Wozniak, G.U. Rattazzi, G.J. Mathews, R. Regimbart, and L.G. Moretto, Phys. Rev. Lett. 46, 522 (1981).

35. T.C. Awes, G. Poggi, S. Saini, C.K. Gelbke, R. Legrain, and G.D. Westfall, Phys. Lett. 103B, 417 (1981).

36. C.B. Fulmer, J.B. Ball, R.L. Ferguson, R.L. Robinson, and J.R. Wu, (unpublished).

37. R.L. Auble, J.B. Ball, F.E. Bertrand, R.L. Ferguson, C.B. Fulmer, I.Y. Lee, R.L. Robinson, G.R. Young, J.R. Wu, J.C. Wells, and H. Yamada (unpublished).

38. J. Gosset, H.H. Gutbrod, W.G. Meyer, A.M. Poskanzer, A. Sandoval, R. Stock, and G.D. Westfall, Phys. Rev. C16, 629 (1977).

39. A. Sandoval, H.H. Gutbrod, W.G. Meyer, R. Stock, Ch. Lukner, A.M. Poskanzer, J. Gosset, J.-C. Jourdain, C.H. King, G. King, Nguyen Van Sen, G.D. Westfall, and K.L. Wolf, Phys. Rev. C21, 1321 (1980).

40. S. Nagamiya, M.-C. Lemaire, E. Moeller, S. Schnetzer, G. Shapiro, H. Steiner, and I. Tanihata, Phys. Rev. C24, 971 (1981).

41. G.D. Westfall, J. Gosset, P.J. Johansen, A.M. Poskanzer, W.G. Meyer, H.H. Gutbrod, A. Sandoval, and R. Stock, Phys. Rev. Lett. 37, 1202 (1976).

42. W.D. Myers, Nucl. Phys. A296, 177 (1978).

43. S.E. Koonin, Phys. Rev. Lett. 39, 680 (1977).

44. R.L. Hatch and S.E. Koonin, Phys. Lett. 81B, 1 (1979).

45. M. Chemtob and B. Schürmann, Nucl. Phys. A336, 508 (1980).

46. J. Hüfner and J. Knoll, Nucl. Phys. A290, 460 (1977).

47. J. Randrup, Phys. Lett. 76B, 547 (1978).

48. J. Cugnon, J. Knoll, and J. Randrup, Nucl. Phys. A360, 444 (1981).

49. Y. Yariv and Z. Fraenkel, Phys. Rev. C20, 2227 (1979); Phys. Rev. C24, 488 (1981).

50. J. Cugnon, Phys. Rev. C22, 1885 (1980).

51. R. Weiner and M. Weström, Nucl. Phys. A286, 282 (1977).

52. P.A. Gottschalk, and M. Weström, Phys. Rev. Lett. 39, 1250 (1977); Nucl. Phys. A314, 232 (1979).

53. S.I.A. Garpman, D. Sperber, and M. Zielińska-Pfabe, Phys. Lett. 90B, 53 (1980).

54. S.I.A. Garpman, S.K. Samaddar, D. Sperber, and M. Zielińska-Pfabe, Phys. Lett. 92B, 56 (1980).

55. W.W. Morison, S.K. Samaddar, D. Sperber, and M. Zielińska-Pfabe, Phys. Lett. 93B, 379 (1980).

56. P. Mooney, W.W. Morison, S.K. Samaddar, D. Sperber and M. Zielińska-Pfabe, Phys. Lett. 98B, 240 (1981).

57. J.P. Bondorf, J.N. De, A.O.T. Karvinen, G. Fái, and B. Jakobsson, Phys. Lett. 84B, 162 (1979).

58. J.P. Bondorf, J.N. De, G. Fái, A.O.T. Karvinen, B. Jacobsson, and J. Randrup, Nucl. Phys. A333, 285 (1980).

59. H.W. Bertini, R.T. Santoro, and O.W. Hermann, Phys. Rev. C14, 590 (1976).

60. M. Blann, Ann. Rev. Nucl. Sci. 25, 123 (1975).

61. M. Blann, Phys. Rev. C23, 205 (1981).

62. G. Mantzouranis, H.A. Weidenmüller, and D. Agassi, Z. Phys. A276, 145 (1976).

63. T.C. Awes, C.K. Gelbke, G. Poggi, B.B. Back, B. Glagola, H. Breuer, V.E. Viola, Jr., T.J.M. Symons, Phys. Rev. Lett. 45, 513 (1980).

64. F.S. Goulding and B.G. Harvey, Ann. Rev. Nucl. Sci. 25, 167 (1975).

65. J.G. Cramer, (unpublished).

66. J.B. Ball, C.B. Fulmer, E.E. Gross, M.L. Halbert, D.C. Hensley, C.A. Ludemann, M.J. Saltmarsh, and G.R. Satchler, Nucl. Phys. A252, 208 (1975).

67. K.E. Rehm, J.J. Körner, M. Richter, H.P. Rother, J.P. Schiffer, and H. Spieler, Phys. Rev. C12, 1945 (1975).

68. J.G. Cramer, R.M. DeVries, D.A. Goldberg, M.S. Zisman, and C.F. Maguire, Phys. Rev. C14, 2158 (1976).

69. J.B. Natowitz, M.N. Namboodiri, L. Adler, R.P. Schmitt, R.L. Watson, S. Simon, M. Berlanger, and R. Choudhury, Phys. Rev. Lett. 47, 1114 (1981).

70. B. Jakobsson, L. Carlen, P. Kristiansson, J. Krumlinde, A. Oskarsson, I. Otterlund, B. Schrøder, H.Å. Gustafsson, T. Johansson, H. Ryde, G. Tibell, J.P. Bondorf, G. Fái, A.O.T. Karvinen, O.B. Nielsen, M. Buenerd, J. Cole, D. Lebrun, J.M. Loiseaux, P. Martin, R. Ost, P. De Saintignon, C. Guet, E. Monnand, J. Mougey, H. Nifenecker, P. Perrin, J. Pinston, C. Ristori, and F. Schussler, Phys. Lett. 102B, 121 (1981).

71. K.R. Cordell, S.T. Thornton, L.C. Dennis, R.R. Doering, R.L. Parks, and T.C. Schweizer, Nucl. Phys. A362, 431 (1981).

72. H. Machner, Phys. Lett. 86B, 129 (1979); Phys. Rev. C21 (1980) 2695.

73. These values are very similar to the ones obtained by performing a slope analysis.[60,74] In this analysis a graph of $\ln[(d\sigma/dE)/E\sigma_{inv}]$ versus $\ln[U]$, where σ_{inv} is the inverse cross section and $U = E^{*}-E_{b}-E$ is the residual excitation energy, yields a line of slope n_o-2 and gives n_o values of about 19, 26 and 31 at 140, 215, and 310 MeV, respectively.

74. J.J. Griffin, Phys. Lett. 24B, 5 (1967).

75. R. Bass, Nucl. Phys. A231, 45 (1974).

76. P.J. Siemens and J.I. Kapusta, Phys. Rev. Lett. 43, 1486 (1979).

77. I.M. Mishustin, F. Myhrer, and P.J. Siemens, Phys. Lett. 95B, 361 (1980).

78. P.J. Siemens, (private communication).

79. H. Stöcker, Lawrence Berkeley Laboratory Preprint, LBL-12302 (1980).

80. F. Hachenberg, H.C. Chiang, and J. Hüfner, Phys. Lett. 97B, 183 (1980).

81. F. Pühlhofer, Nucl. Phys. A280, 267 (1977).

82. M.-C. Lemaire, S. Nagamiya, S. Schnetzer, H. Steiner, and I. Tanihata, Phys. Lett. 85B, 38 (1979).

83. A. Schwarzschild and Č. Zupančič, Phys. Rev. 129, 854 (1963).

84. A. Mekjian, Phys. Lett. 89B, 177 (1980).

85. J.I. Kapusta, Phys. Rev. C21, 1301 (1980).

86. H. Sato and K. Yazaki, Phys. Lett. 98B, 153 (1981).

87. H. Löhner, B. Ludewigt, D. Frekers, G. Gaul and R. Santo, Z. Phys. A292, 35 (1979).

Table I. Total inclusive cross sections (mb) for light particle emission. Systematic errors of absolute values are about 35%. Relative errors between light particle species are about 10%.

Target	Energy (MeV)	Protons[a]	Deuterons[a]	Tritons[a]	Hydrogen Isotopes[a]	Alphas[b]	σ_R[c]
^{197}Au	140	76	15	8	99	72	2259
	215	327	85	65	477	241	3075
	310	1414	497	340	2251	1162	3520
^{90}Zr	215	545	119	49	713	191	2487
	310	1971	649	304	2924	1448	2642
^{27}Al	140	253	58	14	325	140	1742
	215	528	172	52	752	524	1820
	310	1155	437	158	1750	1781	1846

a) Integrated over E>12 MeV

b) Integrated over E>30 MeV

c) Total reaction cross sections calculated using the optical model code HOP II[65] with the parameters of Table II.

Table II. Optical model potential parameters used in calculaton of total reaction cross sections (units of MeV and fm). The optical potential was parameterized in the form: $U(r) = V_o\{1+\exp[(r-R_o)/a_o]\}^{-1} + W_o\{1+\exp[(r-R_I)/a_I]\}^{-1}$, with $R_o = r_o(A_1^{1/3} + A_2^{1/3})$, $R_I = r_I(A_1^{1/3} + A_2^{1/3})$.

Target	V_o	r_o	a_o	W_o	r_I	a_I
^{197}Au[a]	40	1.226	.634	35	1.226	.634
^{90}Zr[b]	100	1.148	.635	20	1.245	.521
^{27}Al[c]	10	1.35	.618	23.4	1.23	.552

a) Potential of Ref. 66 for elastic scattering of ^{16}O on ^{208}Pb.

b) Potential of Ref. 67 for elastic scattering of ^{16}O on ^{92}Mo.

c) Potential of Ref. 68 for elastic scattering of ^{16}O on ^{28}Si.

Table III. Moving source parameters used in calculations of Figs. 8-20.

Target	Energy(MeV)	Particle	N_o [a]	v/c [b]	T(MeV) [c]	σ (mb) [d]
^{197}Au	140	p	2.01	.067	3.08	121
	140	d	.28	.066	3.43	20
	140	t	.146	.055	3.52	11
	140	α	2.74	.060	2.97	156
	215	p	4.32	.054	4.40	444
	215	d	.71	.055	5.34	98
	215	t	.519	.052	5.60	77
	215	α	3.04	.069	4.72	347
	310	p	9.62	.071	5.90	1535
	310	d	2.28	.076	7.10	480
	310	t	1.34	.071	7.60	313
	310	α	4.38	.088	6.94	892
^{90}Zr	215	p	12.7	.053	4.54	1368
	215	d	1.47	.060	5.62	218
	215	t	.474	.059	6.23	82
	215	α	4.02	.066	5.67	604
	310	p	22.4	.072	5.73	3421
	310	d	3.86	.078	7.23	836

Table III. (con't.)

Target	Energy(MeV)	Particle	N_o [a]	v/c [b]	T(MeV) [c]	σ (mb) [d]
	310	t	1.34	.073	8.16	348
	310	α	6.47	.087	8.22	1598
^{27}Al	140	p	19.0	.049	3.96	1667
	140	d	1.91	.054	4.55	206
	140	t	.284	.055	5.05	36
	140	α	14.7	.068	4.26	1439
	215	p	13.3	.074	5.14	1726
	215	d	2.40	.079	5.90	383
	215	t	.460	.080	6.74	90
	215	α	11.7	.088	5.85	1844
	310	p	15.2	.085	6.25	2645
	310	d	3.33	.089	7.23	721
	310	t	.834	.091	8.10	214
	310	α	13.6	.114	7.39	3042

a) Units of $mb/((MeV)^{3/2}\ sr)$

b) Typically ±10% uncertainty

c) Typically ±5% uncertainty

d) Calculated using Eq. (5) of text.

MSUX-81-060

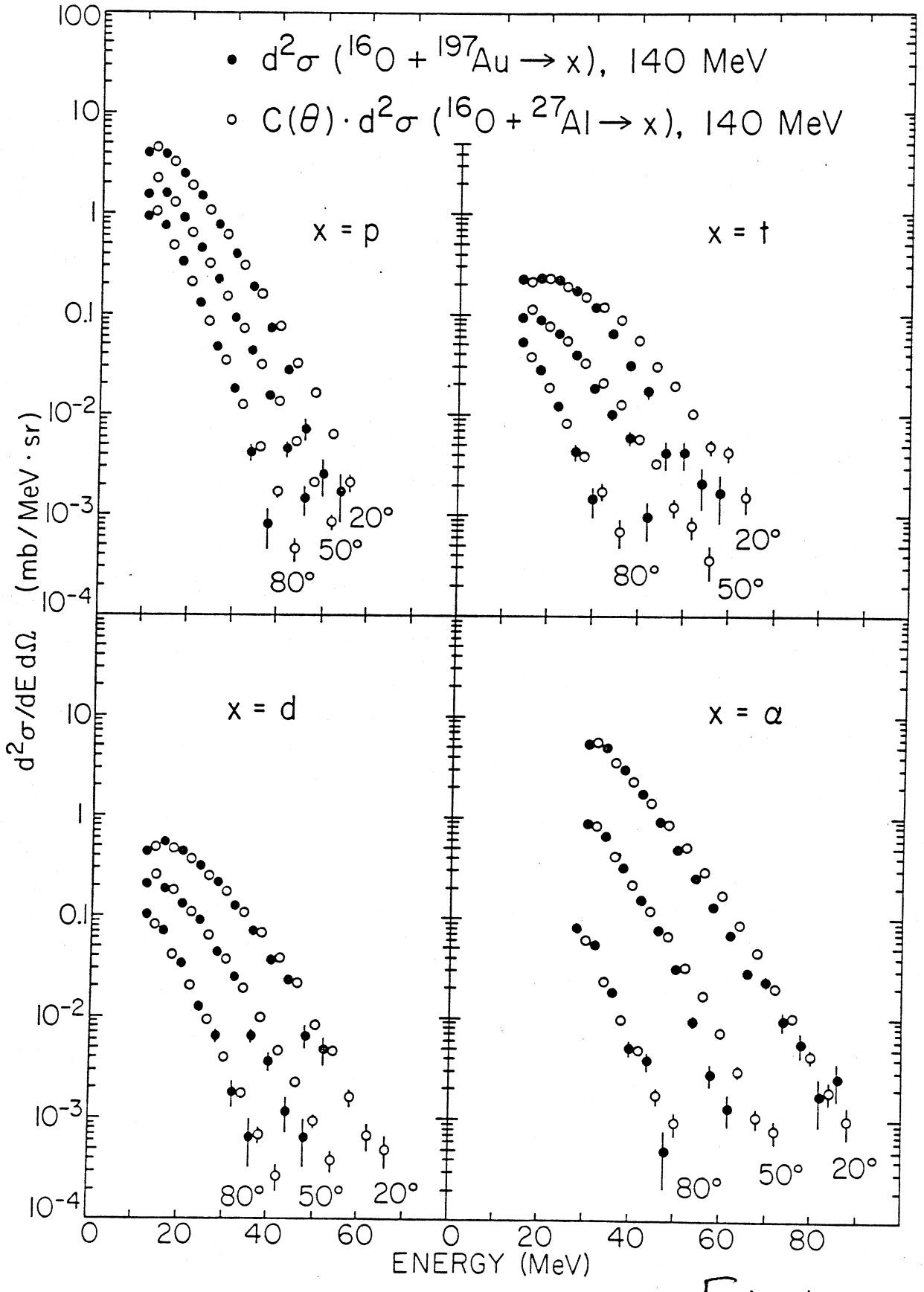

Fig. 1

MSUX-81-009

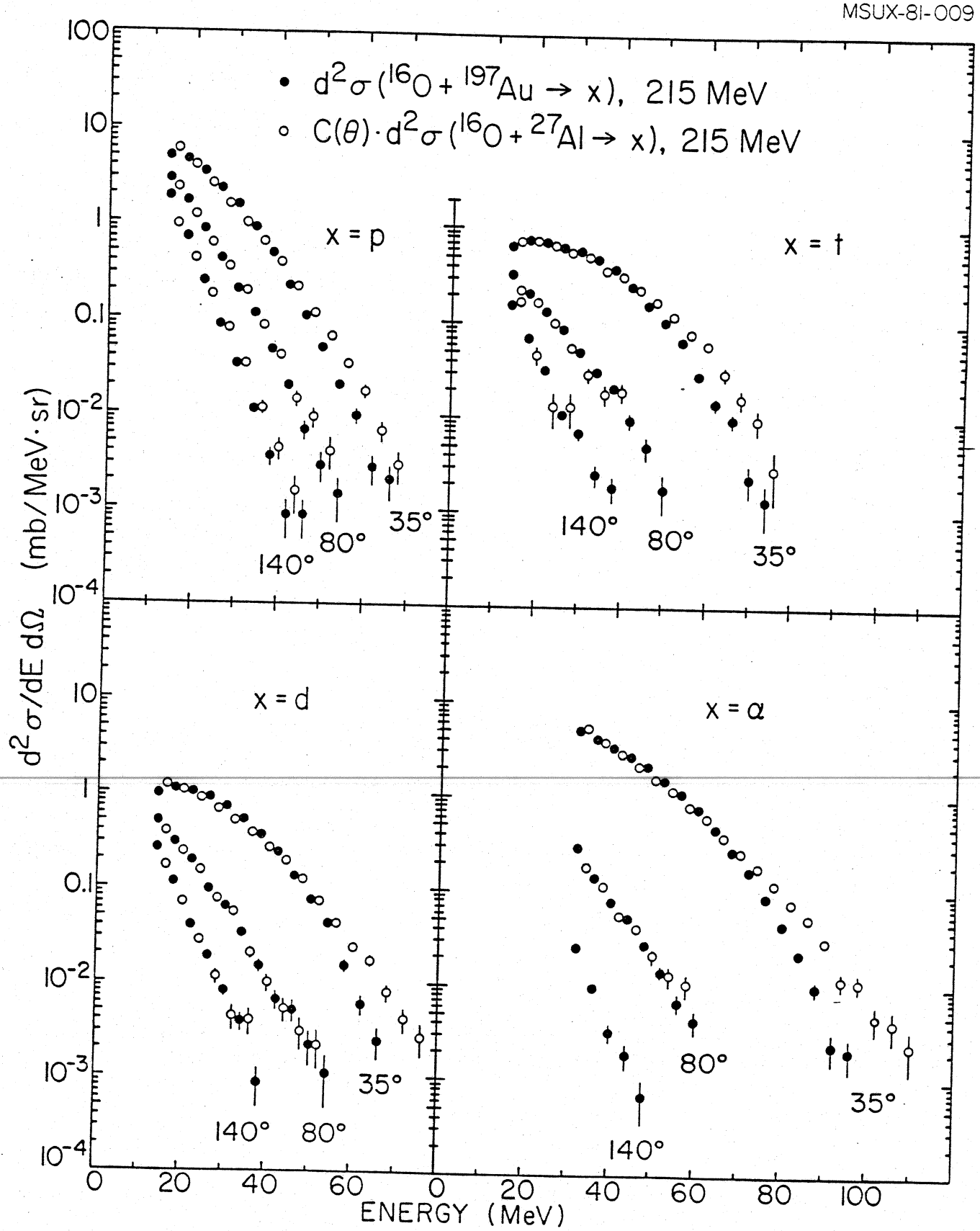

Fig. 2

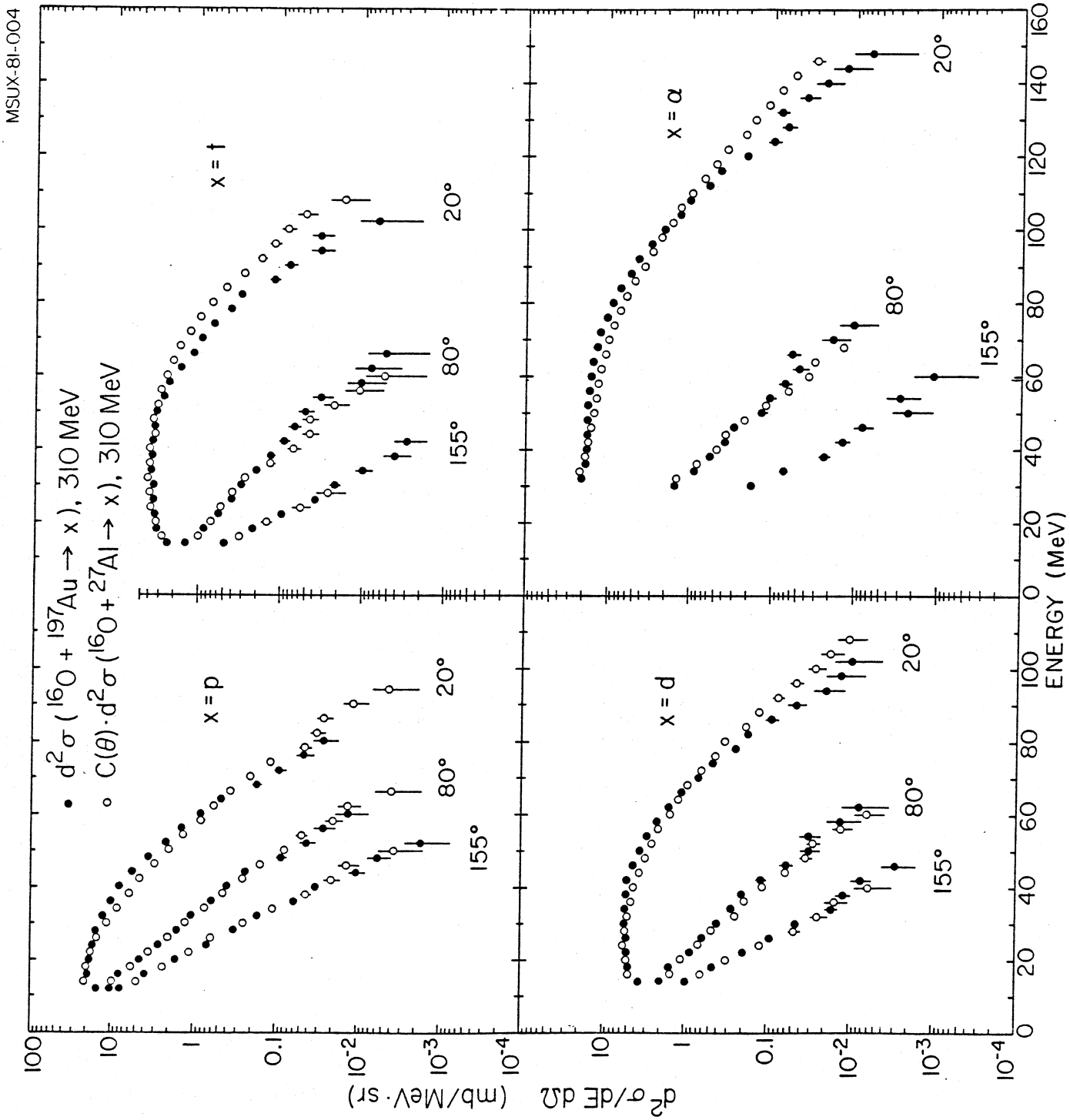
MSUX-81-004
• $d^2\sigma(^{16}O + ^{197}Au \rightarrow x)$, 310 MeV
○ $C(\theta) \cdot d^2\sigma(^{16}O + ^{27}Al \rightarrow x)$, 310 MeV
x = p
x = t
x = d
x = α
20°
80°
155°
$d^2\sigma/dE\,d\Omega$ (mb/MeV·sr)
ENERGY (MeV)

Fig. 3

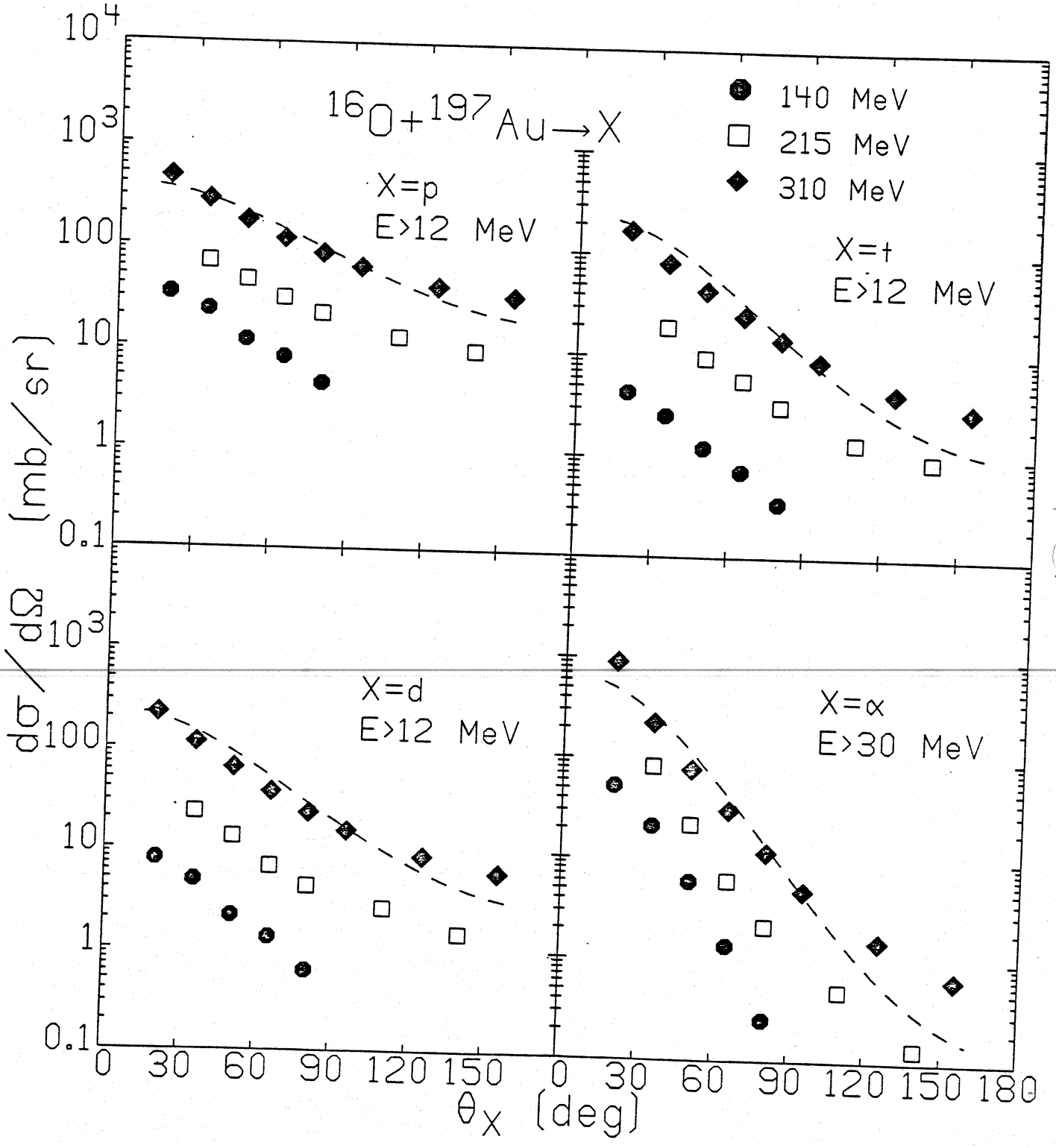
$^{16}O+^{197}Au \rightarrow X$
140 MeV
215 MeV
310 MeV
X=p
E>12 MeV
X=t
E>12 MeV
X=d
E>12 MeV
X=α
E>30 MeV
dσ/dΩ (mb/sr)
θ_X (deg)
10^4
10^3
100
10
1
0.1
0 30 60 90 120 150
0 30 60 90 120 150 180

Fig. 4

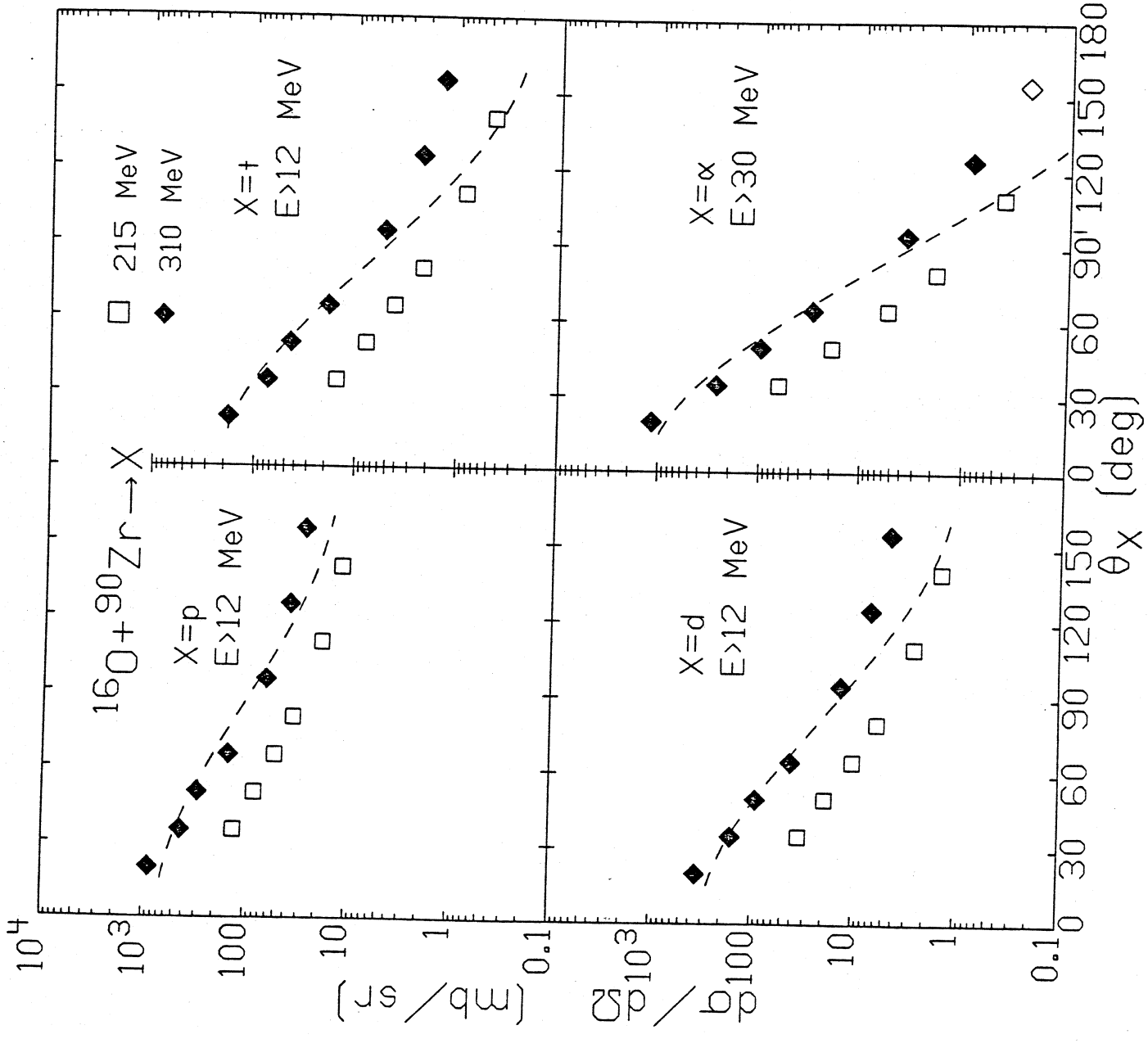
$^{16}O+^{90}Zr \rightarrow X$
215 MeV
310 MeV
X=p
E>12 MeV
X=t
E>12 MeV
X=d
E>12 MeV
X=α
E>30 MeV
$\frac{d\sigma}{d\Omega}$ (mb/sr)
$\frac{d\sigma}{d\Omega}\cdot 10^3$ (mb/sr)
θ_X (deg)
0 30 60 90 120 150
0 30 60 90 120 150 180
0.1
1
10
100
10^3
10^4

Fig. 5

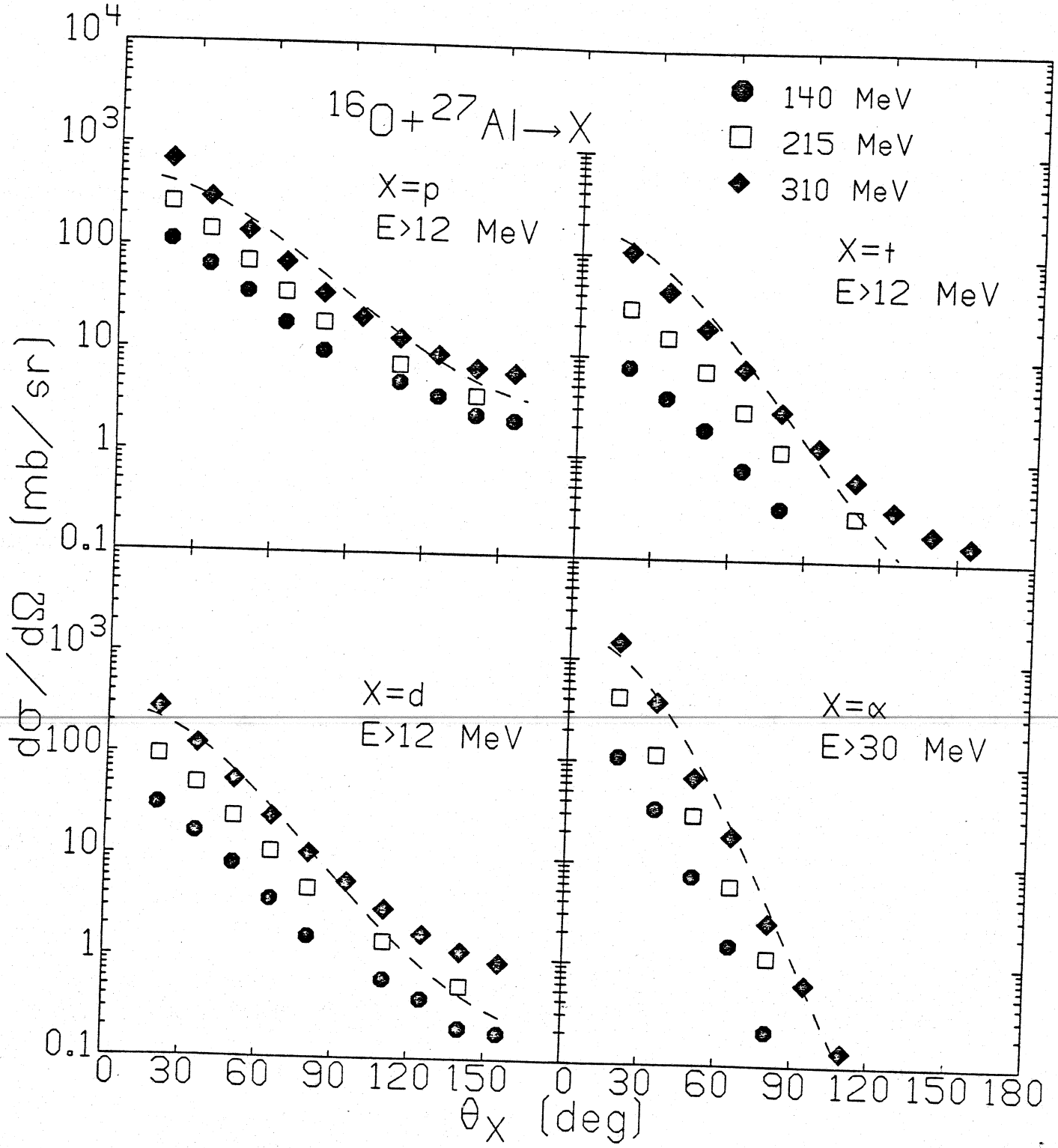
$^{16}O+^{27}Al \rightarrow X$
140 MeV
215 MeV
310 MeV
X=p
E>12 MeV
X=t
E>12 MeV
X=d
E>12 MeV
X=α
E>30 MeV
$d\sigma/d\Omega$ (mb/sr)
θ_X (deg)
10^4
10^3
100
10
1
0.1
0 30 60 90 120 150
0 30 60 90 120 150 180

Fig. 6

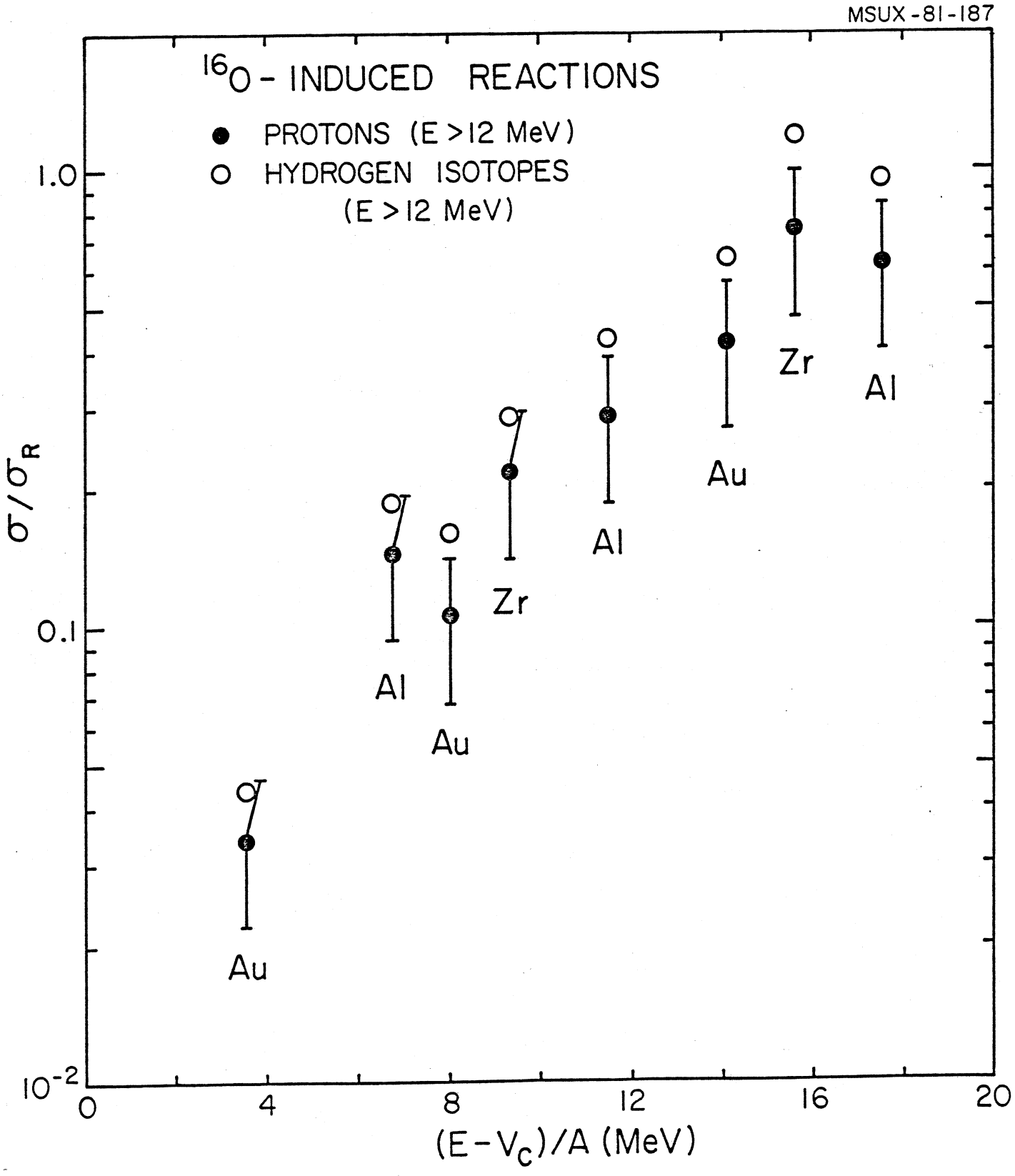
MSUX-81-187
^{16}O - INDUCED REACTIONS
PROTONS (E > 12 MeV)
HYDROGEN ISOTOPES (E > 12 MeV)
1.0
0.1
10^{-2}
σ/σ_R
Au
Al
Au
Zr
Al
Au
Zr
Al
0
4
8
12
16
20
$(E-V_c)/A$ (MeV)

Fig. 7

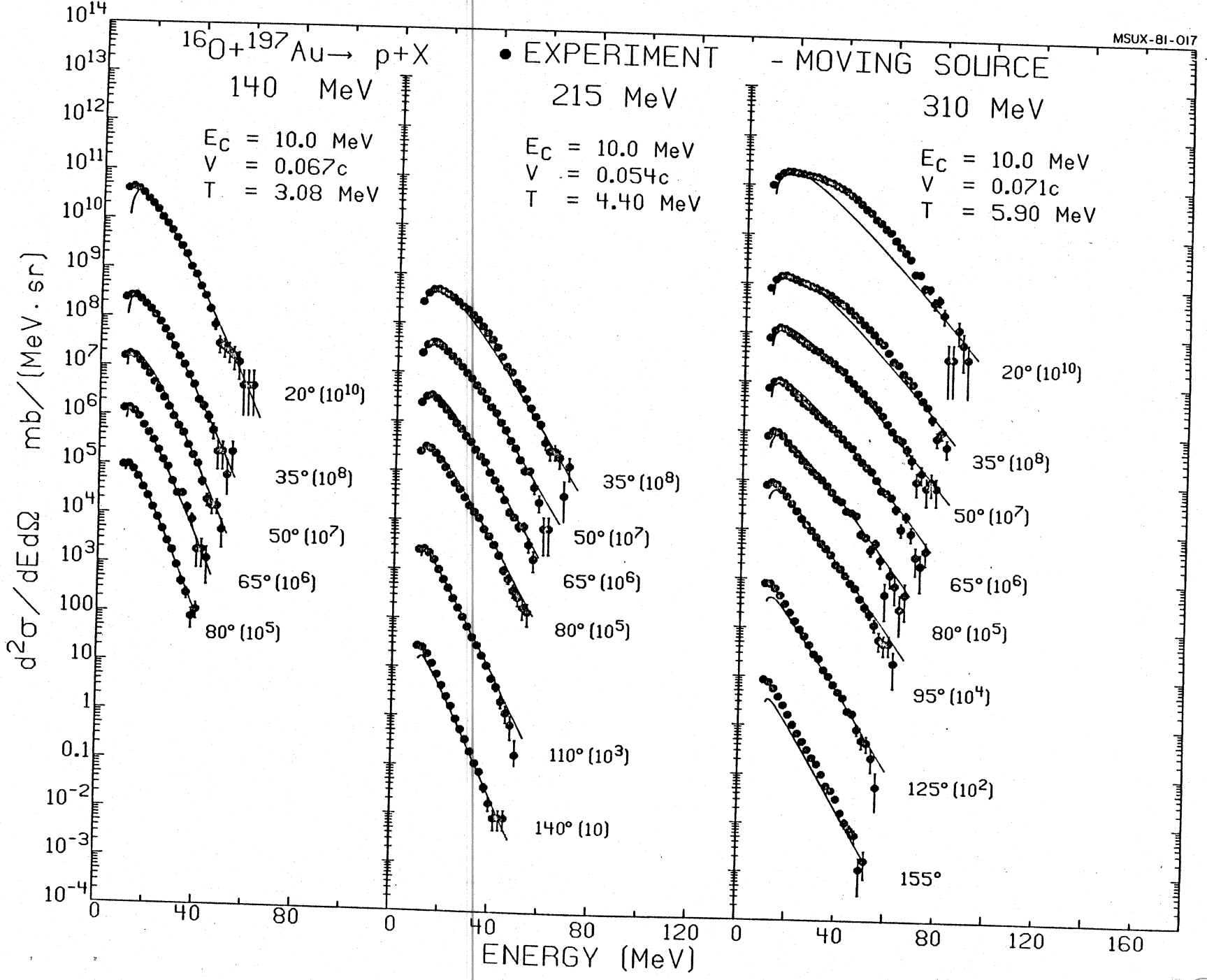
MSUX-81-017
$^{16}O+^{197}Au \rightarrow p+X$
• EXPERIMENT - MOVING SOURCE
140 MeV
E_C = 10.0 MeV
V = 0.067c
T = 3.08 MeV
215 MeV
E_C = 10.0 MeV
V = 0.054c
T = 4.40 MeV
310 MeV
E_C = 10.0 MeV
V = 0.071c
T = 5.90 MeV
$d^2\sigma/dEd\Omega$ mb/(MeV·sr)
ENERGY (MeV)
20° (10^{10})
35° (10^8)
50° (10^7)
65° (10^6)
80° (10^5)
95° (10^4)
110° (10^3)
125° (10^2)
140° (10)
155°

Fig. 8

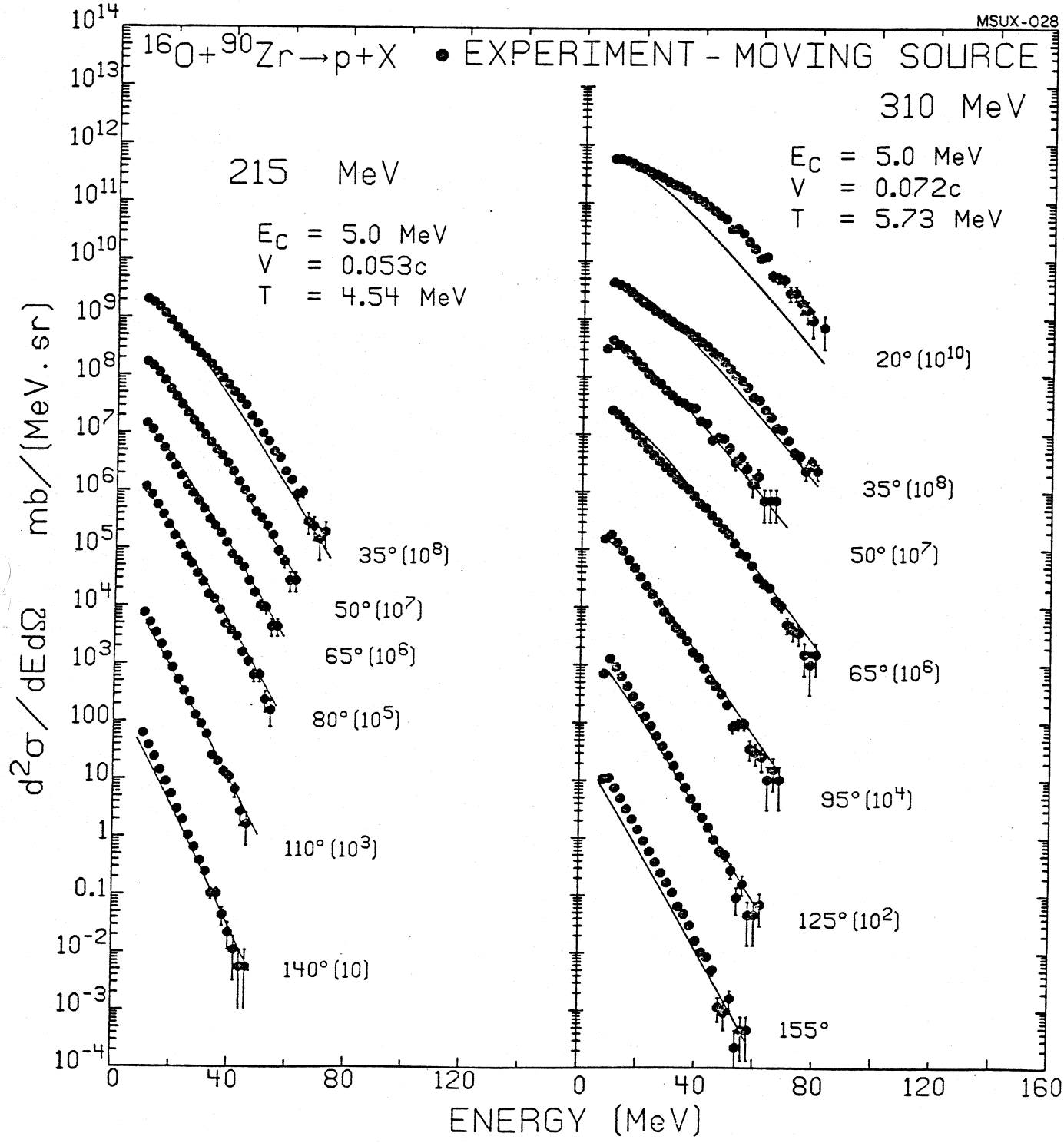
MSUX-028
$^{16}O+^{90}Zr \rightarrow p+X$ • EXPERIMENT - MOVING SOURCE
215 MeV
E_C = 5.0 MeV
V = 0.053c
T = 4.54 MeV
35° (10^8)
50° (10^7)
65° (10^6)
80° (10^5)
110° (10^3)
140° (10)
310 MeV
E_C = 5.0 MeV
V = 0.072c
T = 5.73 MeV
20° (10^{10})
35° (10^8)
50° (10^7)
65° (10^6)
95° (10^4)
125° (10^2)
155°
$d^2\sigma / dEd\Omega$ mb/(MeV.sr)
ENERGY (MeV)

Fig. 9

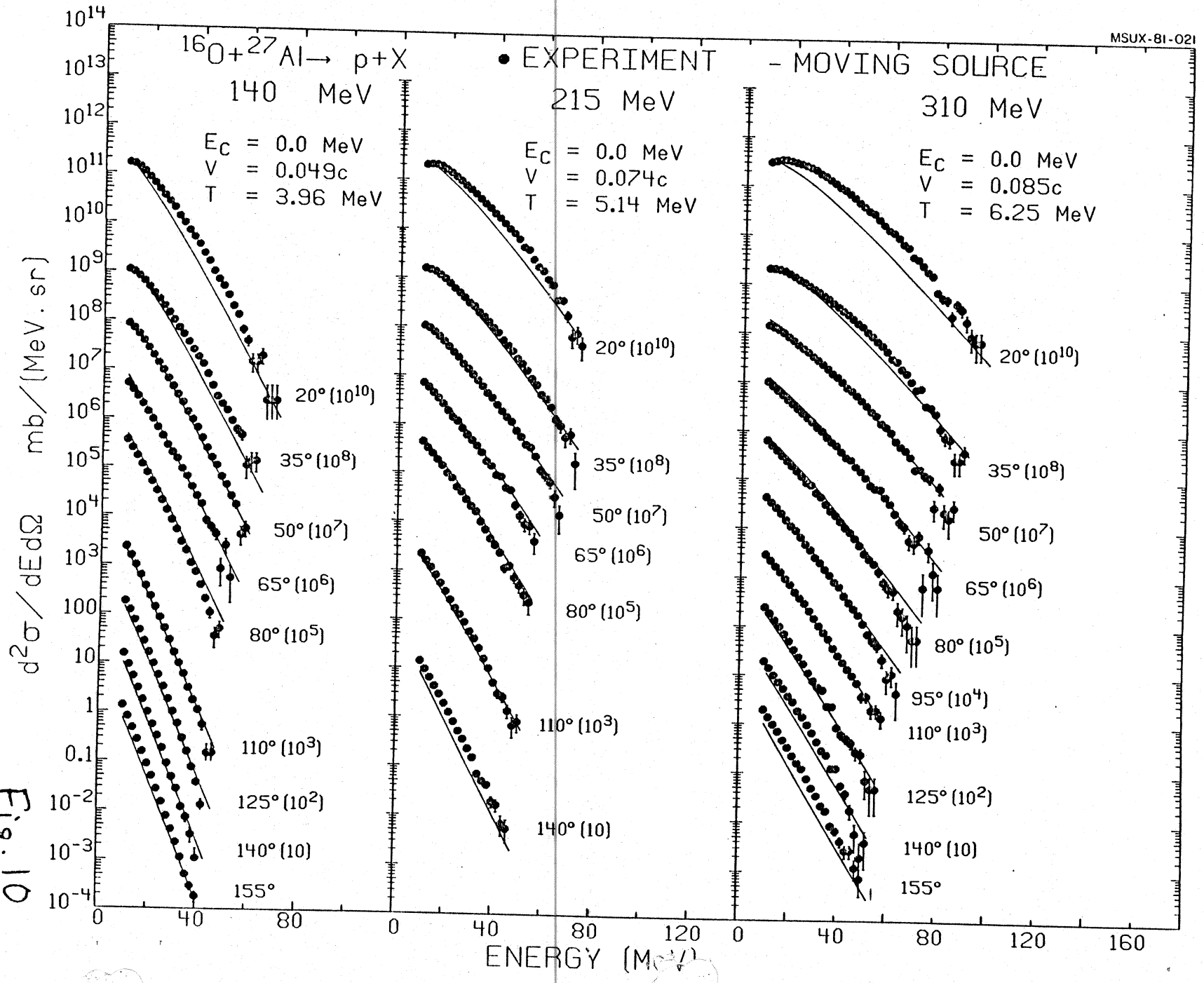
MSUX-81-021
$^{16}O+^{27}Al \rightarrow p+X$
• EXPERIMENT - MOVING SOURCE
140 MeV
E_C = 0.0 MeV
V = 0.049c
T = 3.96 MeV
215 MeV
E_C = 0.0 MeV
V = 0.074c
T = 5.14 MeV
310 MeV
E_C = 0.0 MeV
V = 0.085c
T = 6.25 MeV
20° (10^{10})
35° (10^8)
50° (10^7)
65° (10^6)
80° (10^5)
95° (10^4)
110° (10^3)
125° (10^2)
140° (10)
155°
$d^2\sigma/dEd\Omega$ mb/(MeV·sr)
ENERGY (MeV)

Fig. 10

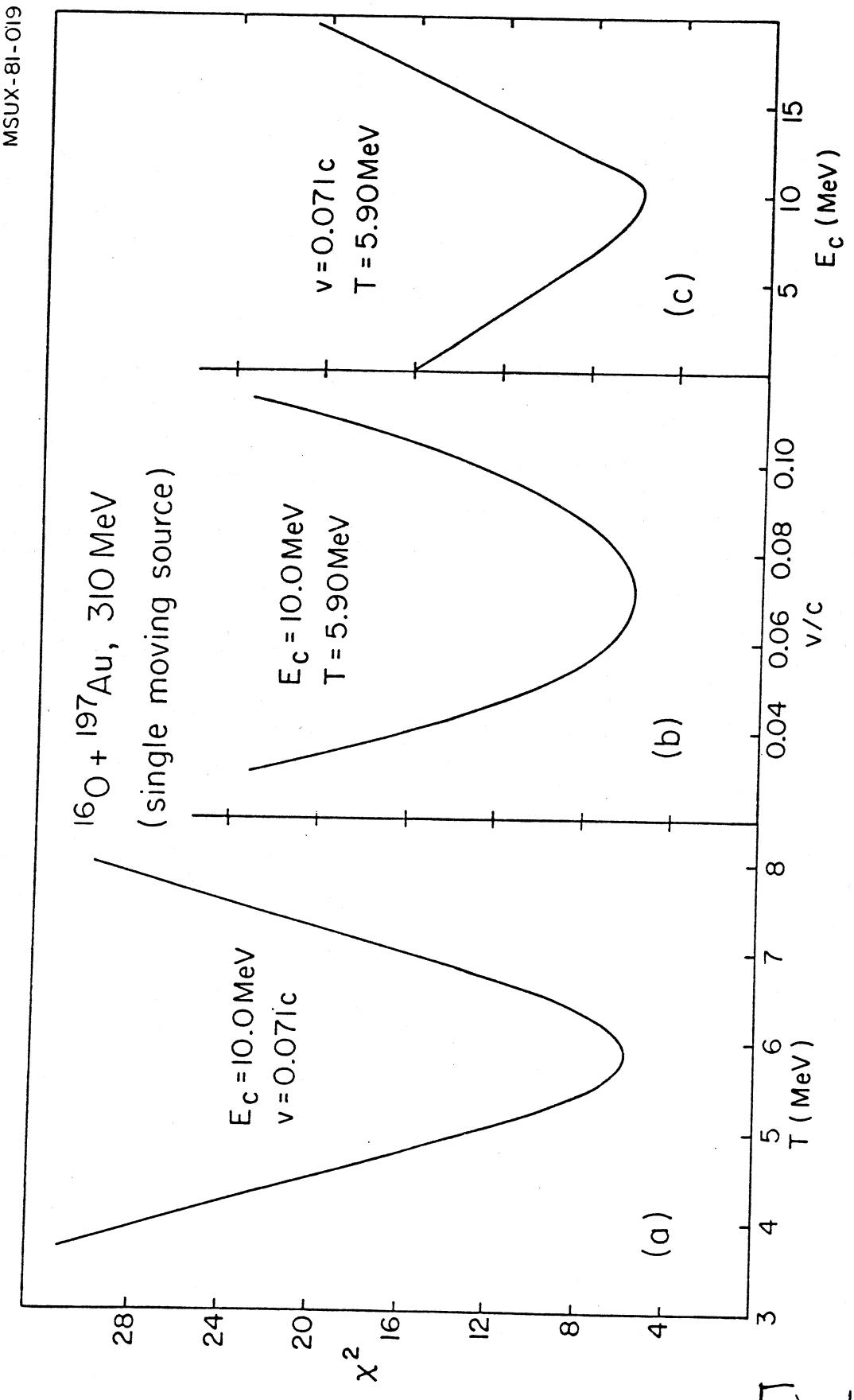
MSUX-81-019
$^{16}O + ^{197}Au$, 310 MeV
(single moving source)
E_c = 10.0 MeV
v = 0.071c
(a)
E_c = 10.0 MeV
T = 5.90 MeV
(b)
v = 0.071c
T = 5.90 MeV
(c)
χ^2
T (MeV)
v/c
E_c (MeV)

Fig. 11

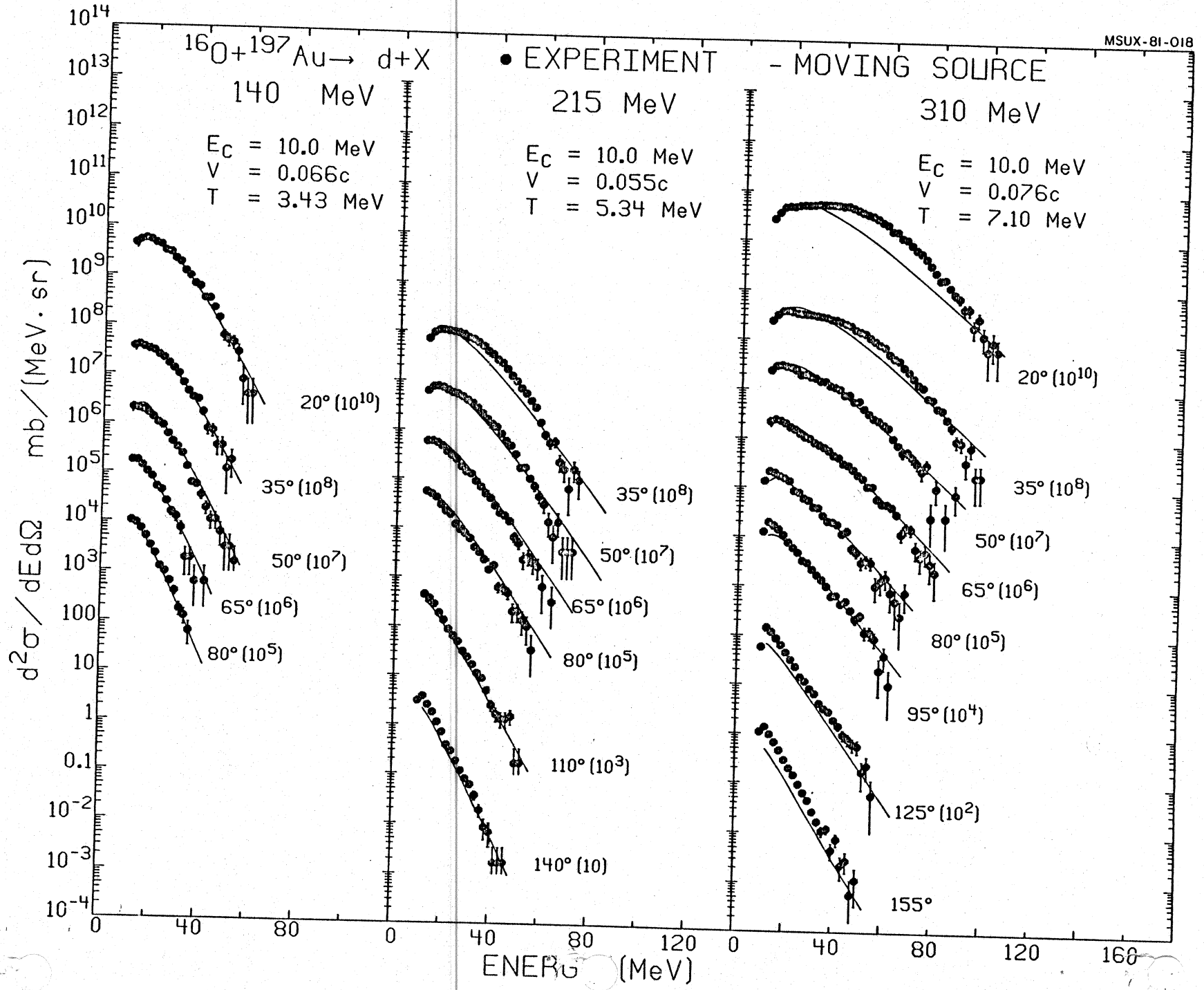
MSUX-81-018
$^{16}O+^{197}Au \rightarrow d+X$
• EXPERIMENT - MOVING SOURCE
140 MeV
E_C = 10.0 MeV
V = 0.066c
T = 3.43 MeV
215 MeV
E_C = 10.0 MeV
V = 0.055c
T = 5.34 MeV
310 MeV
E_C = 10.0 MeV
V = 0.076c
T = 7.10 MeV
$d^2\sigma/dEd\Omega$ mb/(MeV·sr)
ENERGY (MeV)
20° (10^{10})
35° (10^8)
50° (10^7)
65° (10^6)
80° (10^5)
95° (10^4)
110° (10^3)
125° (10^2)
140° (10)
155°

Fig. 12

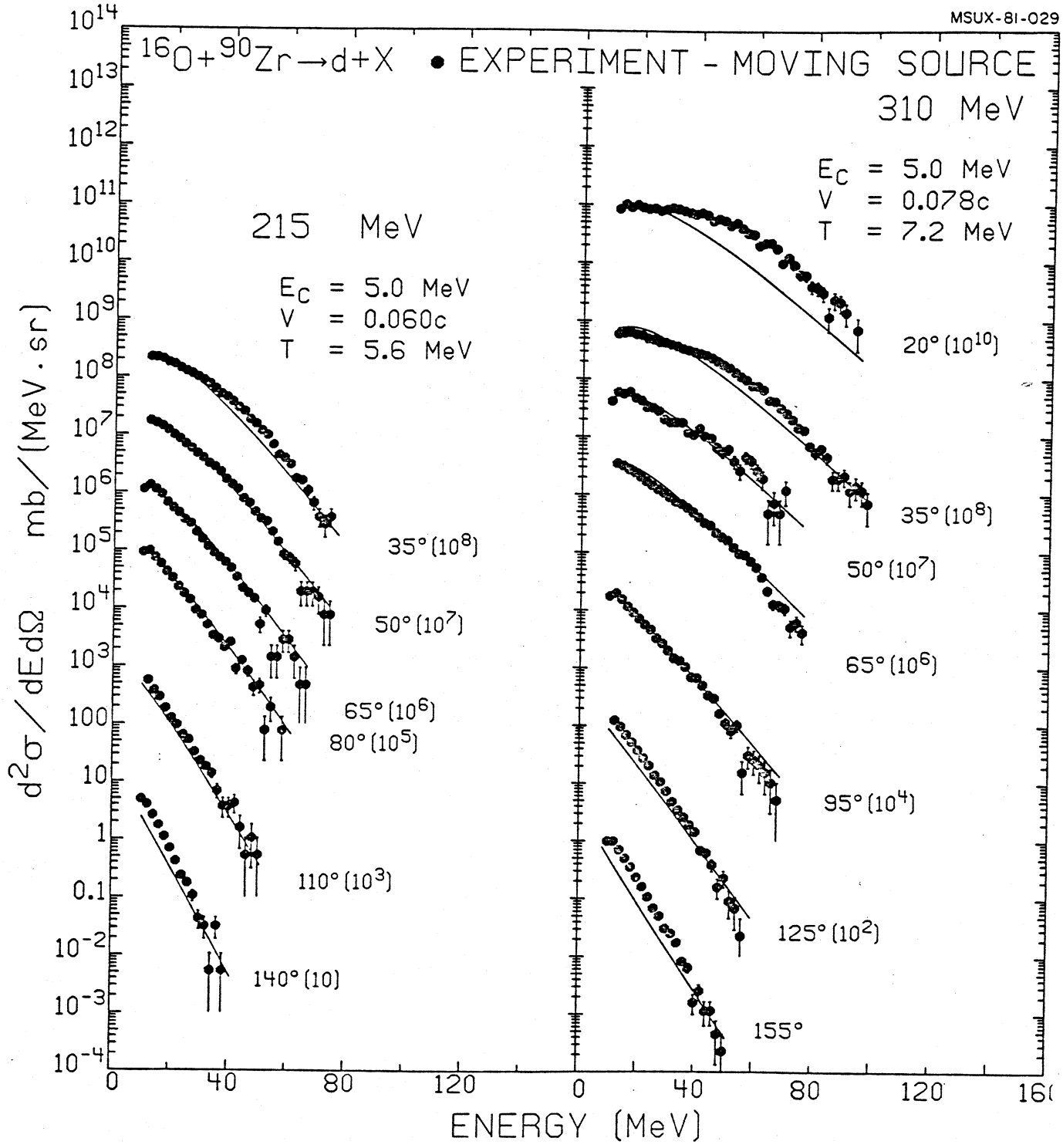
MSUX-81-029
$^{16}O+^{90}Zr \rightarrow d+X$ • EXPERIMENT - MOVING SOURCE
215 MeV
E_C = 5.0 MeV
V = 0.060c
T = 5.6 MeV
35° (10^8)
50° (10^7)
65° (10^6)
80° (10^5)
110° (10^3)
140° (10)
310 MeV
E_C = 5.0 MeV
V = 0.078c
T = 7.2 MeV
20° (10^{10})
35° (10^8)
50° (10^7)
65° (10^6)
95° (10^4)
125° (10^2)
155°
$d^2\sigma / dEd\Omega$ mb/(MeV·sr)
ENERGY (MeV)

Fig. 13

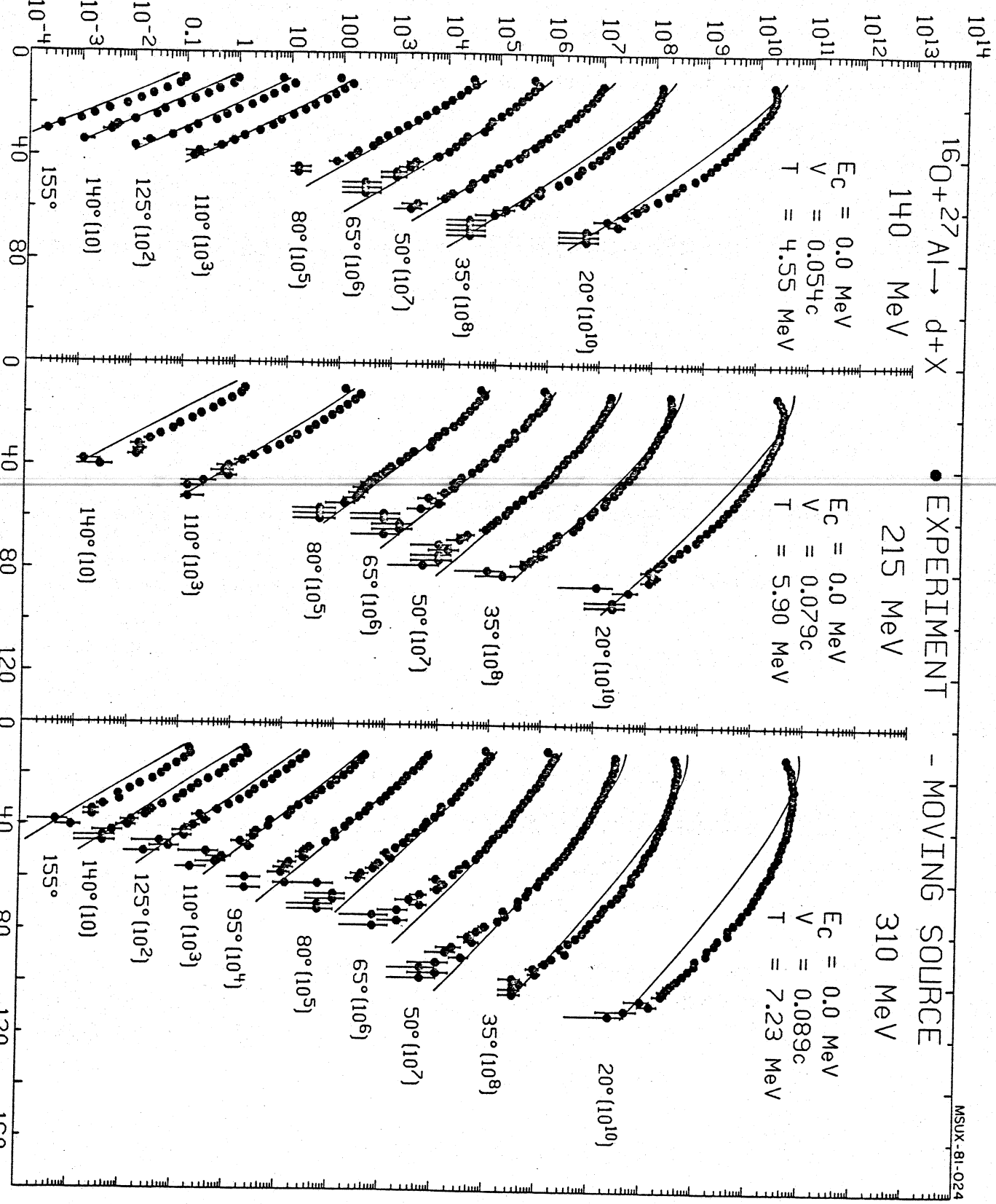
$^{16}O + ^{27}Al \rightarrow d + X$
● EXPERIMENT - MOVING SOURCE
140 MeV
E_c = 0.0 MeV
v = 0.054c
T = 4.55 MeV
215 MeV
E_c = 0.0 MeV
v = 0.079c
T = 5.90 MeV
310 MeV
E_c = 0.0 MeV
v = 0.089c
T = 7.23 MeV
155°
140° (10)
125° (10^2)
110° (10^3)
95° (10^4)
80° (10^5)
65° (10^6)
50° (10^7)
35° (10^8)
20° (10^{10})
$d^2\sigma/dEd\Omega$ mb/(MeV.sr)
ENERGY (MeV)
MSUX-81-024

Fig. 14

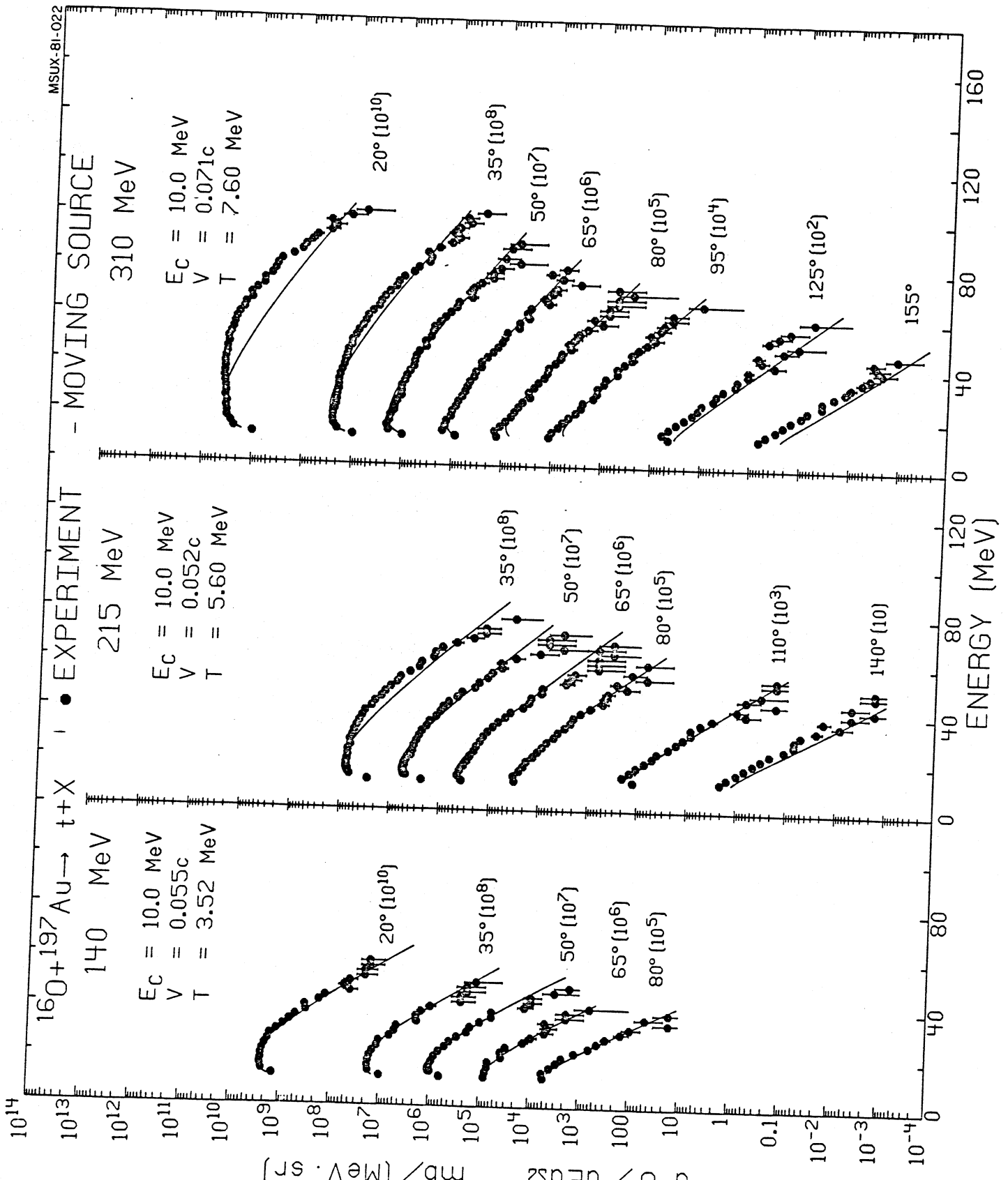
MSUX-81-022
$^{16}O+^{197}Au \rightarrow t+X$ ● EXPERIMENT - MOVING SOURCE
140 MeV
E_c = 10.0 MeV
V = 0.055c
T = 3.52 MeV
215 MeV
E_c = 10.0 MeV
V = 0.052c
T = 5.60 MeV
310 MeV
E_c = 10.0 MeV
V = 0.071c
T = 7.60 MeV
20° (10^{10})
35° (10^8)
50° (10^7)
65° (10^6)
80° (10^5)
95° (10^4)
110° (10^3)
125° (10^2)
140° (10)
155°
$d^2\sigma/dE d\Omega$ mb/(MeV · sr)
ENERGY (MeV)

Fig. 15

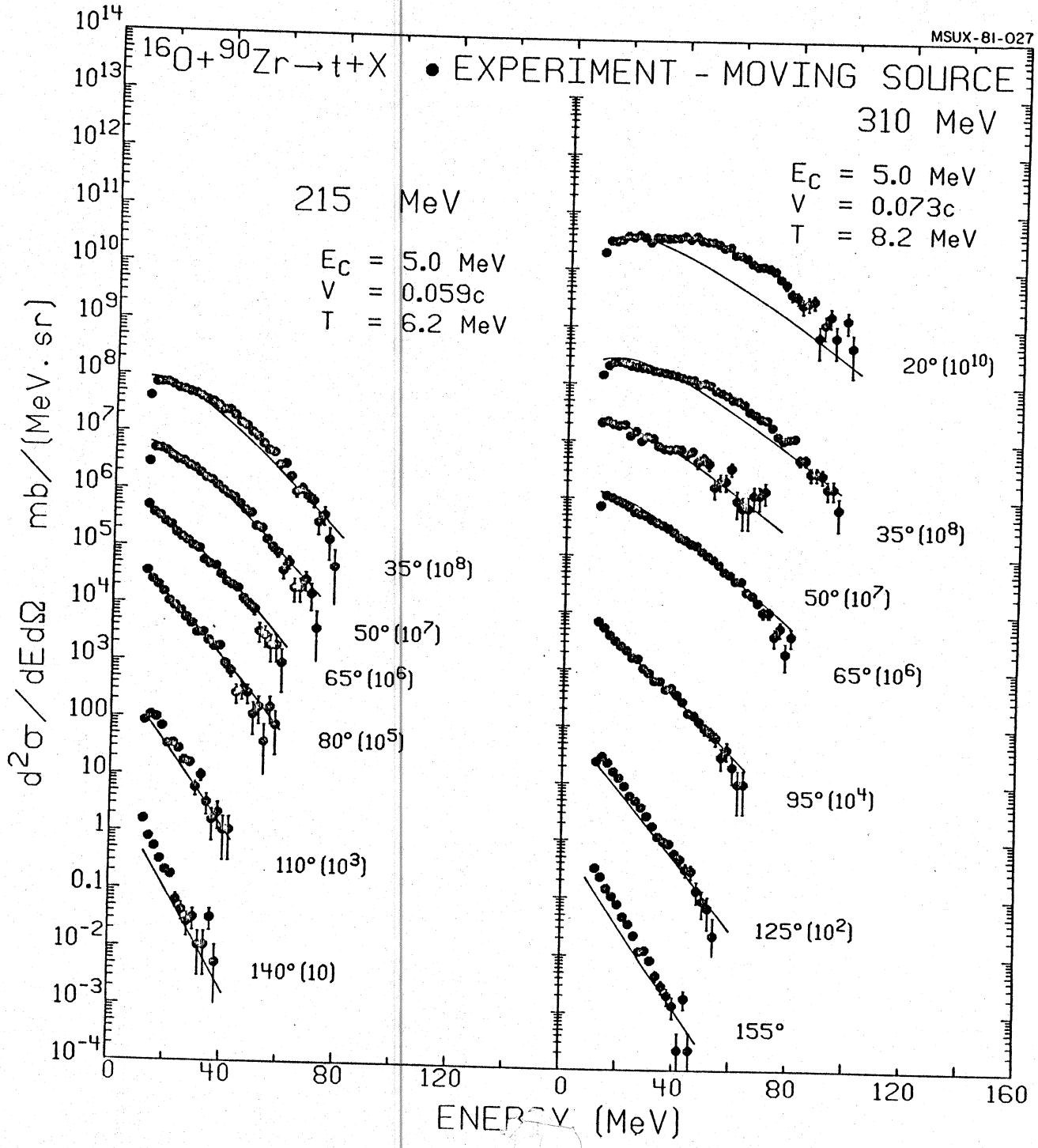
MSUX-81-027
$^{16}O+^{90}Zr \rightarrow t+X$
● EXPERIMENT - MOVING SOURCE
215 MeV
E_C = 5.0 MeV
V = 0.059c
T = 6.2 MeV
310 MeV
E_C = 5.0 MeV
V = 0.073c
T = 8.2 MeV
$d^2\sigma/dEd\Omega$ mb/(MeV·sr)
ENERGY (MeV)
20° (10^{10})
35° (10^8)
50° (10^7)
65° (10^6)
80° (10^5)
95° (10^4)
110° (10^3)
125° (10^2)
140° (10)
155°

9) Fig. 6

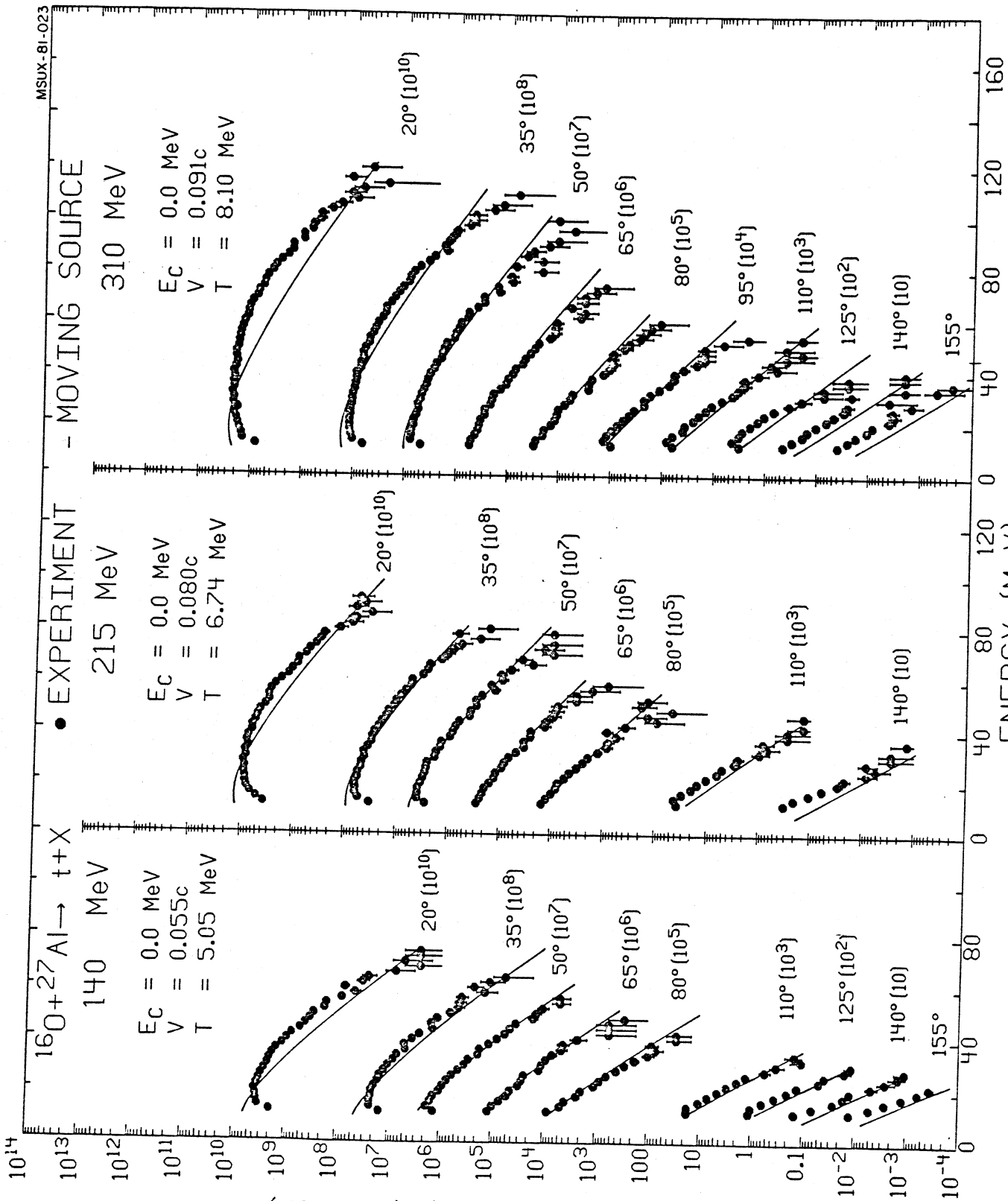
MSUX-81-023
$^{16}O+^{27}Al \rightarrow t+X$
140 MeV
E_c = 0.0 MeV
V = 0.055c
T = 5.05 MeV
● EXPERIMENT
215 MeV
E_c = 0.0 MeV
V = 0.080c
T = 6.74 MeV
- MOVING SOURCE
310 MeV
E_c = 0.0 MeV
V = 0.091c
T = 8.10 MeV
20° (10^{10})
35° (10^8)
50° (10^7)
65° (10^6)
80° (10^5)
95° (10^4)
110° (10^3)
125° (10^2)
140° (10)
155°
$d^2\sigma/dE d\Omega$ mb/(MeV. sr)
ENERGY (MeV)

Fig. 17

MSUX-81-023

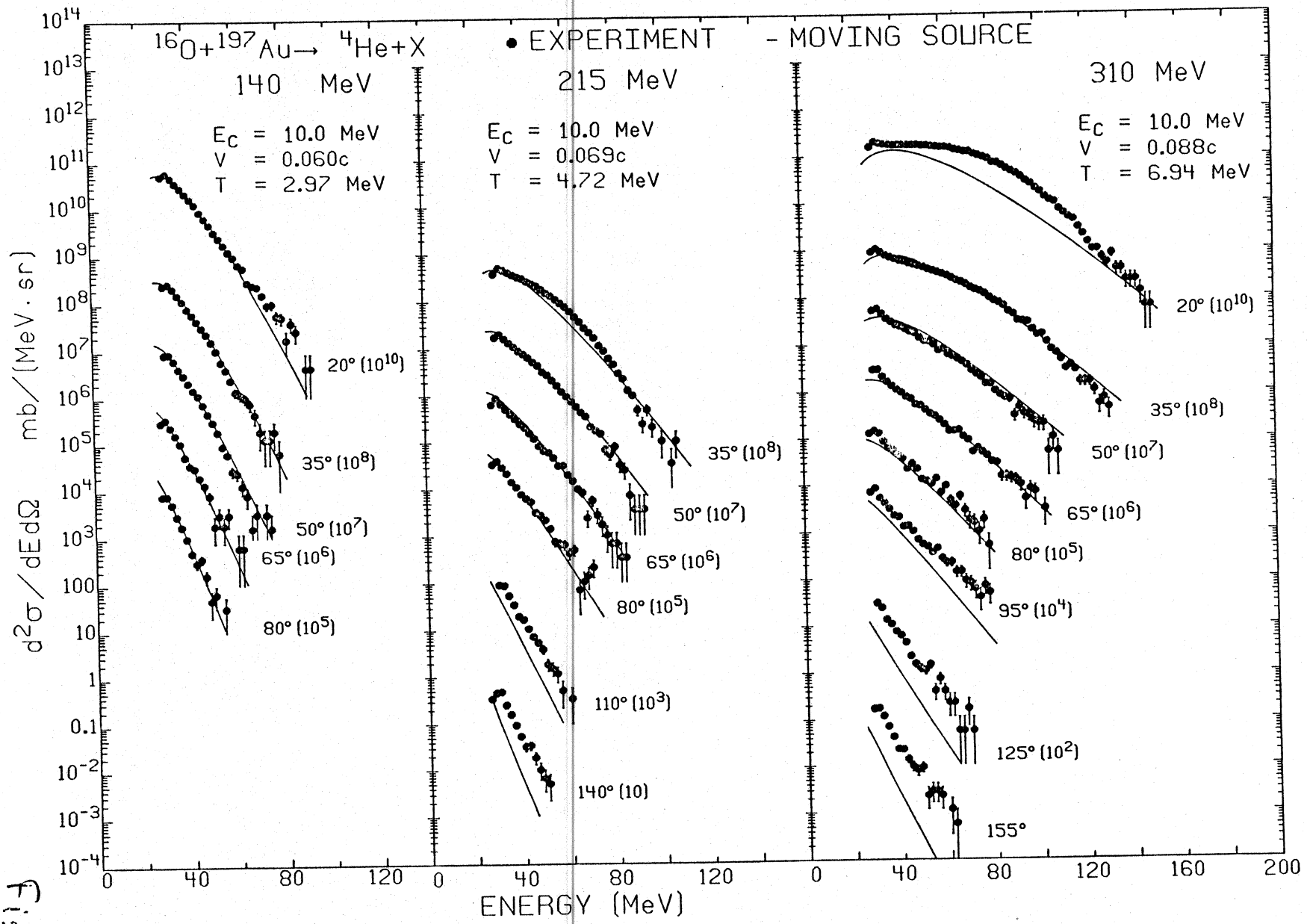

Fig. 18

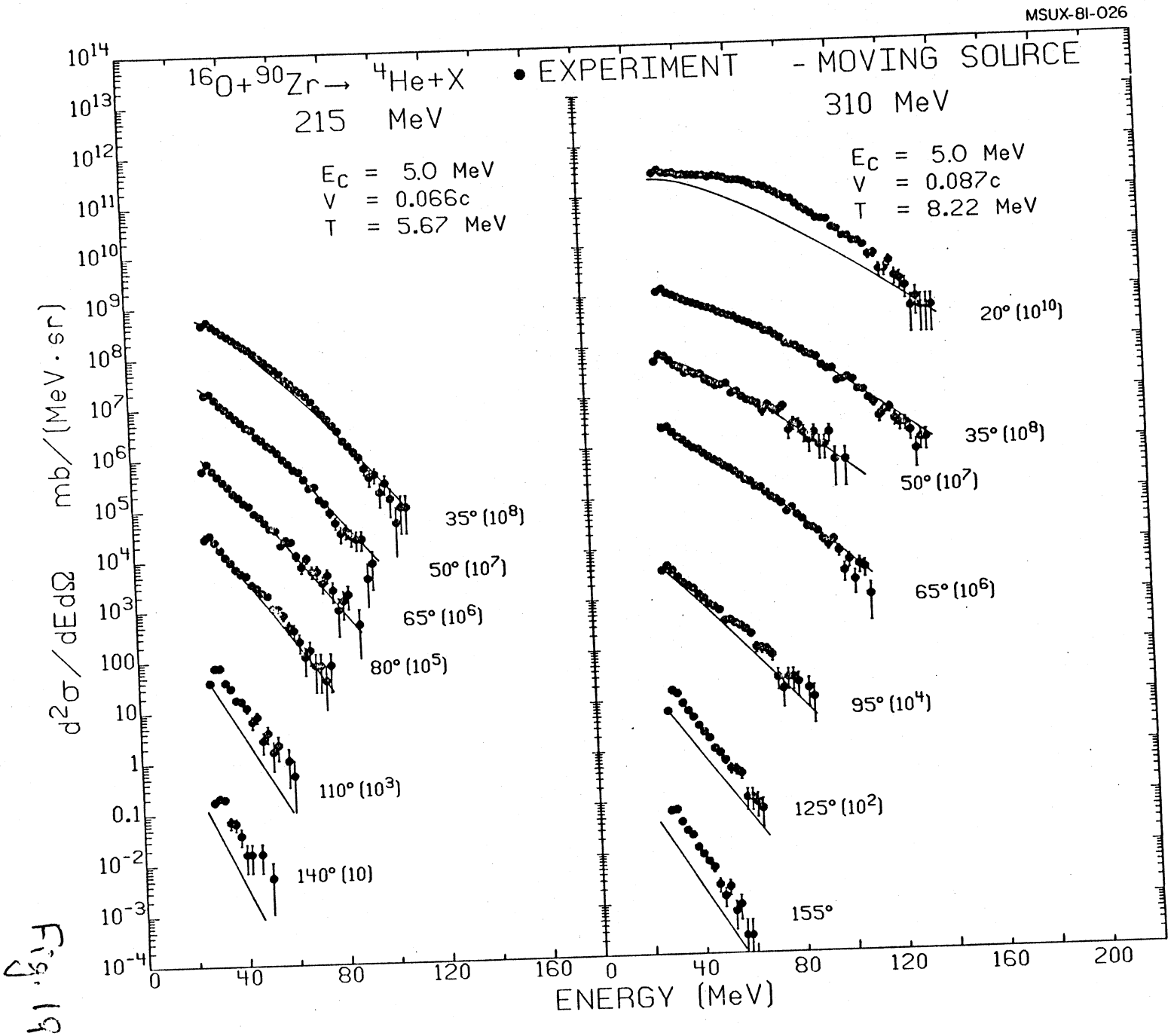
MSUX-81-026
$^{16}O+^{90}Zr \rightarrow {}^{4}He+X$
• EXPERIMENT - MOVING SOURCE
215 MeV
E_C = 5.0 MeV
V = 0.066c
T = 5.67 MeV
310 MeV
E_C = 5.0 MeV
V = 0.087c
T = 8.22 MeV
$d^2\sigma/dEd\Omega$ mb/(MeV·sr)
ENERGY (MeV)
35° (10^8)
50° (10^7)
65° (10^6)
80° (10^5)
110° (10^3)
140° (10)
20° (10^{10})
35° (10^8)
50° (10^7)
65° (10^6)
95° (10^4)
125° (10^2)
155°

Fig. 5.1

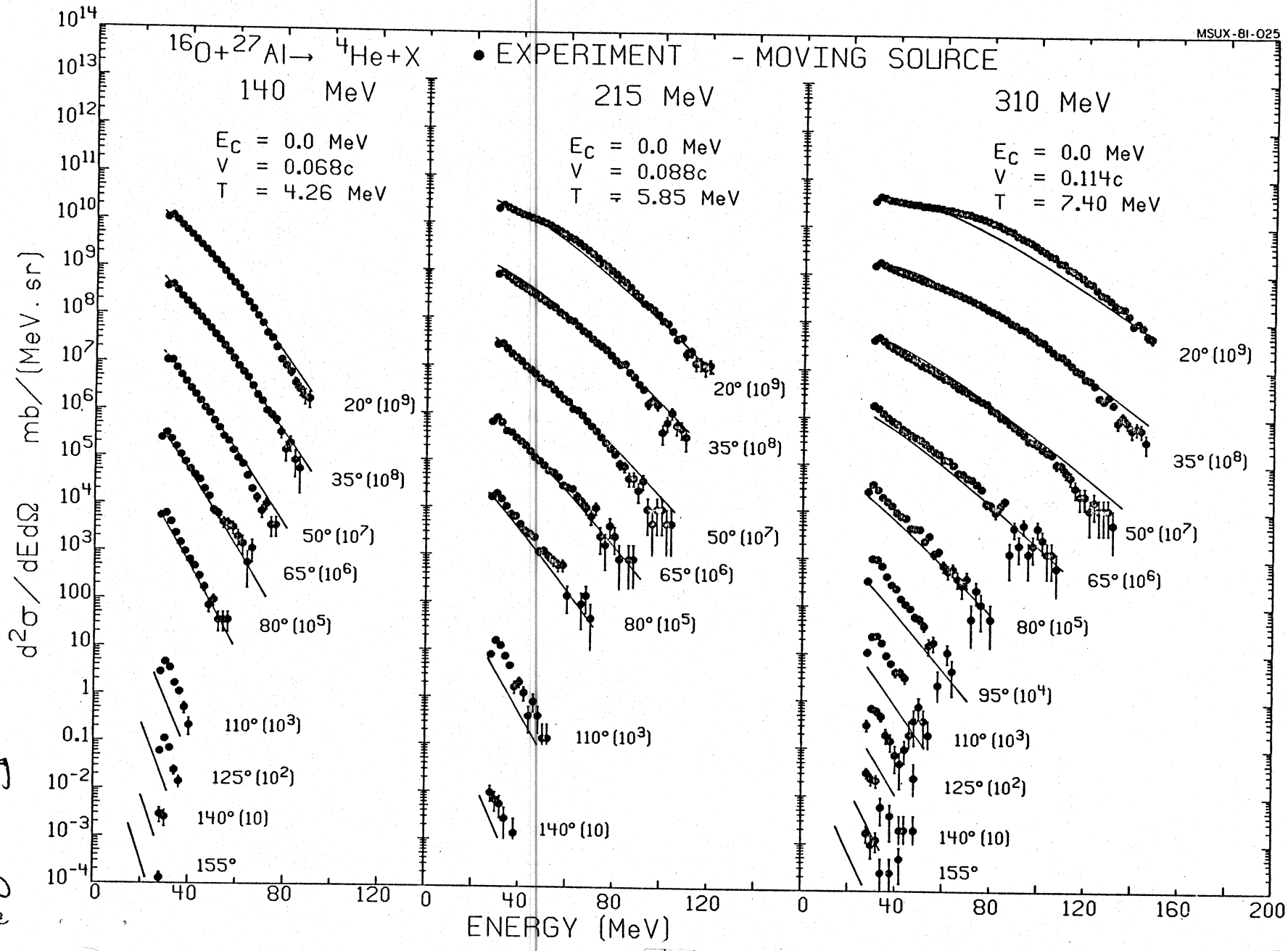
MSUX-81-025
$^{16}O+^{27}Al \rightarrow {}^{4}He+X$ • EXPERIMENT - MOVING SOURCE
140 MeV
E_C = 0.0 MeV
V = 0.068c
T = 4.26 MeV
215 MeV
E_C = 0.0 MeV
V = 0.088c
T = 5.85 MeV
310 MeV
E_C = 0.0 MeV
V = 0.114c
T = 7.40 MeV
20° (10^9)
35° (10^8)
50° (10^7)
65° (10^6)
80° (10^5)
95° (10^4)
110° (10^3)
125° (10^2)
140° (10)
155°
$d^2\sigma/dEd\Omega$ mb/(MeV.sr)
ENERGY (MeV)

Fig. 20

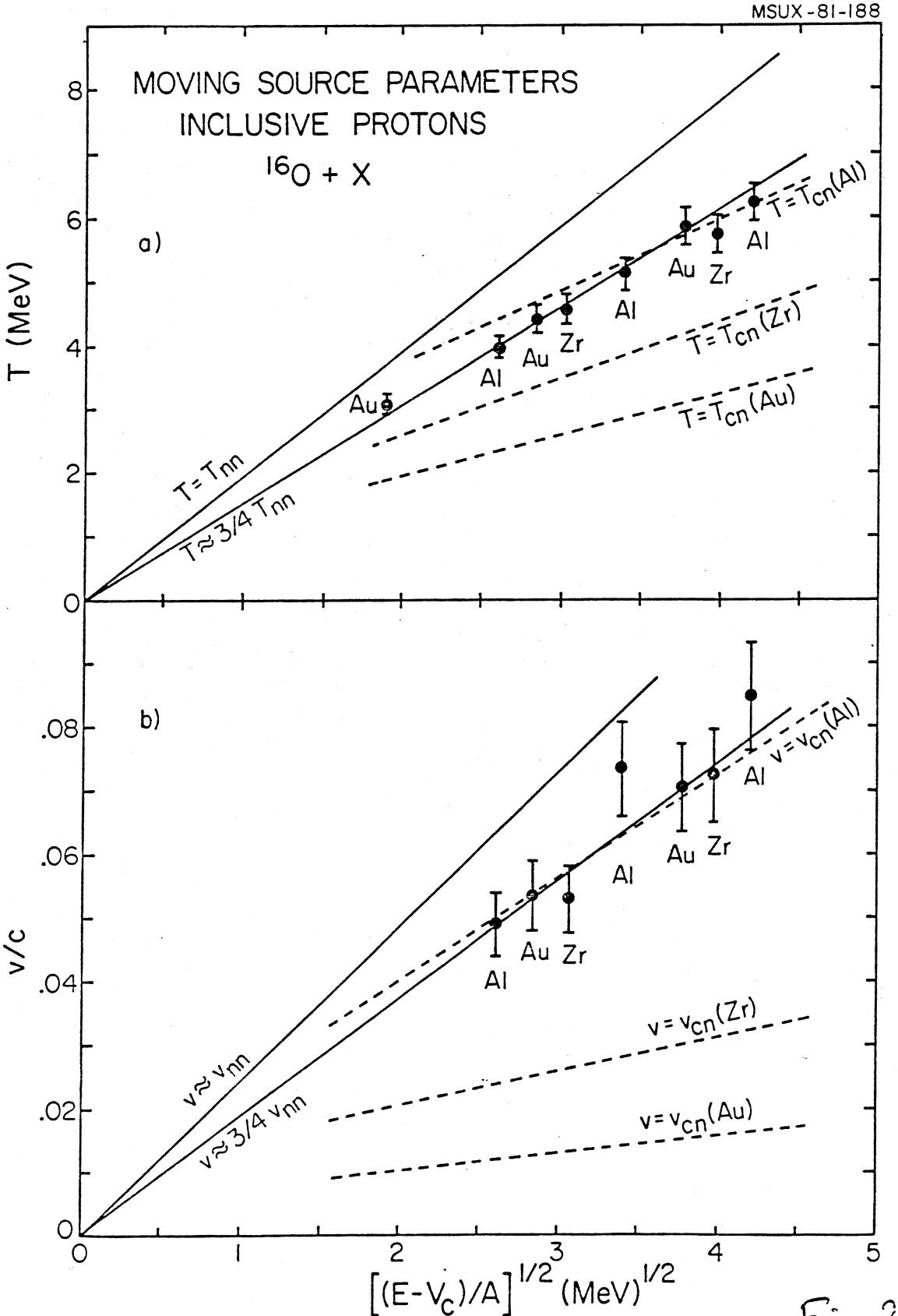
MOVING SOURCE PARAMETERS
INCLUSIVE PROTONS
16O + X
a)
b)
T (MeV)
v/c
T=Tnn
T≈3/4 Tnn
T=Tcn(Al)
T=Tcn(Zr)
T=Tcn(Au)
v≈vnn
v≈3/4 vnn
v=vcn(Al)
v=vcn(Zr)
v=vcn(Au)
Al
Au
Zr
[(E-Vc)/A]1/2 (MeV)1/2

Fig. 21

MSUX-81-074

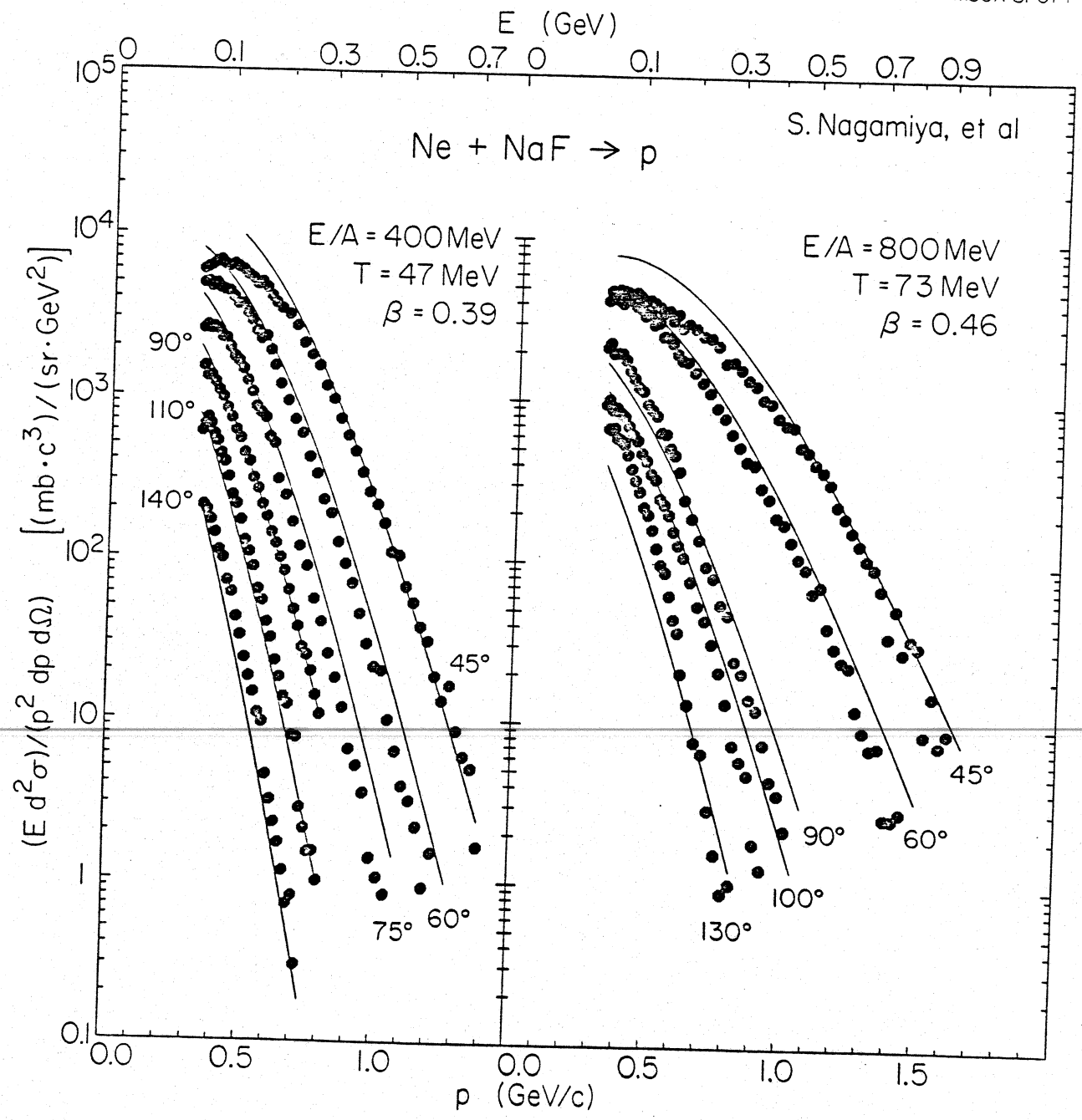

Fig. 22

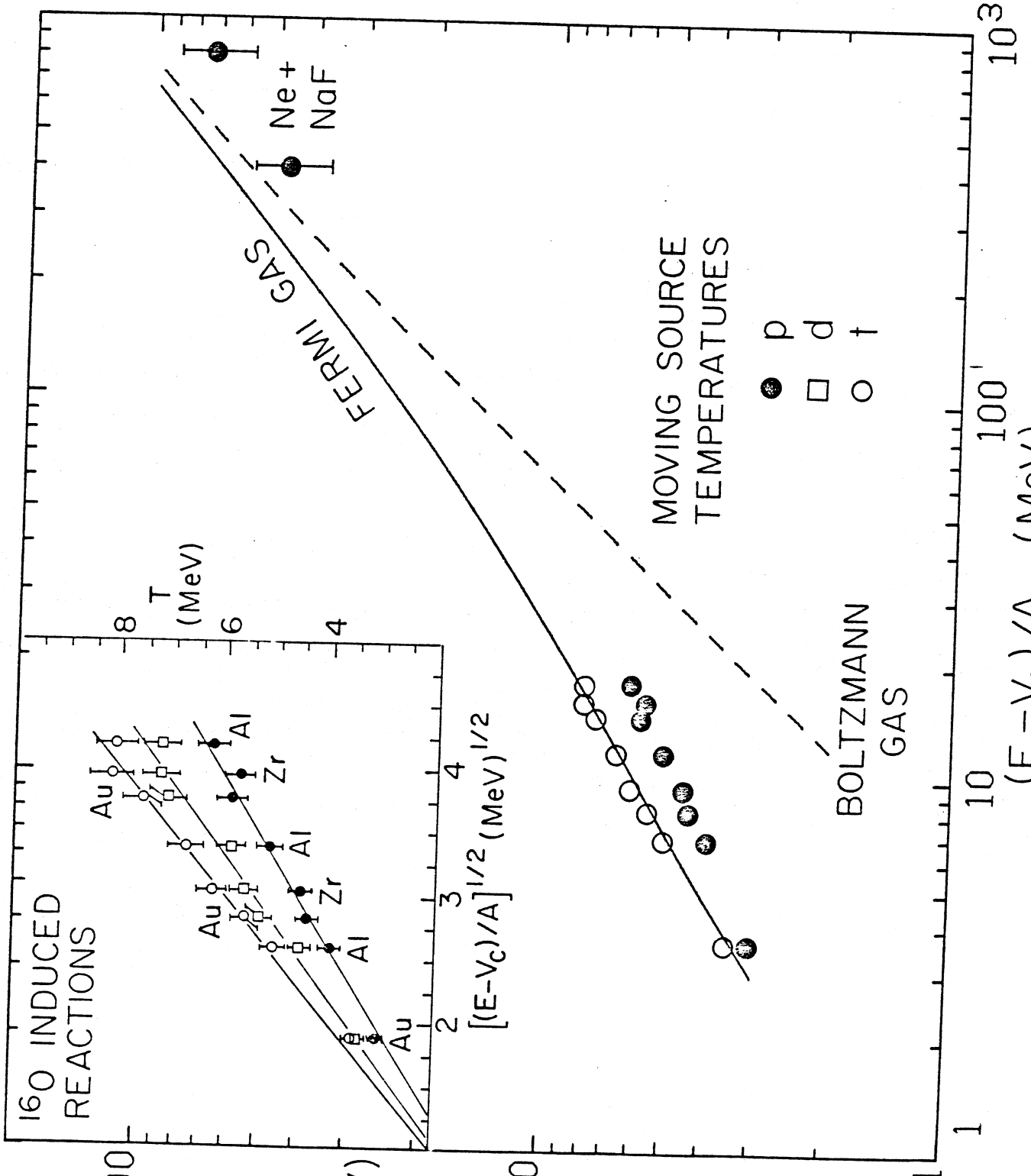
^{16}O INDUCED REACTIONS
Au
Au
Al
Zr
Al
Zr
Al
Au
T (MeV)
100
10
1
$[(E-V_C)/A]^{1/2}$ (MeV)$^{1/2}$
2
3
4
T (MeV)
8
6
4
FERMI GAS
Ne+ NaF
MOVING SOURCE TEMPERATURES
p
d
t
BOLTZMANN GAS
1
10
100
10^3
$(E-V_C)/A$ (MeV)

Fig. 23

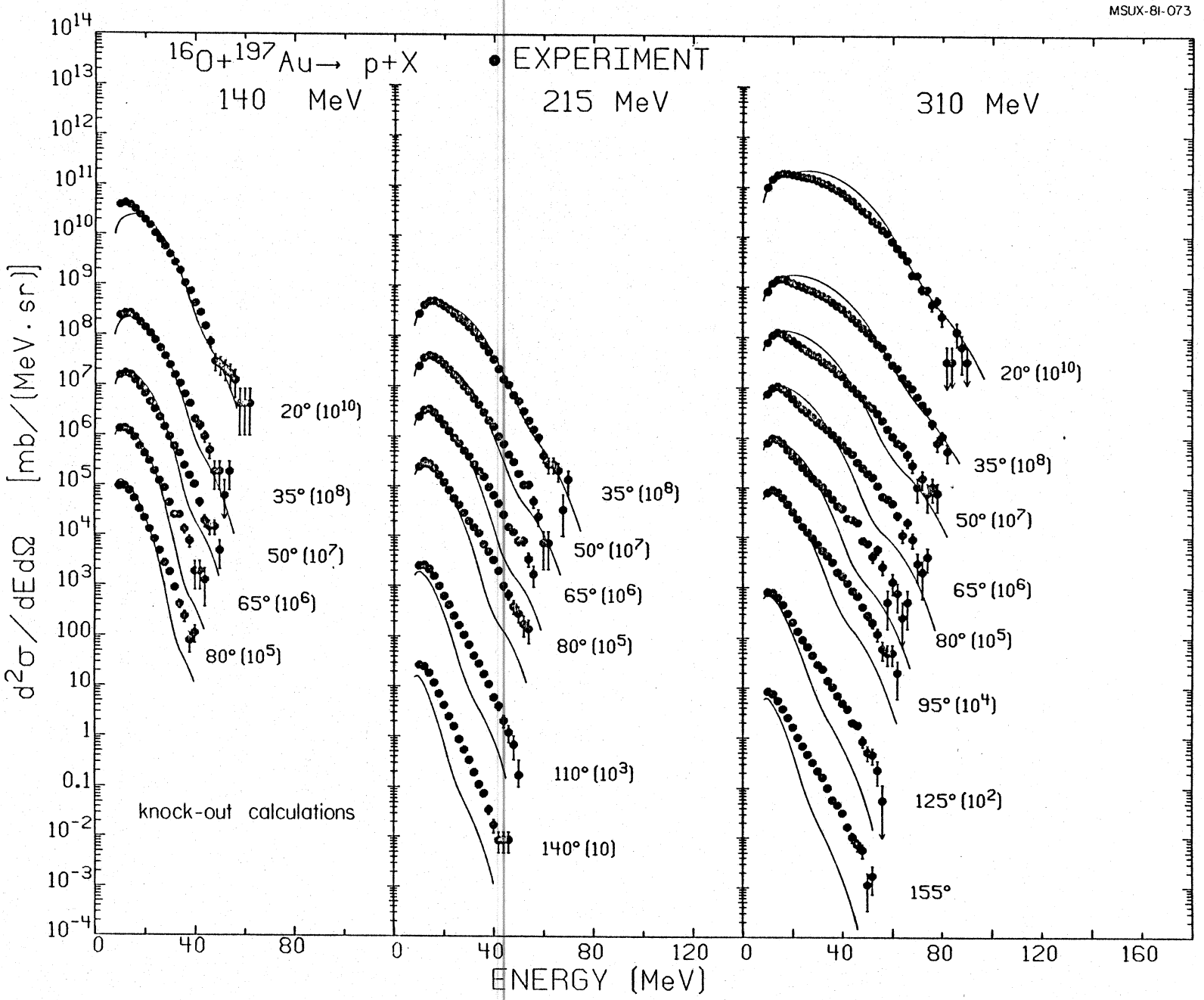
MSUX-81-073
$^{16}O+^{197}Au \rightarrow p+X$
EXPERIMENT
140 MeV
215 MeV
310 MeV
$d^2\sigma/dEd\Omega$ [mb/(MeV·sr)]
20° (10^{10})
35° (10^{8})
50° (10^{7})
65° (10^{6})
80° (10^{5})
95° (10^{4})
110° (10^{3})
125° (10^{2})
140° (10)
155°
knock-out calculations
ENERGY (MeV)

Fig. 24

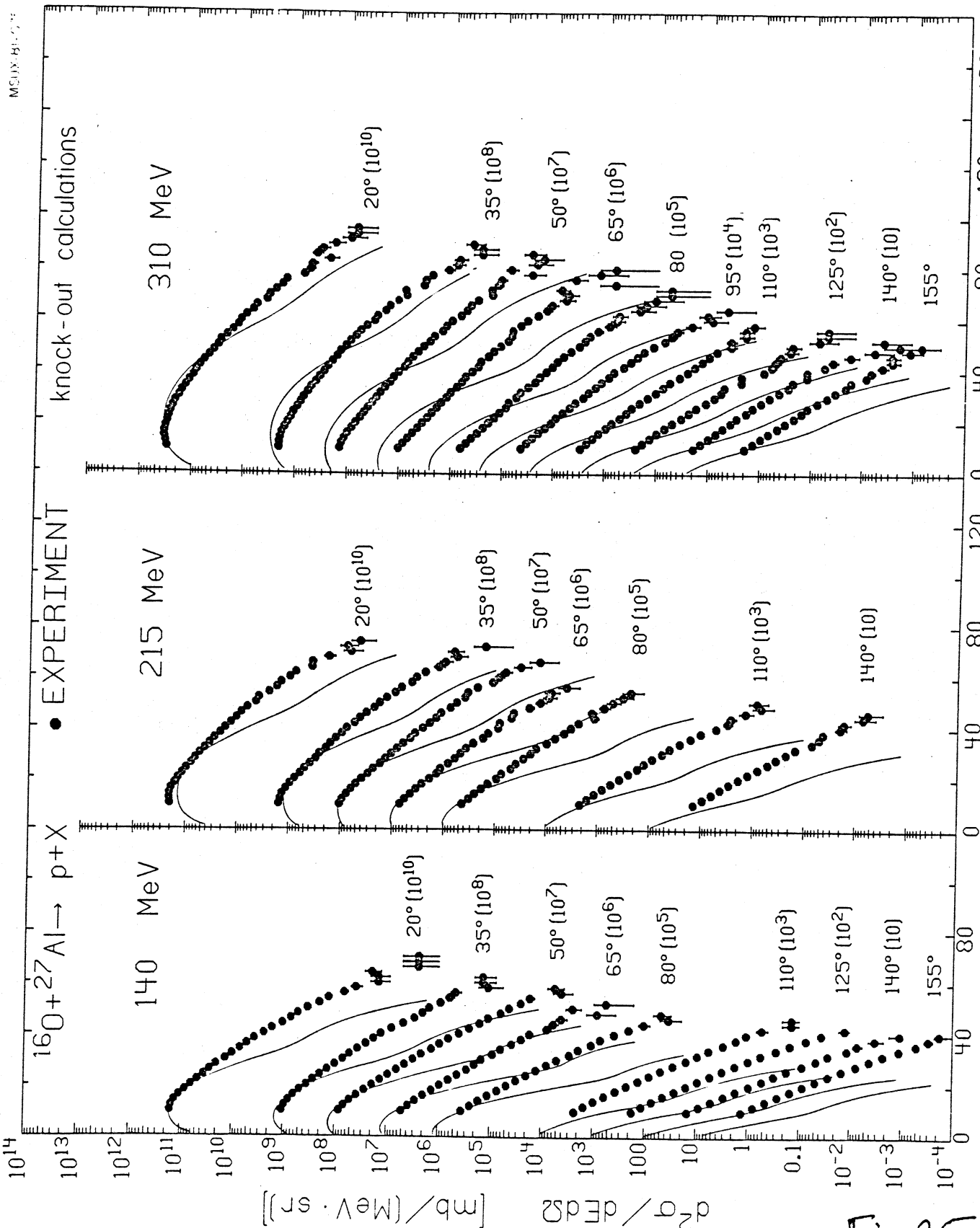
$^{16}O+^{27}Al \rightarrow p+X$
• EXPERIMENT
knock-out calculations
140 MeV
215 MeV
310 MeV
20° (10^10)
35° (10^8)
50° (10^7)
65° (10^6)
80° (10^5)
95° (10^4)
110° (10^3)
125° (10^2)
140° (10)
155°
$d^2\sigma/d\Omega dE$ [mb/(MeV · sr)]
ENERGY (MeV)

Fig. 25

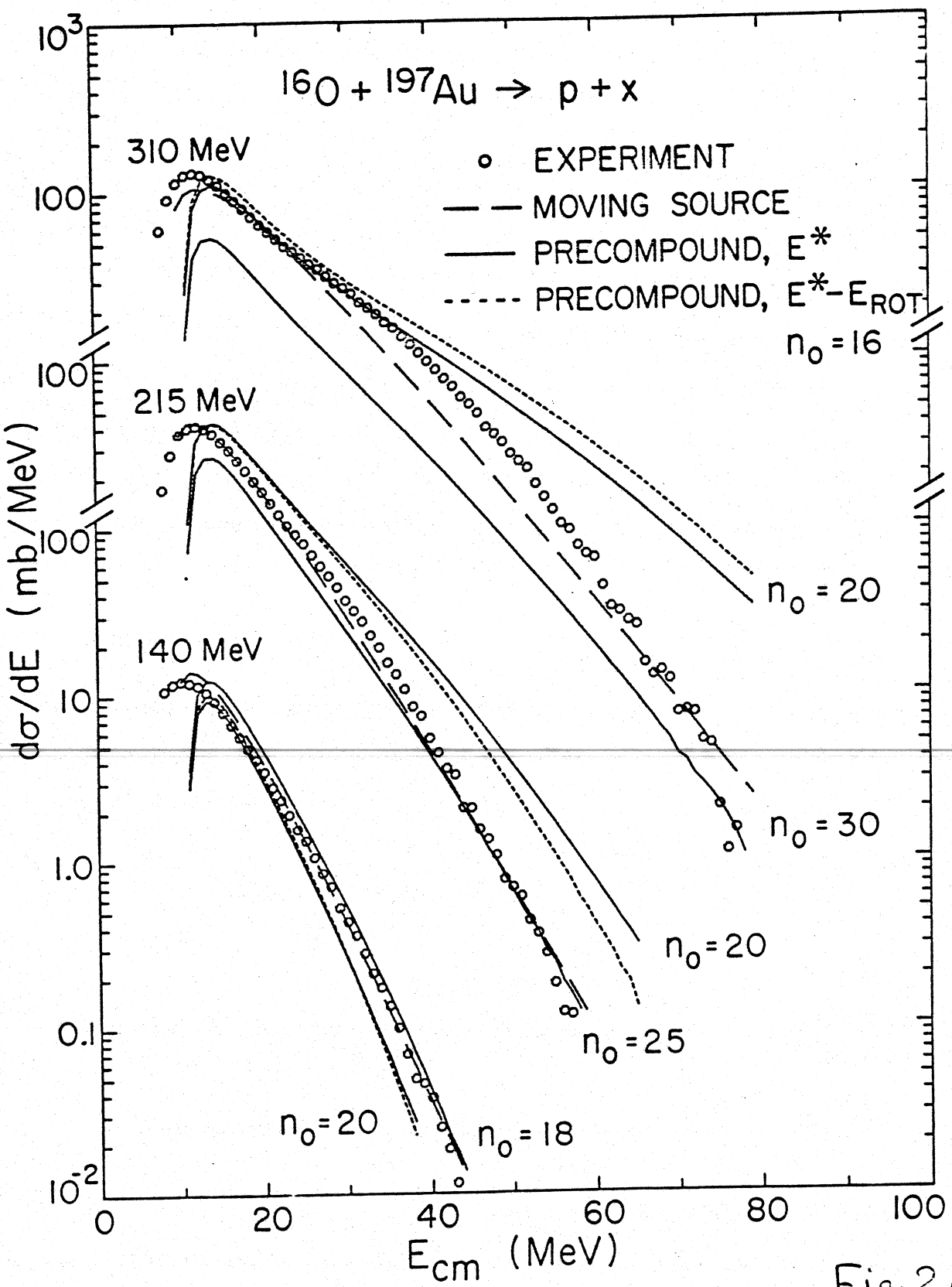
$^{16}O + ^{197}Au \rightarrow p + x$
310 MeV
215 MeV
140 MeV
EXPERIMENT
MOVING SOURCE
PRECOMPOUND, E*
PRECOMPOUND, E*-E_ROT
n_o = 16
n_o = 20
n_o = 30
n_o = 20
n_o = 25
n_o = 20
n_o = 18
dσ/dE (mb/MeV)
E_cm (MeV)
10^3
100
10
1.0
0.1
10^-2
0
20
40
60
80
100

Fig. 26

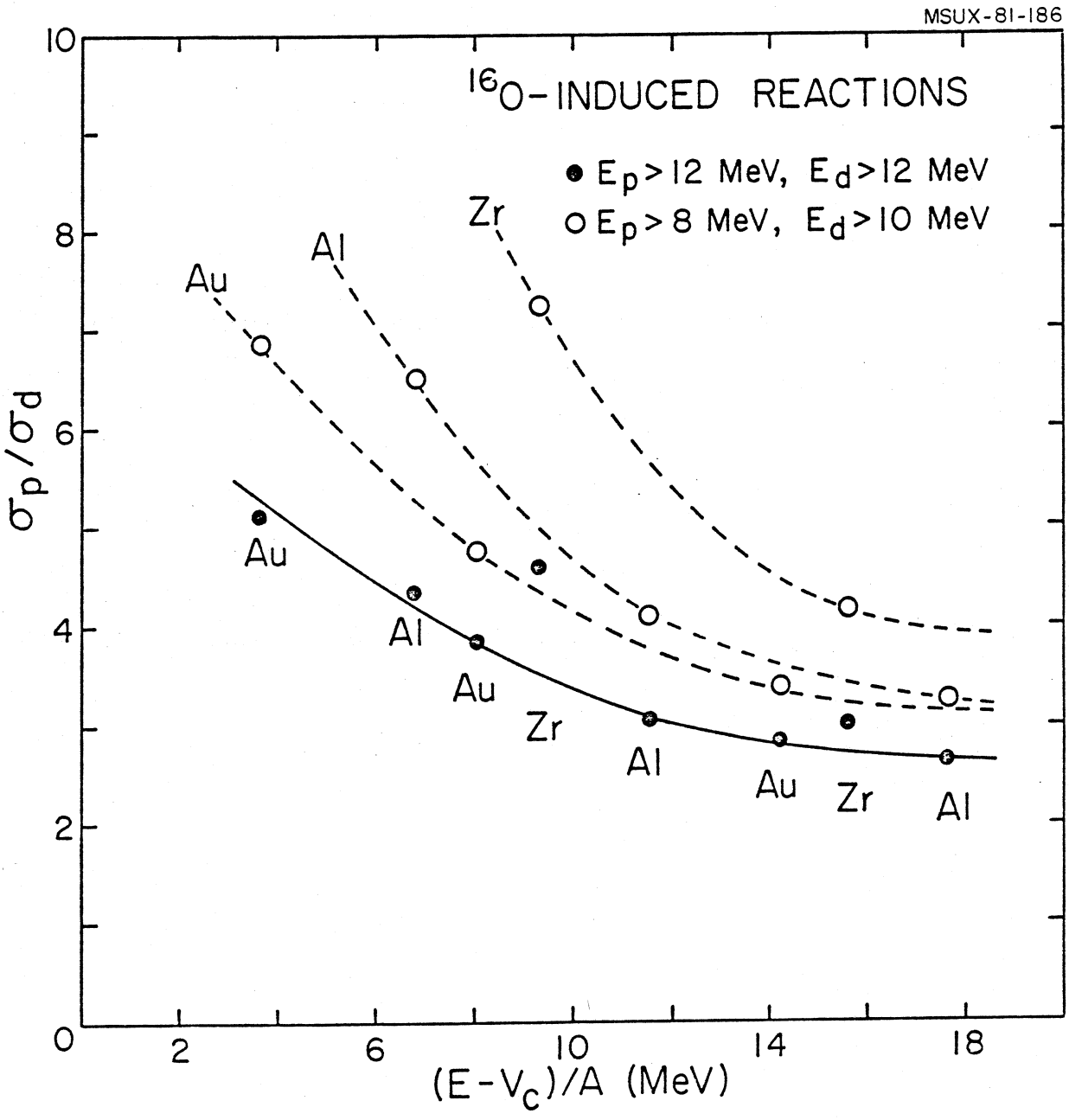
MSUX-81-186
^{16}O-INDUCED REACTIONS
● E_p>12 MeV, E_d>12 MeV
○ E_p>8 MeV, E_d>10 MeV
Zr
Al
Au
Au
Al
Au
Zr
Al
Au
Zr
Al
σ_p/σ_d
(E-V_c)/A (MeV)
0
2
4
6
8
10
2
6
10
14
18

Fig. 27

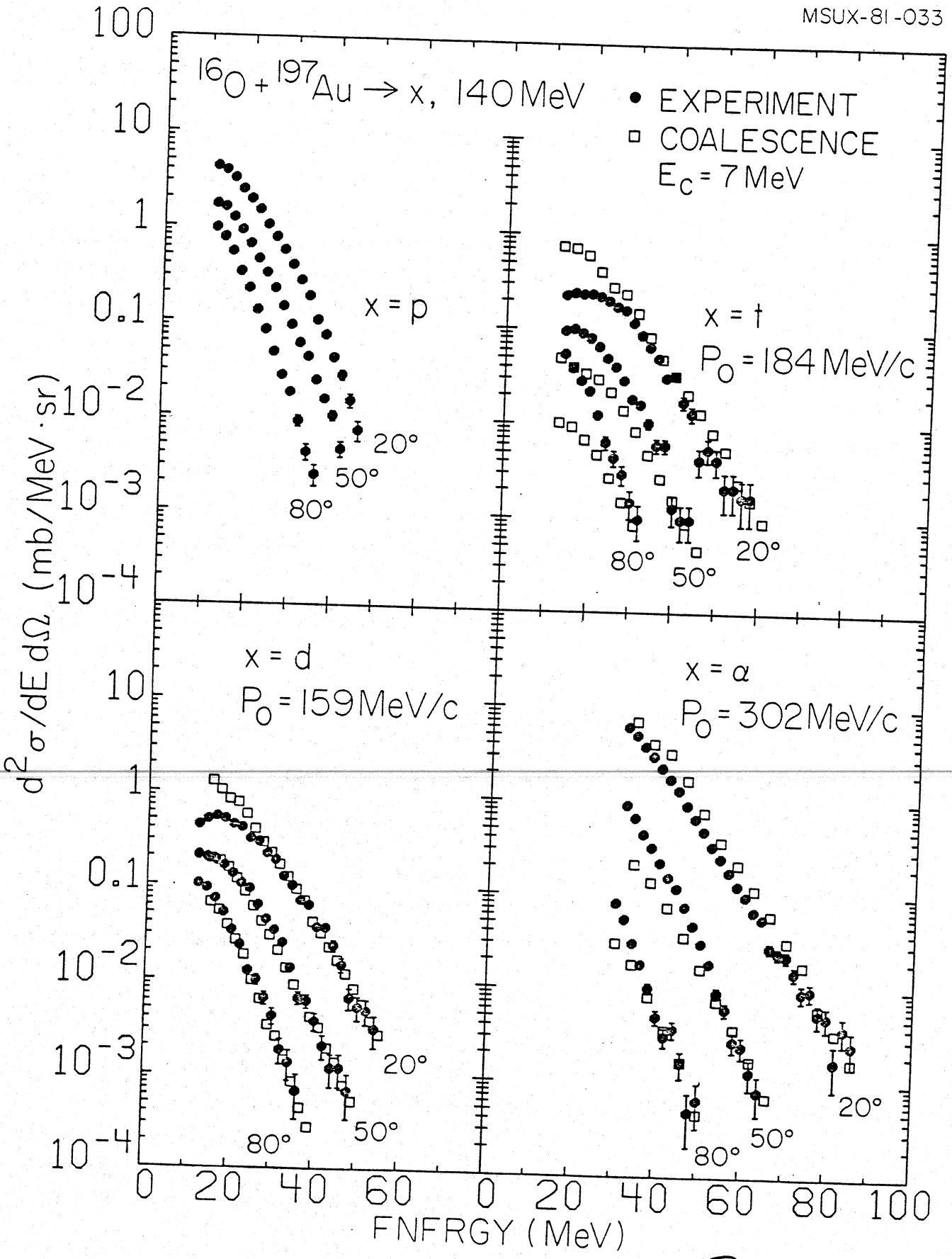
MSUX-81-033
$^{16}O + ^{197}Au \rightarrow x$, 140 MeV
EXPERIMENT
COALESCENCE
$E_c = 7$ MeV
x = p
x = t
$P_0 = 184$ MeV/c
x = d
$P_0 = 159$ MeV/c
x = α
$P_0 = 302$ MeV/c
20°
50°
80°
$d^2\sigma/dE\,d\Omega$ (mb/MeV·sr)
FNFRGY (MeV)

Fig. 28

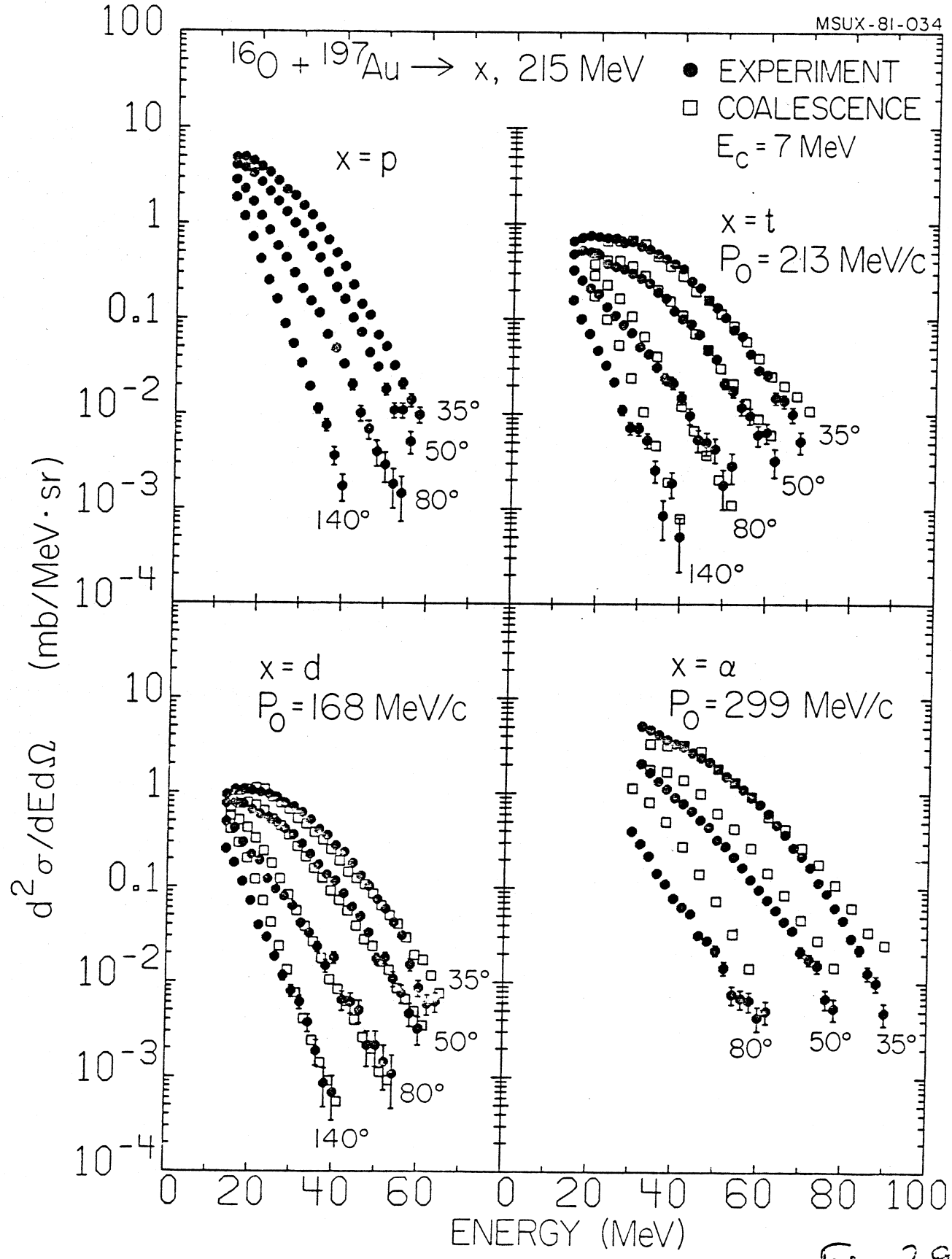
MSUX-81-034
$^{16}O + ^{197}Au \rightarrow x$, 215 MeV
EXPERIMENT
COALESCENCE
E_c = 7 MeV
x = p
x = t
P_0 = 213 MeV/c
x = d
P_0 = 168 MeV/c
x = α
P_0 = 299 MeV/c
35°
50°
80°
140°
$d^2\sigma/dEd\Omega$ (mb/MeV·sr)
ENERGY (MeV)

Fig. 29

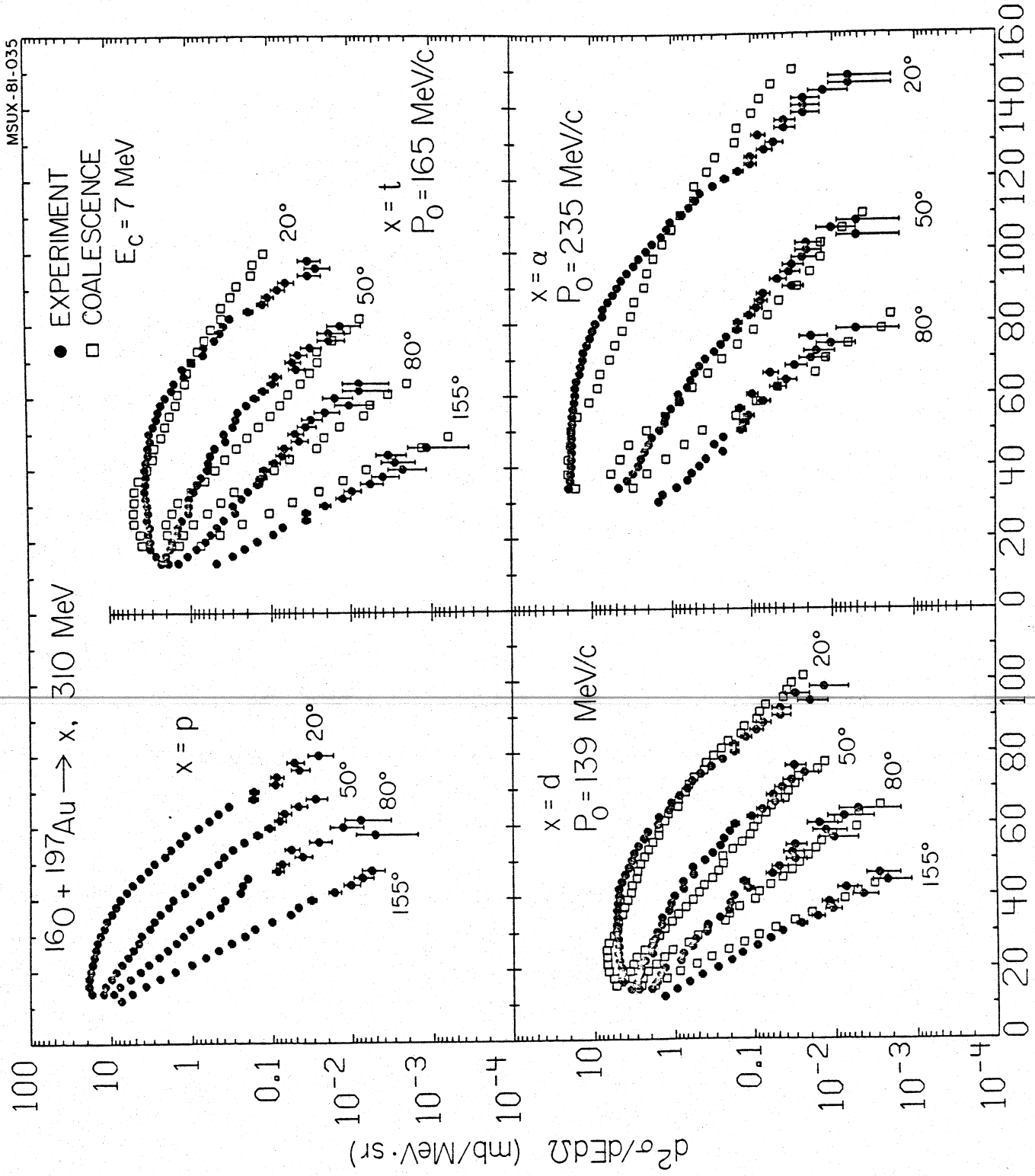
MSUX-81-035
EXPERIMENT
COALESCENCE
E_c = 7 MeV
$^{16}O + ^{197}Au \rightarrow x$, 310 MeV
x = p
x = t
P_0 = 165 MeV/c
x = d
P_0 = 139 MeV/c
x = α
P_0 = 235 MeV/c
20°
50°
80°
155°
$d^2\sigma/dE d\Omega$ (mb/MeV·sr)
ENERGY (MeV)

Fig. 30

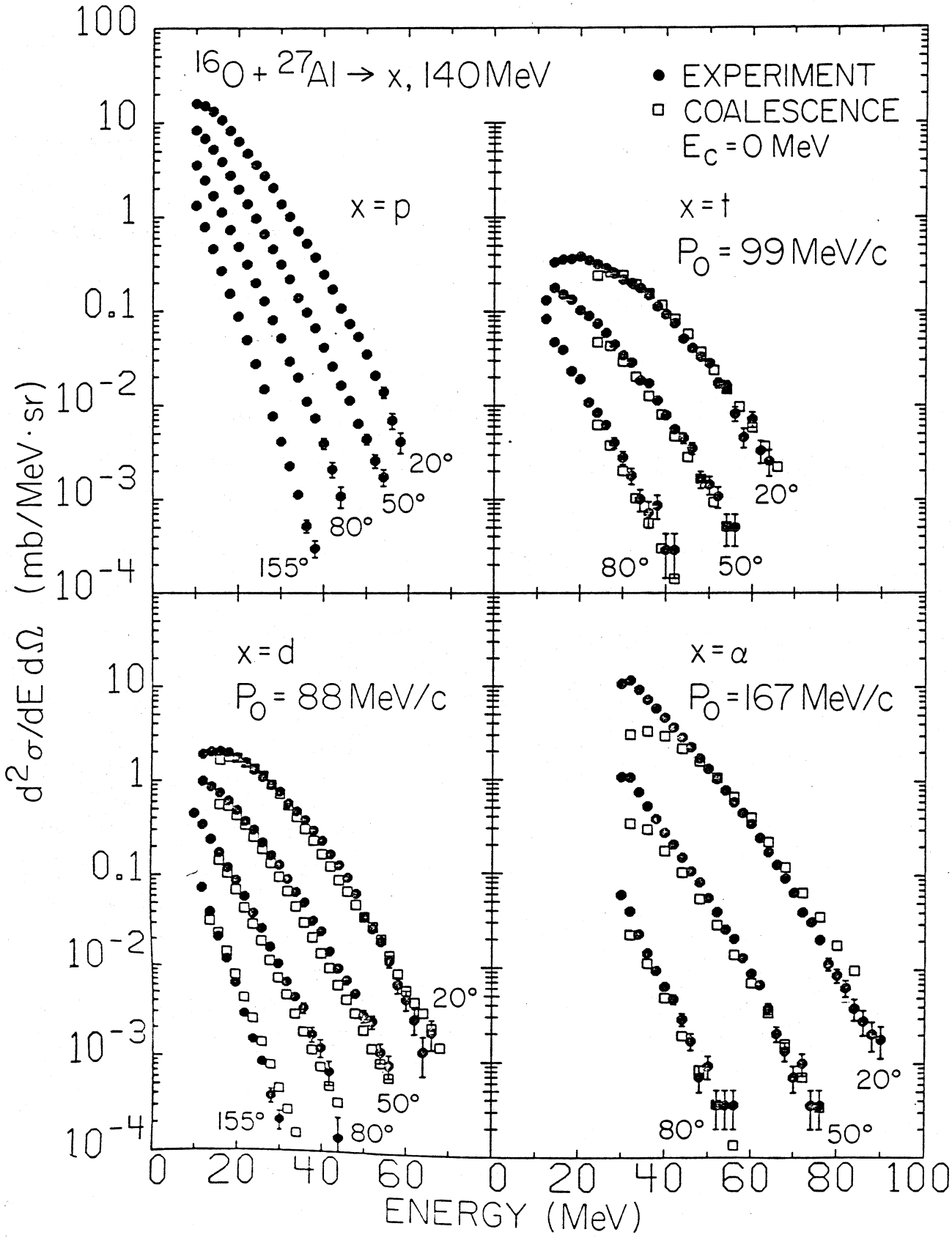
$^{16}O + ^{27}Al \rightarrow x$, 140 MeV
EXPERIMENT
COALESCENCE
E_c = 0 MeV
x = p
x = t
P_0 = 99 MeV/c
x = d
P_0 = 88 MeV/c
x = α
P_0 = 167 MeV/c
20°
50°
80°
155°
$d^2\sigma/dE\,d\Omega$ (mb/MeV·sr)
ENERGY (MeV)

Fig. 31

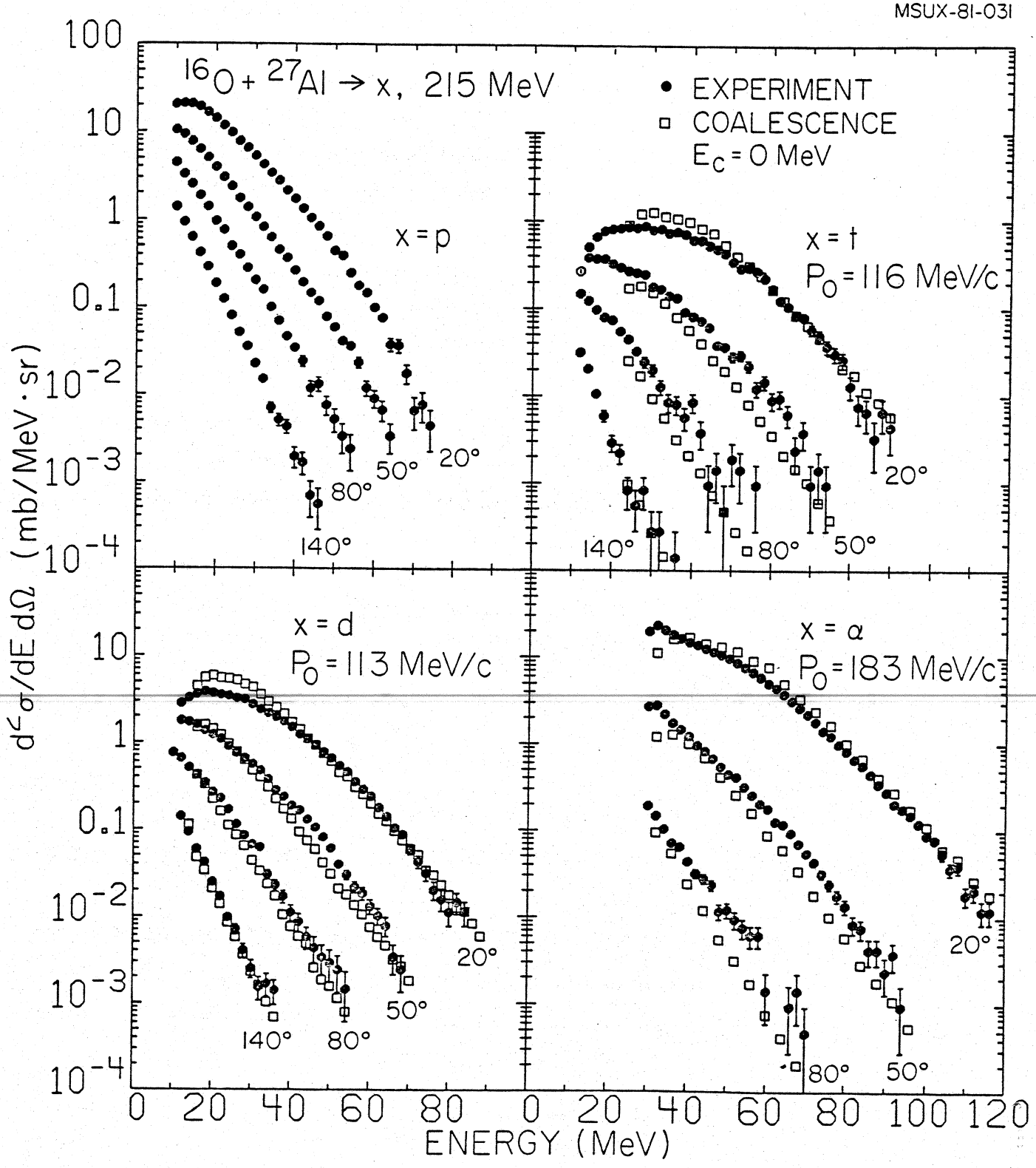
MSUX-81-031
$^{16}O + ^{27}Al \rightarrow x$, 215 MeV
EXPERIMENT
COALESCENCE
E_c = 0 MeV
x = p
x = t
P_0 = 116 MeV/c
x = d
P_0 = 113 MeV/c
x = α
P_0 = 183 MeV/c
20°
50°
80°
140°
$d^2\sigma/dE\,d\Omega$ (mb/MeV·sr)
ENERGY (MeV)

Fig. 32

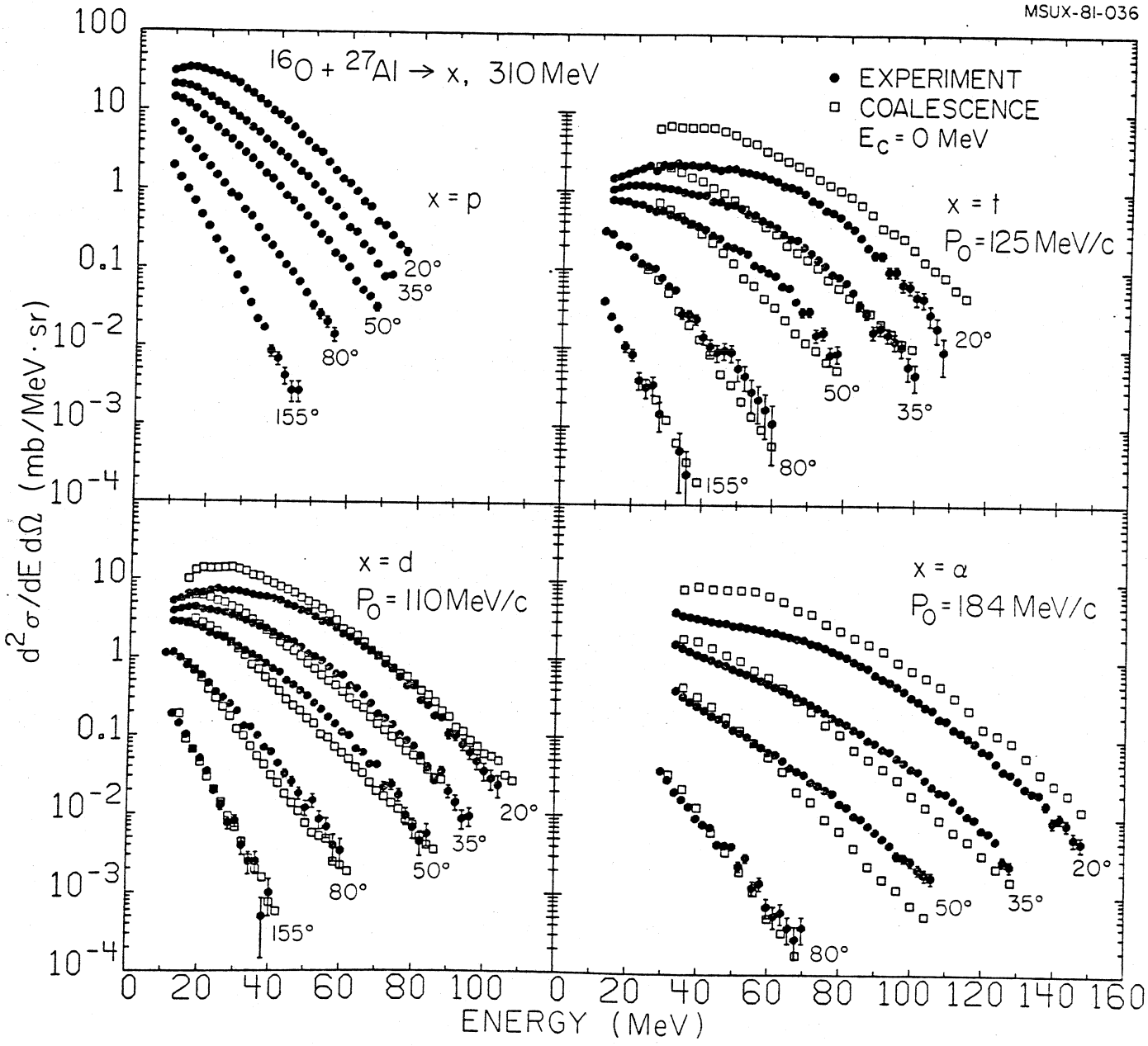
MSUX-81-036
$^{16}O + ^{27}Al \rightarrow x$, 310 MeV
EXPERIMENT
COALESCENCE
E_c = 0 MeV
x = p
x = t
P_0 = 125 MeV/c
x = d
P_0 = 110 MeV/c
x = α
P_0 = 184 MeV/c
20°
35°
50°
80°
155°
$d^2\sigma/dE\,d\Omega$ (mb/MeV·sr)
ENERGY (MeV)

Fig. 33

MSUX-81-064

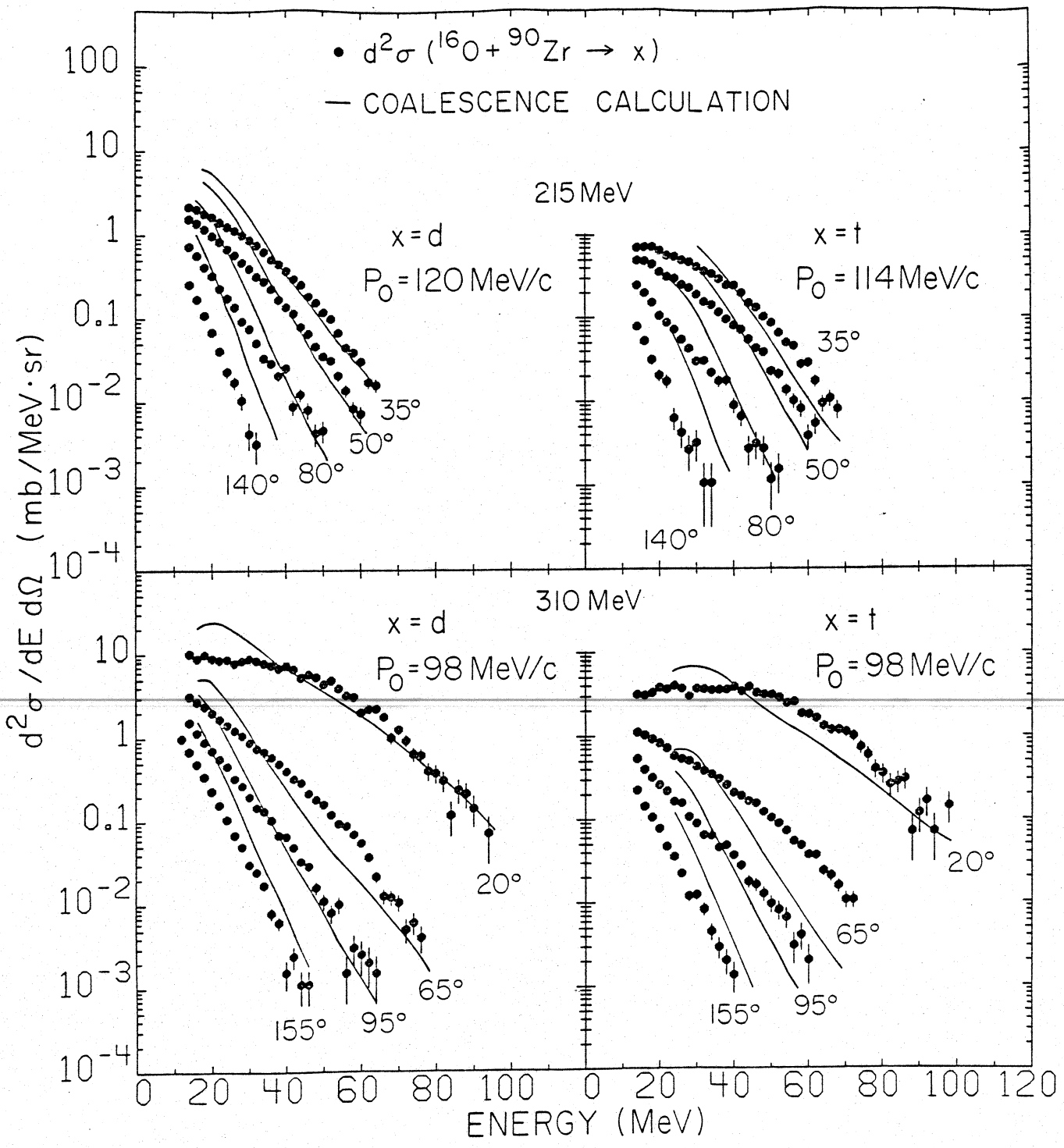

Fig. 34

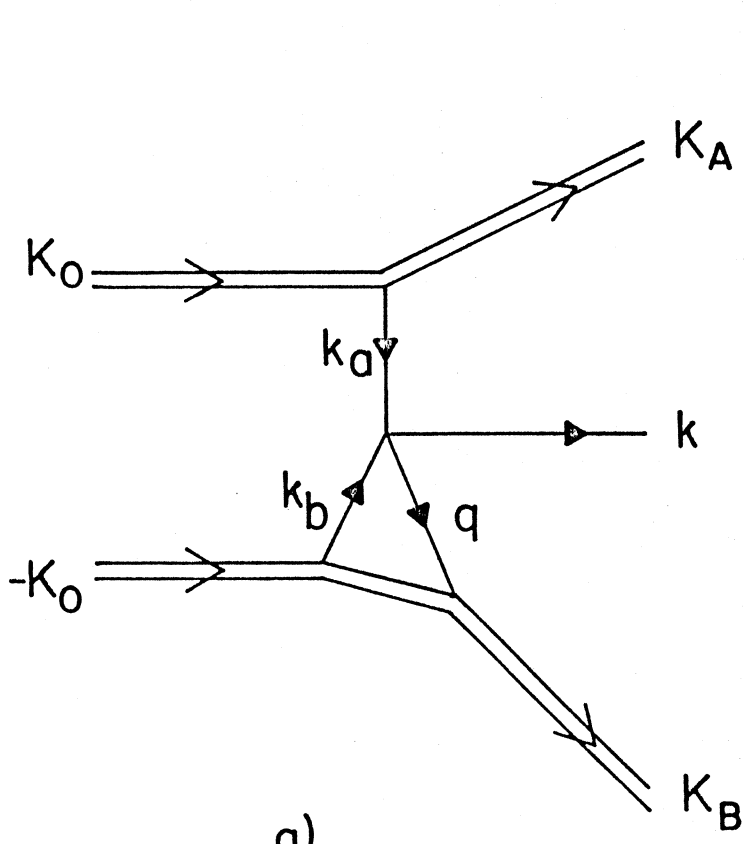

a)

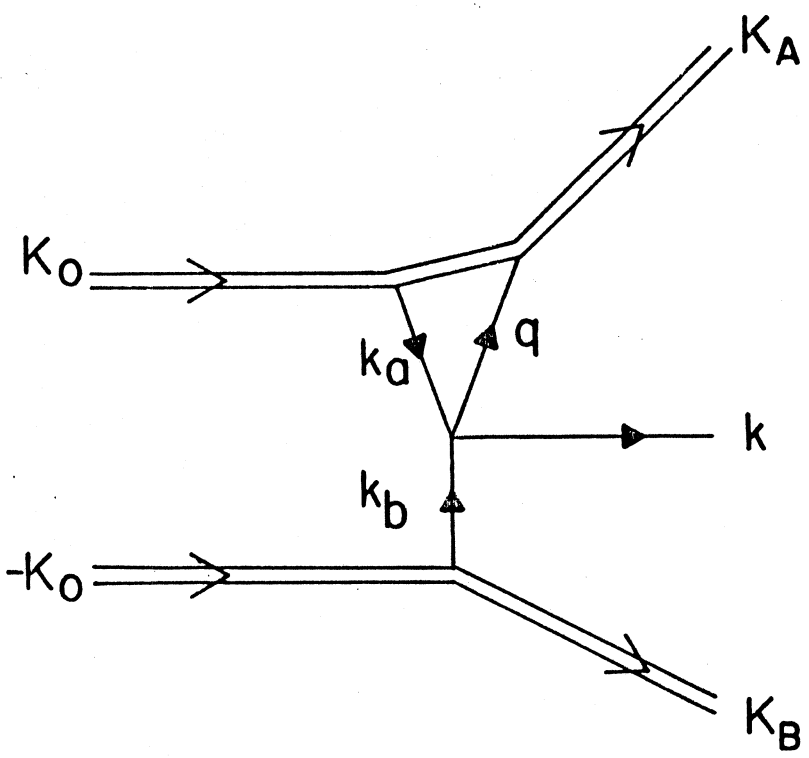

b)

Fig. 35